AN ABSTRACT OF THE THESIS OF

Aaron K. Porter for the degree of Master of Science in Civil Engineering presented on August 13, 2012

Title: Laboratory Observations and Numerical Modeling of the Effects of an Array of Wave Energy Converters

Abstract approved:

Merrick C. Haller

This thesis investigates the effects of wave energy converters (WECs) on water waves through the analysis of extensive laboratory experiments, as well as subsequent numerical simulations. Data for the analysis was collected during the WEC-Array Experiments performed at the O.H. Hinsdale Wave Research Laboratory at Oregon State University, under co-operation with Columbia Power Technologies, using five 1:33 scale point-absorbing WECs. The observed wave measurement and WEC performance data sets allowed for a direct computation of power removed from the wave field for a large suite of incident wave conditions and WEC array sizes.

To numerically represent WEC effects the influence of the WECs upon the wave field was parameterized using the power absorption data from the WECs. Because a large driver of the WECs influence on the wave field is absorbed wave power by the WEC, it is reasonable to attempt a parameterization based on this process. It was of interest as to whether this parameterization, which does not account for wave scattering among other physics, could provide a good estimate of far-field effects.

Accurately predicting WEC-array effects in the far-field requires empirical validation. Previous WEC analysis and modeling studies had limited data available for model verification, and additionally had used idealized WEC performance. In the present work we develop a WEC-array parameterization for use in phase-averaged wave models (e.g. SWAN). This parametrization only considers the wave absorption effects of the WECs and the model predictions of far-field effects are compared to observations. Further testing of the SWAN model was performed against a phase-resolving model, WAMIT, to determine the significance of physics the WEC absorption parameterization does not capture, such as scattered waves. Considering the complexity of the problem, the parameterization of WECs by only power absorption is a reasonable predictor of the effect of WECs on the far field.

Laboratory Observations and Numerical Modeling of the Effects of an Array of Wave Energy Converters

by

Aaron K. Porter

A THESIS

submitted to

Oregon State University

in partial fulfillment of
the requirements for the
degree of

Master of Science

Presented August 13, 2012

Commencement June 2013

Master of Science thesis of Aaron K. Porter presented on August 13, 2012

APPROVED:

Major Professor, representing Civil Engineering

Head of the School of Civil and Construction Engineering

Dean of the Graduate School

I understand that my thesis will become part of the permanent collection of Oregon State University libraries. My signature below authorizes release of my thesis to any reader upon request.

Aaron K. Porter, Author

ACKNOWLEDGMENTS

Sifting through and understanding all of the data produced by the WEC-Array Experiments was no easy task, and could not have been done without the collaborations of Cameron McNatt, Pukha Lenee-Bluhm, and my adviser Mick Haller. The spectacular data sets Pukha put together to characterize WEC device performance, and the countless meetings and data processing help he provided were essential; thank you Pukha. Without Cameron's help, my understanding of the wave field produced by WECs would be much more elementary; his WAMIT model results were one of the lynchpins of this thesis. Thank you Cameron for your insights, critical thinking, and WEC-array wave patterns.

Mick, your involvement and hands-on guidance kept this thesis afloat. Thank you also for involving me in such an interesting project. I cannot think of a more rewarding research endeavor for a thesis, and look forward to future work.

Thank you to my whole family for keeping a keen interest and stake in my research these past two years. Mom, thank you for your unconditional support. Dad, thank you for always telling me, "If it were easy, everyone would do it." Caroline, thank you for being such a supportive sister and encouraging me to go back to school to study what I wanted to study. I love you all.

Thank you to all my friends I gained during the thesis process. George, Kyle, John, Cameron, I would not have made it through without you guys. The late nights we had studying (mostly) in Graf Hall seems to have paid off. Marisa, I may not have met you if not for presenting this research, and for that I am extremely lucky. Your support while I wrote this thesis was invaluable, thank you for keeping me on an even keel, and among other things, I love you greatly.

This research was supported by the U.S. Department of Energy (DE-EE0002658), Sandia National Labs, and Columbia Power Technologies under Research Subagreement NO. 2010-1698, additional support came from Oregon Wave Energy Trust through Award Number OIC-0911-109. I'd also wish to thank the staff of the Hinsdale Wave Research Laboratory for their considerable effort.

TABLE OF CONTENTS

TABLE OF CONTENTS (Continued)

LIST OF FIGURES

LIST OF FIGURES (Continued)

LIST OF TABLES

Laboratory Observations and Numerical Modeling of the Effects of an Array of Wave Energy Converters

1 Introduction

As the importance and potential of emerging renewable energy resource technology increases, so does the need for objective research. In this case the resource of interest is the harnessing of ocean waves via wave energy converting buoys. A clear understanding of how wave energy converters (WECs) will affect the ocean environment, ocean waves in particular, is needed before commercial application. Of importance to both private industry and the public is how this new technology will affect our oceans' waves, and in turn the beach.

This thesis presents observations of laboratory data, analyzes the results, simulates select wave cases with the spectral model SWAN, and evaluates the ability of such models to predict the wave field leeward of WEC-arrays. The basis of comparison between model and experiment are longshore transects of wave height and energy flux, total power deficits between seaward and leeward locations of the WEC-array, and changes to the incident wave spectra induced by WEC-arrays. This thesis covers a wide range of information, but has three essential parts. It will make conclusions of how WECs affect the wave field by analysis of experimental data, determine whether spectral modeling can predict the affected wave field by verification against the experimental data set, and evaluate spectral model capabilities against a phase-resolving boundary element method (BEM) model, WAMIT.

Wave energy conversion is currently in it's nascent stage and has various designs, ranging from the point absorbing buoy (WEC of interest), to on-shore installments; each generates power from the oscillating nature of ocean waves. While test berths of WECs are expected to have few devices, and possibly only a single device, it is expected that WEC buoys will be deployed in arrays to employ efficiency in installment and maintenance. This paper explores single buoy and multiple buoy (array) cases.

Ocean waves, the source of power for WECs, are a manifestation of multiple forces including wind, the moon, the sun, and in some cases tectonic motion [Dean & Dalrymple, 1998]. Of interest to this paper and most common are wind waves; perturbations in the still water surface are created by the wind. These perturbations continue to grow in size with exposure time.

For the purposes of this investigation on affected water waves, the assumption of linearity is reasonable. Linear wave theory assumes waves travel through a inviscid and incompressible fluid, and flow is irrotational.

$$\eta(x,t) = a\cos(kx - \sigma t) \tag{1}$$

where η is the sea surface elevation [The SWAN Team, 2011], a is the wave amplitude, k is the wavenumber, x is location in space, σ is the radial frequency ($\sigma = 2\pi f$), and t is time. The wavenumber, k, is related to wavelength by, $L = 2\pi/k$. Wavenumber is related to radial frequency, and water depth by the dispersion relationship:

$$\sigma^2 = gk \tanh(kh) \tag{2}$$

The combination of many waves often results in the ocean surface appearing irregular and random. However, the sea surface η is a summation of sinusoidal wave forms of frequency σ, amplitude a, and phase α, at time t [Dean & Dalrymple, 1998]. Real seas are often described by its spectral content, $S(f, \theta)$ at each frequency (inverse of wave period, T^{-1}) and direction. Different frequencies in the sea will be home to varying amounts of energy. The collection of these energies is called the wave spectra. Normally in the ocean, energetic frequencies range from .05Hz to 0.25Hz, or wave periods between twenty and four seconds, respectively. At the lab scale in this thesis (1:33) that translates to 0.29Hz and 1.43Hz

Eventually the waves approach a coastline where depths decrease. Here the waves undergo transformations such as shoaling and refraction that conserves energy flux, $E_f = EC_g$[Watts/meter]. Energy flux conservation is defined as:

$$(EC_g)_1 b_1 = (EC_g)_2 b_2 \tag{3}$$

where

$$E = \frac{1}{8}\rho g H^2 \tag{4}$$

and

$$n = \frac{C_g}{C} = \frac{1}{2}\left(1 + \frac{2kh}{\sinh(2kh)}\right) \tag{5}$$

$$C_g = Cn \tag{6}$$

$$E_f = EC_g = ECn \tag{7}$$

where H is wave height; $C = L/T$ (wave celerity); $C_g$is group velocity, or the velocity at which energy propagates; n is a unit-less factor that asymptotes at 1.0 in shallow water and 0.5 in deep water; and b is the unit crest length of analysis, and varies depending on refraction.

Breaking waves are of great importance to beaches and other shorelines, because this is how energy flux from the waves is dissipated, or transferred to the environment. When waves break, they exert forces. These are always in directed in the cross-shore direction (normal to the shoreline), and if the waves break at an angle to the shoreline there are also

forces in the alongshore direction (parallel to the shoreline). Simply, force balances show that forces in the cross-shore cause undertow and set-up, while forces acting alongshore result in currents flowing parallel to the shore. These two types of current are the basis for sediment transport and help shape the beach environment. Understanding potential changes to these currents is vital to ensuring the environmental well-being of our beaches, shorelines, and aquaculture.

In a commercial wave energy farm, as with any obstruction of waves, the waves will experience diffraction and reflection when interacting with the WEC-array. Diffraction is the process in which energy is spread laterally perpendicular to the dominant direction of wave propagation [Dean & Dalrymple, 1998], that is, energy will leak along the crest of the wave and appear to smooth out the wave heights along a crest. A more technical description of the diffraction process can be found in section 5.1.

When ocean waves are affected by an outside source, the effects are not only seen in the near-field, but as previously discussed, in the far-field as well. It is expected that WECs will in some capacity affect the wave field, whether or not these effects are significant in the far-field is under investigation. These effects could be seen by decreased wave heights due to absorption by the array, diffraction around the array, changes in spectral shapes, or decreased longshore current. Accurately predicting far-field wave effects is still difficult because of limited field deployments of WEC arrays up to this time, and the difficulty in accurately modeling all the physics present needed to predict wave action near WECs.

To date, there is still a knowledge gap between numerical simulations of wave action in the presence of WEC arrays, and observational verification. In order to improve accuracy of numerical simulations we must develop a wave model parametrization for WEC arrays that is verified with both scaled laboratory data, and measured WEC performance data. Specifically of interest are the changes in waves between the unaffected and the affected, in the area in the lee of the array. To model the near and far field effects, SWAN, a third generation phase-averaged spectral model is employed [SWANTeam, 2011]. It can obtain realistic estimates of wave parameters on any scale relevant for wind-generated surface gravity waves, model over real bathymetry, and is able to model objects in the sea (such as jetties and islands) [SWANTeam, 2011].

Previous work to get to this knowledge gap between empirical and numerical simulations has not been trivial. There are have been previous attempts at roughly predicting far-field WEC influences by modeling. Additionally there have been several WEC-array experiments, but none had yet closed the gap between model and observations.

Literature Review Wave energy has been of interest to the scientific and engineering community for several decades, with literature dating back to the 1970s [Budal, 1977], but only recently has there been a sharp increase of analysis and experimentation. Previous experiments have been small in scope and varied in the type of WEC used. Ashton et. al.

[Ashton et al., 1999] measured the effects of an array of WECs on the surrounding wave field with a floating oscillating water column device, but data analysis was limited to five wave gages sparsely populated near and within the array with only one being completely in the lee. They found that single point measurements are not suitable to quantify the effect of a WEC on the surrounding wave field, and that more measurement points were needed to provide a more detailed pictured of what was occurring in the wave field.

Running WEC experiments is a difficult task in part because of small response signal sizes in comparison to tank modes [Boyle et al., 2011], which may have been a factor in the experiments by Ashton et al [1999]. Boyle et. al. showed that point measurements of surface elevation are not sufficient in defining the incident wave conditions for many WEC models by extensive empty tank testing and modeling. Nodes and anti-nodes make it difficult to isolate the response signals of the WEC-array, especially signals below 10 percent [Boyle et al., 2011].

Alexandre et al. [2009] ran physical experiments with 1/67th scale heaving point absorbing WECs and tracked the changes made to the spectra in the physical experiment between incident and lee conditions using seven wave gages; three in the lee, three in the offshore, and one longshore of the WECs. The measured relative changes in spectra due to the five by two sized WEC-array were input to a numerical model, SWAN, then the authors ran the model towards a shoreline. They found that group velocity had changed from the incident wave climate, as well as the spectral shape, which had become bi-modal when the WEC was tuned to the peak frequency of the incident spectra.

Preliminary work for this thesis was published in Haller et al. [2011] and among the results was that the shadow was not dependent on incident wave height, but primarily upon wave period and array size. This suggests the nonlinear effects are not of primary concern. This paper also remarked that based on wave height analysis wave absorption, and not scattering was the dominant process inducing the shadow.

None of the experiments listed above considered interactions between WECs in arrays. When interactions between WECs influence the overall performance of the array, this effects of this physical process are called the interaction factor, or q. The interaction factor is equal to 1.0 when the maximum power absorbed in an array is the same as achieved in isolation, with values greater or less than this indicating positive and negative interactions, respectively [Weller et al., 2009]. Weller et. al. obtained experimental measurements of power absorbed by a small two-dimensional array of heaving devices in regular and irregular waves. It was reported that the factor q can be be anywhere between 0.8 to 1.1 for regular waves, and 0.8 to 0.9 in irregular waves. These values were intended help form a basis for evaluating numerical models.

Most recently, two major fields in WEC-array modeling have emerged; understanding behavior within and very near WEC arrays, and modeling WEC-array effects in the far-

field. Often, these goals require different modeling and analysis techniques. Phase averaged models, like SWAN, are intended for multi-kilometer domains with varying bathymetry, while phase resolving programs like WAMIT are better suited to model the near-field and are not built for modeling large domains with variable bathymetry.

As previously mentioned this paper primarily uses SWAN to model the wave field, as it is a common tool in wave analysis and has been used in the past to model WEC-array effects [Millar et al., 2007; Smith et al., 2012; Alexandre et al., 2009]. As a spectral model it does not model individual wave forms, instead it tracks spectral energy in space and time as phase averaged quantities. In this sense it cannot model constructive or destructive interference from multiple waves, or interactions between WECs. However, it has previously been shown that although such a model cannot account for WEC interactions, spectral models may be able to reasonably predict the wave field in the lee of a WEC-array [Folley & Whittaker, 2011]. It is not without its limitations though, Monk et. al. [Monk et al., 2011] found that when compared to experimental data SWAN does not laterally spread leeward wave energy passing through a WEC quickly enough.

SWAN was developed to numerically represent the effects of spatial propagation, refraction, shoaling, wave generation, dissipation, and nonlinear wave-wave interactions. In order to accurately represent these effects, SWAN solves the spectral action balance equation:

$$\frac{\partial N}{\partial t} + \frac{\partial c_x N}{\partial x} + \frac{\partial c_y N}{\partial y} + \frac{\partial c_\sigma N}{\partial t} + \frac{\partial c_\theta N}{\partial t} = \frac{S_{tot}}{\sigma} \tag{8}$$

where σ= radian frequency, N is the energy density $E(\sigma, \theta)$ distributed over radian frequencies σ and propagation directions θ. The evolution of the action density, N, is determined in space and time; it is defined as $N = E/\sigma$ and is contained wholly on the left side of the equation. The right side S_{tot} is the sum of physical processes, or the "sources and sinks", that generate, dissipate, or redistribute wave energy. S_{tot} balances with the kinematics of the wave energy located on the left side of the equation. SWAN has six process that add to S_{tot} :

$$S_{tot} = S_{in} + S_{nl3} + S_{nl4} + S_{ds,w} + S_{ds,b} + S_{ds,br} \tag{9}$$

These terms, in order, represent: wave growth due to wind, nonlinear transfer of wave energy through three-wave and four wave interactions, wave decay due to white-capping, wave decay due to bottom friction, and wave decay due to wave breaking [SWANTeam, 2011].

At the onset of spectral WEC modeling in SWAN, WECs were represented as large objects, where energy is removed from the wave field at equal magnitudes across all frequencies over a large swath of sea. For example, Millar et. al., modeled the effects of the proposed Wave Hub in the U.K. off the north coast of Cornwall by a 4km wide partially transmitting obstacle. This type of obstacle removes portions of energy up to one-hundred

percent, equally across all frequencies; the percent removed is chosen by the user [SWAN-Team, 2011]. A range of transmission coefficients was chosen to represent varying degrees of WEC spacing in the array. The results from that analysis showed a minimal impact to the shoreline, and little cause for concern. However, those authors noted that their analysis does not use transmission coefficients from actual WECs, and that the purpose of the analysis was to determine whether the effects could be practically measured.

Since then, predicting WEC array effects with spectral modeling has evolved, taking into account the frequency dependence of WECs. It started with Alexandre et. al. in 2009 who fused together numerical and physical modeling of WECs to get an idea of how a frequency dependent transmission coefficient alters the wave climate. In contrast with this paper, their interest was in how spectra change as they approach the shore, and not precisely modeling WECs in SWAN.

More recently, two of the authors from the previous Wave Hub paper, addressed the Wave Hub problem again in 2012 [Smith et al., 2012]. Here, the authors modified the SWAN source code to allow for directional and frequency dependent transmission coefficients. The purpose of this paper was not to get the best simulations from SWAN, but rather to asses the differences between WEC arrangements in the wave-farm. To this point, they varied the shape of the relative capture widths (RCW) of the WECs between a narrow band (large amounts of energy absorbed at few frequencies) and a wide band (small amounts of energy absorbed at many frequencies). They found that no matter the arrangement or RCW shape, wave height differences at the shoreline were very small.

The TELEMAC-based Operational Model Addressing Wave Action Computation model, or, TOMAWAC, is spectral wave model similar to that of SWAN. Like SWAN, it solves the wave action density balance equation (eaquation 8). Silverthorne and Folley [Silverthorne & Folley, 2011] used TOMAWAC to model WEC-array effects in order to examine the importance of frequency and directionality responses of the wave climate. The WECs are treated as an additional sink term in equation 9 which are directional and frequency dependent, similar to the process is the 2012 Wave Hub paper by Smith et. al. Unlike Smith et. al., here the authors calculated a RCW curve for an idealized surging WEC based on a linear single degree of freedom system that was a nonlinear function of the ratio between frequency, f, and the device's natural frequency, f_0. The WEC model had a cosine squared directional dependence, which was consistent with frequency domain modeling of the Oyster oscillating surge wave converter [Silverthorne & Folley, 2011]. They found that modeling the WECs as individual grid points, rather than a single line to represent many WECs, was more realistic. This sub-grid resolution for WEC representation could be important for WEC array design.

Different from spectral models are those models that are not phase averaged, such as MILDwave which solve the mild slope equation, and WAMIT which is a boundary element method (BEM) model. Troch et al [2010] investigated the effects of an overtopping WEC

by modeling in MILDwave. Because MILDwave is phase resolving, the interactions between WECs can be included in model physics. It was found that staggered WEC arrangements result in the highest power consumption, and that lee wave regeneration depends on wave period and directional spreading. Also it was concluded in this paper that wave shadows behind a device have a shorter cross-shore extent with increased wave period and increased directional spreading.

Interactions between WECs are one of the biggest differences between spectral and phase-resolving models. Phase resolving models can attempt to predict the interactions between WECs in the array. Borgarino et. al. assessed the influence of separating distances between generic points absorbing WECs using a custom BEM. It was found that the yearly averaged q factor varied at different wave periods and spacings between positive thirteen percent and negative eighteen percent off of unity, but that over the time period of a year the negative and positive interactions compensate for each other, and positioning is not a major issue. Prior to the Borgarino paper, Cruz et. al. modeled four-WEC array effects with WAMIT and found that for a selection of suboptimal control strategies the q factor equaled between 0.92 and 0.98 [Cruz et al., September 2009].

Model choice really depends on the intent of the model. Large domains (like the entire nearshore domain) are better modeled with spectral models like SWAN, while BEM models such as WAMIT are better suited for localized effects [Folley et al., 2012]. According to Folley et al. [2012] other models such as Mild-slope or Boussinesq models should do moderately well in both environments, but not as well as a spectral model in very large domains .

2 Experiment and Analysis

This section describes the WEC-Array experimental setup and analysis methodology. The physical model is described in detail as well as the data processing needed to obtain useful wave data from instrumentation for each trial. Wave conditions for each trial are discussed and summarized, further details are given in Appendix A. Organization of the processed data set is also described for later use. The processed data set was then used to determine wave shadowing characteristics for every trial by comparing the incident waves set to waves in the lee of WEC-arrays. The (non-trivial) details of how the incident wave conditions were determined when multiple WECs were installed in the tank are given in section 3.3.

2.1 WEC-Array Experiments

The WEC-Array experiments were conducted in the Tsunami Wave Basin at the O.H. Hinsdale Wave Research Laboratory (Oregon State University). The experiments used five 1:33 scale point absorbing wave energy converters (WECs, Columbia Power Technologies "Manta-3.1"). Data was collected between November 18, 2010 and February 15, 2011 (Processed data is available upon request, merrick.haller@oregonstate.edu). The organization and format of the processed data is located in section 2.1.4. Figure 1 shows the experimental set-up from a typical five WEC (devices in yellow) array. The sticks protruding from the devices hold LEDs which were used for optical motion tracking for each 3-bodied device. Also shown are several wave gages with pink flags attached. The water surface appears cloudy due to a chalk-like substance that was used as a contrast agent for the stereo imaging camera system mounted on the ceiling

2.1.1 Experimental Set-up

Wave Energy Converters The lab experiments were performed with a 1/33rd scale version of the "Manta 3.1" WEC, a point-absorber designed to capture energy in both heave and surge. In theory, such a design allows the device to capture twice the wave energy of a point-absorber designed to capture in heave only. The "Manta" has both a fore and aft float which are attached to a heavy spar through a drive shaft, which is shown in Figure 2. As incoming waves pass the WEC, heave and surge motions force the floats to rotate about the top portion of the spar and drive their respective direct drive rotary (DDR) generators. At lab scale the WECs have a diameter of approximately 0.55 meters, at field scale this is equivalent to eighteen meters. Using the motion tracking data, power capture by the WECs was measured and recorded for each trial condition. This mechanical power capture behavior by the WECs are compared to power deficits measured in the wave field.

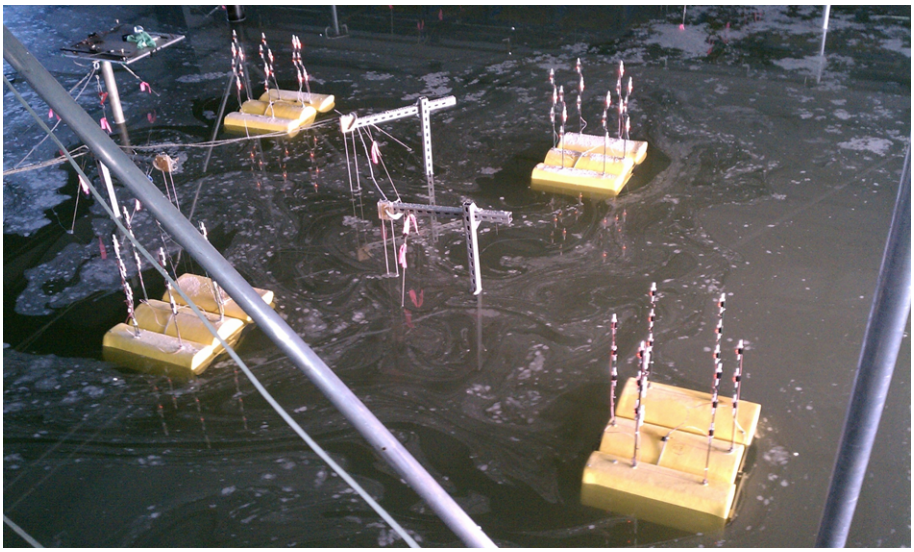

Figure 1: Photograph of the 5-WEC array experimental setup. WECs are yellow with LEDs attached to vertical posts for motion tracking. Also shown with the pink flags attached are several wave gages

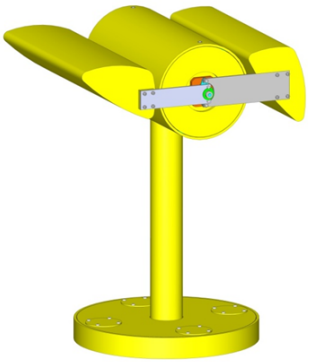

Figure 2: The "Manta 3.1" 1:33 scale wave energy converter (Columbia Power Technologies)

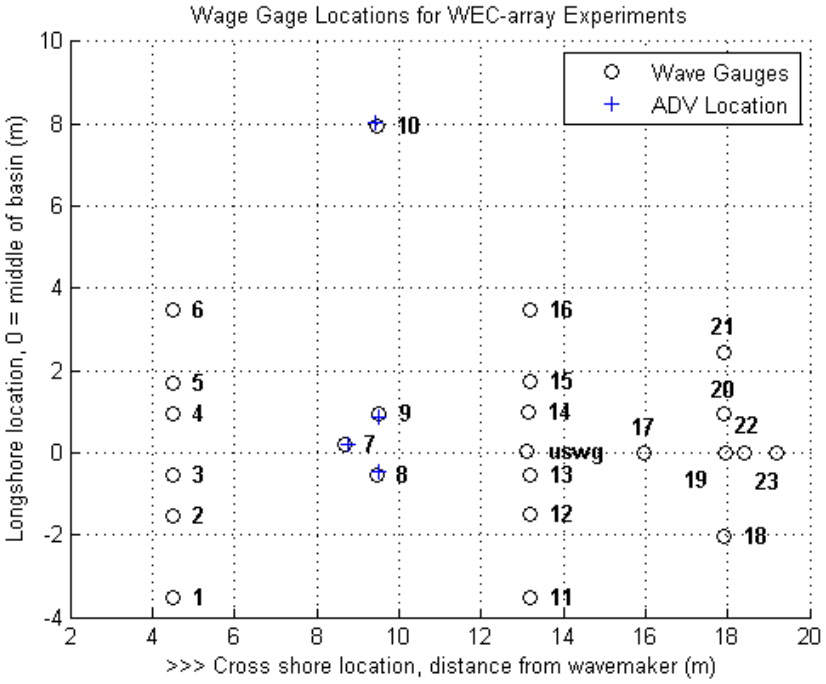

Figure 3: Layout of the wave gages for the WEC-Array Experiments.

Physical Model The internal dimensions of the wave basin are approximately 48.8 m in length by 26.5m with the Directional Tsunami Wavemaker situated at one end. A plan view of the wave basin is shown in Figure 4. This figure also shows the coordinate axes; the origin is located at the wavemaker. The wavemaker consists of twenty-nine, two-meter wide, piston-type wave-boards. These wave boards have a maximum stroke of 2.1 meters, have directional wave capability, and are equipped with active wave absorption. The system has the ability to produce regular, irregular, tsunami, multidirectional, and user defined wave fields. The maximum water level in the basin is 2.1 meters; however, for this experiment water levels ranged from 1.365 meters to 1.372 meters. Opposite the wavemaker, on the far end of the basin, a crushed rock beach of initial grade of approximately 1:12 was installed to mitigate cross-shore wave reflections in the tank.

Instrumentation Twenty-seven in-situ instruments were placed in the wave basin. This included twenty three wave gages, one ultrasonic wave gage, and three acoustic doppler velocimeters (ADVs). Detailed locations are plotted in Figure 3. Wave gages were placed in instrument arrays designed to measure and resolve directionally-spread incident wave fields, wave fields in the lee of the WECs, wave scattering in and around the WECs, far-field effects, and cross-shore reflections near the beach. Theses gages report voltage, which is

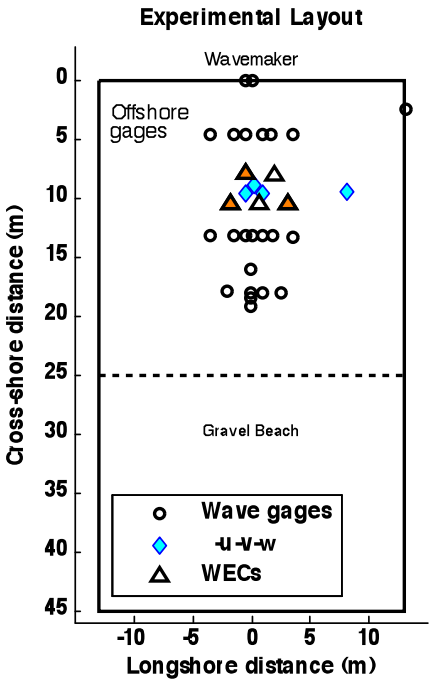

Figure 4: Experimental layout of wave gages, acoustic doppler velocimeters (ADVs), and WECs in 5-WEC array arrangement. Three device arrangement shown in orange.

linearly proportional to water surface elevation, η. To convert data units from voltage to meters, the gages must be calibrated, and produce a calibration coefficient. Each gage was calibrated at each basin fill, and drain. The method for determining calibration coefficients is discussed further in section 2.1.3 and the results plotted in Figure 6. Co-located with select wave gages within the WEC array, and at gage ten, are ADVs which measure fluid velocity in three directions, $u - v - w$. See Figure 4 for locations of the gages in reference to the WEC-array. The WEC location(s) are centered in the basin to reduce side wall effects, eight to ten meters from the wave maker. Each of the WECs was moored to the basin floor in one of five positions. Throughout the experiment the number of WECs in the water at one time varied between one, three, and five; and when in the water, the WECs were always moored in the same position (1-5). To measure WEC movements, in order to calculate power absorbed by the WECs (i.e., velocity squared times damping = power), a commercial LED tracking system was employed. LEDs were attached the WECs via rods protruding from the three WEC body portions (main body, front and back flaps). Through the tracking data, the system was able to measure time-series of position in 3D space. These data were used to calculate object velocity and extracted power. Attached to the ceiling of the facility was a bi-static camera system to include 3D imaging capability through binocular stereo.

Basin Survey Bathymetric surveys of the beach were taken before and after the experiment occurred. Survey data is contained in the WEC-array experiments processed data set. The surveys were taken using LIDAR technology, by Michael Olsen and the OSU Geomatics unit at a resolution of 5 cm with 222,744 total grid points. Because of line-of-sight limitations, three scans are combined to include the entire basin. The LIDAR data set was produced in the TWB coordinate system. For the purposes of this experiment five centimeter spacing was not needed, so the original grid was interpolated to a regular 10cm regular grid.

2.1.2 Wave Conditions

The experiment consisted trials that varied between regular monochromatic waves and irregular (real seas) waves; single and multidirectional waves; and normally incident and off-angled waves. The lab scale waves were developed from a suite of target field scale conditions. Equivalent lab scale wave periods were calculated using Froude scaling, $T_{scale} = \sqrt{L_{scale}}$, where T is time scale and L is the length scale.

Test names and trials are organized by wave-type, and WEC-count (i.e., 3-WEC frequency scan, where frequency scans are constant wave height and variable regular wave period). These tests consist of variable amounts of individual trials, depending on type, and vary between thirteen and one-hundred-ninety-four trials per test. Most tests were run over several days, while some (i.e., Single Buoy Characterization) were ran in several days over the course of 2-3 months. Characterization tests are only different than other tests in that the physical WEC in the water was changed throughout, although the WECs mooring position was always the same. Detailed characteristics of the trials are located in the Appendix.

Regular Waves Regular waves tests consisted of monochromatic waves, with incident angles of normal, and twenty two and one half degrees. At field scale these waves range from periods of 5.2 seconds to 16 seconds, and wave heights of one meter to five meters. Table2 has a summary all of the regular wave conditions tested from both the scans and the characterization. A more detailed description of conditions tested, along with associated trial numbers can be found in the Appendix. Although the wave heights span a range of values, in the following analysis the focus is on target wave heights of six centimeters. The six centimeter waves have the most populated scans between different wave periods.

Regular wave trials generally consist of 50 waves; so the sample times vary depending on nominal wave period. Early on in the experiment, during the single buoy scans, only twelve waves were ran per trial instead of fifty, so these runs are much shorter. However, the single buoy characterization trials all have 50 waves per trial.

Table 1: Tests in the WEC-Array Experiments

The WEC-Array Experiments	
Test Name	**No. Trials**
Argus Pre-test (empty tank)	13
Single Buoy Amplitude Scan	75
Single Buoy Frequency Scan	82
Single Buoy Real Seas	76
Three Buoy Amplitude Scan	51
Three Buoy Frequency Scan	62
Three Buoy Real Seas	70
Five Buoy Amplitude Scan	53
Five Buoy Frequency Scan	54
Five Buoy Real Seas	60
Single Buoy Characterization	194
Single Buoy Characterization Off Angle	114
Single Buoy Characterization Real Seas	39
Single Buoy Extreme Seas	9
Total	**952**

Table 2: Regular wave trial conditions

Regular Waves			
H (cm)	**Period**[1]**(s)**	**Angle**[2](θ)	**WEC-array**[3]
3	1.0-2.8 [11]	0, 22.5	1
6	0.9-2.8 [20]	0, 22.5	1
6	0.9-2.7 [15]	0, 22.5	3, 5
6	1.8-2.8 [3]	22.5	3, 5
9	1.0-2.6 [7]	0, 22.5	1, 3, 5
12	1.3-2.6 [5]	0, 22.5	1, 3, 5
15	1.3-2.6 [5]	0, 22.5	1, 3, 5
[1] Wave periods represent max and min of tested range; bracketed number indicates number of periods tested within this range.			
[2] Wave angle with respect to shore normal.			
[3] Number of devices in array.			

Table 3: Real seas target wave conditions 1

Real Seas					
Wave height	**Peak period**	**Peak direction**	**Directional Spreading**	**Sea State**	**WEC-Array**
$H_{m0}(cm)$	$T_p(sec)$	θ_p	s^1		
4.5	1.2, 1.6	0, 22.5	4, 10, UD	HI – Kaneohe, Oregon 1	1
4.5	1.2, 1.6	0, 22.5	2, 4, 10, UD	HI – Kaneohe, Oregon 1	3, 5
7.6	1.4, 1.8, 2.2	0, 22.5	4, 10, UD	Oregon 2, 3, 4	1
7.6	1.4, 1.8, 2.2	0, 22.5	2, 4, 10, UD	Oregon 2, 3, 4	3, 5
10.6	1.6	0, 22.5	4, 10, UD	IR – M4 Buoy	1
10.6	1.6	0, 22.5	2, 4, 10, UD	IR – M4 Buoy	3, 5
13.6	2.2	0, 22.5	4, 10, UD	Oregon 5	1
13.6	2.2	0, 22.5	2, 4, 10, UD	Oregon 5	3, 5
30	2.6	0	UD	Oregon Storm	1
45.2	2.6	0	2, UD	Extreme Seas[2]	1
45.2	2.6	22.5	UD	Extreme Seas[2]	1
[1] Directional spread parameter, s, for distribution $[0.5\cos(\theta - \theta_{mean})]^{2s}$					
[2] 100 year storm event					

Real Seas Also run in during the experiment were the real seas simulations. These trials are intended to simulate sea state conditions at different potential installation sites. Spectra for all trials are Joint North Sea Wave project (JONSWAP) shaped with $\gamma = 1.0$; equivalent to the Pierson-Moskowitz (PM) spectra [Sorensen, 2006].

$$S(f) = \frac{\alpha * g^2}{(2*\pi)^4 f^5} e^{-1.25(f_p/f)^4 * \gamma} \tag{10}$$

Both unidirectional (UD), and multidirectional incident wave spectra were run from normal and offangle directions. At field scale the typical peak periods of the spectra range from seven to fifteen seconds, and significant wave heights of one and a half meters to four and a half meters. Real seas trials have longer sampling times than regular waves trials so that the random wave spectra can be considered statistically significant. The sample times for real seas tests ranged from 313 seconds to 540 seconds, with the latter applicable to all but the Single Buoy Real Seas Test and a portion of the Single Buoy Characterization Real Seas test. Table 2.1.2 summarized real seas wave conditions tested. A more detailed description of conditions tested, along with associated trial numbers can be found in the Appendix.

WEC-arrays WEC-array arrangement varied throughout the experiment, with any of one, three, of five WECs in the water at one time. There were five possible mooring positions for the WECs, seen in 5. During the trials WECs tended to move slightly around in the basin, so the positions plotted are the average positions as determined by to motion tracking

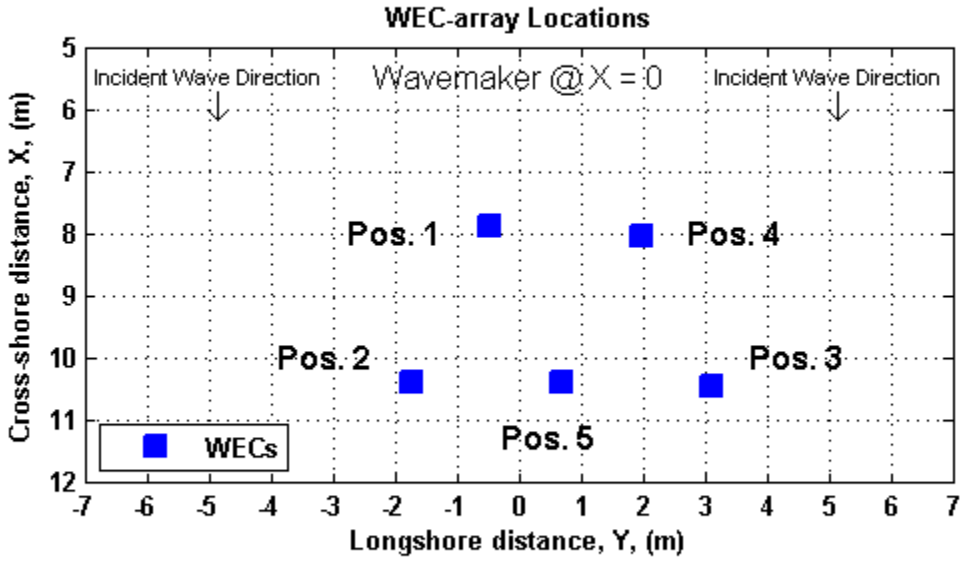

Figure 5: Detailed locations of the five WEC-array positions. Blue squares mark the mean positions of the WECs.

data for select trials. For almost the entirety of the experiment, WECs were moored in only one location (i.e., WEC #3 was only moored in position 3). The lone exception was during single buoy characterization trials, where all WECs, 1-5, were moored to Position 1 for different trials throughout the tests. For all single buoy tests the WECs were moored in Position 1 only; for all of the three buoy tests WECs were moored in Positions 1, 2, and 3; for the five buoy tests WECs were moored according to their WEC number at all five positions.

2.1.3 Quality Control

The first step in processing trial data was to review time series data for all wave gages for every trial in order to check for possible flagged trials. There are twenty-four channels (twenty three wave gages and one ultrasonic wave gage) with sea surface elevation time-series; data from a single trial is best viewed on separate subplots of several gages apiece.

Flagging potential problems was done by hand on a quality control spreadsheet. The quality control sheet contained a matrix of trial numbers and wave gages for each test. Trials that looked odd or contained questionable data were marked as so for reference. The quality control sheets later saved time by reducing the amount of back checking necessary. During the quality control process the ultrasonic wave gage was identified as having extremely noisy data in many of the trials.

It's important to remove the noise (spikes) in the ultrasonic data so that accurate wave heights are recorded. The accuracy of the ultrasonic gage is especially important because it is part of the process that calibrates the conversion from volts to meters for wave gages; the calibration process is discussed in depth in the following section "Wave Gage Calibration". Spikes in wave gage surface elevation time series were identified and then removed using phase-space method by developed by Goring and Nikora [2002], and later modified by Nobuhito Mori [2007]. This method assumes that the data set is random, and that the instantaneous acceleration must be less than gravity. Many of the data trials in the current data set however, were not random, but instead contained sets of regular waves. This caused problems in recognizing real spikes against false spike identifiers. A small adjustment to the spike identifying threshold was made to account for the regularity of the sinusoidal waves. The original universal threshold was , $\lambda = 2 * \log(n)$ but an adjustment that worked, with visual confirmation, was to multiply this value by $\sqrt{2}$, which decreased the sensitivity of spike identification. This allowed regular wave trials to be better analyzed by the method.

Wave Gage Calibration A calibration value is needed to convert the voltage in each gage to units of meters. From past experience at the HWRL, it has been shown that the electronegativity in the tank changes during the first few days after the basin is filled with water, which results in changing calibration values. Hence, calibration values need to be monitored throughout the experiment. However, the standard method for obtaining calibration coefficients for each gage involves either draining or filling the tank. To estimate calibration between calibration events, a good understanding about the behavior of electronegativity in the tank over time is needed. Here we have used a fixed ultrasonic wave gage (USWG), co-located with one of the regular resistance wave gages, as a fixed reference point; under the assumption that the calibration coefficient of the USWG does not change over time (since it is based on the speed of sound in air). Comparing wave height readings from these two gages gives an estimate of how the electronegativity in the tank changes over time. However, data from the USWG is noisier, so these data need to be used with care so that noise does not overly affect the calibration adjustments.

Two sets of calibration curves were needed, because there were two separate instances of filling the basin, and then draining it. The ratio of the USWG to the local gage in each instance, these are denoted as $2010ratio$, and $2011ratio$ (occurring in Experimental Phases One and Two. The 2010 fill/drain spanned a longer period of time, and in turn has a larger

range between fill and drain calibration coefficients.

To start, we looked at the recorded voltages of the co-located gage during regular wave trials and compared it to voltage from the USWG. Before this was possible, the noise problem in the uswg had to be fixed to obtain accurate Hmean values for each trial. We decided to find trials that did not have any noise problems throughout a portion of the trial that was at least five wave periods long, and that had a standard deviation between wave heights within the trial of 0.003. This standard deviation constraint was chosen since the method for determining steady state portions of the trials was still in its infancy, and at the time, safeguards were thought to be needed to avoid inaccurate data. Trials that passed this are the only those trials used to determine the calibration equation. We assume that the quality of these trials give an accurate representation of the real ratio between the local gage, and the uswg.

Plotting the 2010$ratio$ (between H_{mean} of the USWG and the local gage, or $USWGRatio$) for trials that passed the above constraints indicated that just after the drain, the ratio fell sharply, before falling slowly off, as shown in Figure 6. Two curves are used to describe the 2010$ratio$. The first is fit to tests 'SingleBuoyAmplitudeScan', 'SingleBuoyFrequencyScan', and 'ThreeBuoyAmplitudeScan'; these are used in the curve fit of the time in which the 2010$ratio$ drops off relatively quickly. The 2010$ratio$ data from these tests was fit to a power curve of the form: $ratio = a^{log(b*UTC_{date}+c}$; and the coefficients were determined by reducing the levels of squared absolute error. The resulting curve is seen in Figure 6 and the equation,"CalibrationRatioPowerCurve". Additionally, a linear fit from the end value of the power curve fit, to the drain calibration value completes the calibration curve for 2010 data.

Phase 2 of the experiment occurred in 2011, in a different fill/drain period, and makes up the second calibration curve. The time period which it occurred in was shorter than the 2010 period, and less change in calibration coefficients were observed between the fill and drain. Because of this a linear fit between the fill and drain calibration coefficients was chosen as the calibration curve. The next step was to convert from units of volts to units of meters. This was done by multiplying the constant uswg calibration (0.174 volts/m) by the ratio between the local gage and the uswg, giving the calibration coefficient of the local gage to convert to meters from volts at any point in time.

Each gage has its own calibration coefficient for the fills and drains, which was measured and calculated by wave basin staff. The ratio curve must be scaled accordingly to each gage's change in calibration magnitudes, which vary by up to approximately 100%. That is, the curve must be scaled to account for differences in the absolute change of calibration values for each gage, compared to the absolute change of the co-located gage. That ratio, of gage thirteen to any other gage, is approximated by a linear trend by both gages between their fill and drain coefficients. While this method of scaling is not exact, it provides a decent

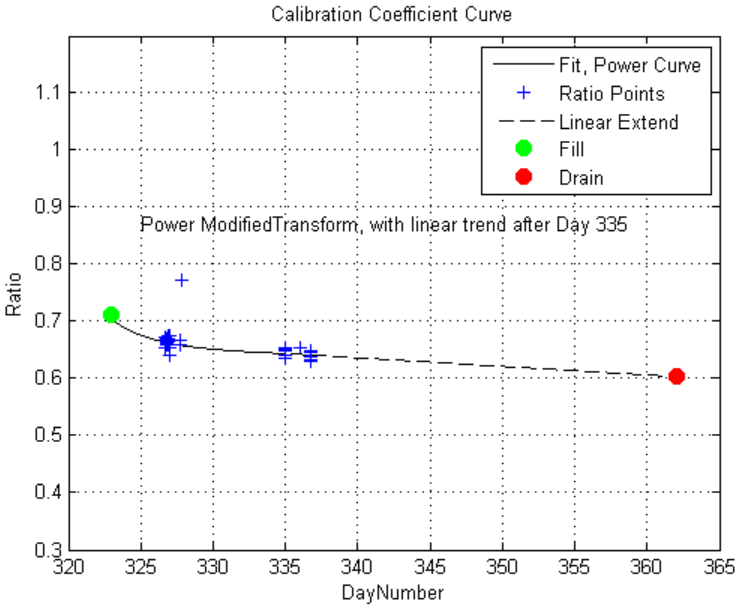

Figure 6: Calibration curve for the 2010 raw wave data. A modified power curve was fit to data points that passed stringent quality control checks.

approximation for the differences between the absolute changes of each of the gages at any day and time. The functions $CalCoeff2010$and $CalCoeff2011$ do this. The calibration coefficient for any gage in time is then $0.174 * USWGRatio$, multiplied by the ratio of the approximate change of a selected wave gage at a certain time to the approximate change of the local wave gage at a that same time ($gage2gageRatio$). This method applies to both the 2010ratio and 2011ratio.

$$CalCoeff = 0.174 * USWGRatio * gage2gageRatio \tag{11}$$

The end product, the calibration coefficient $CalCoeff$, is multiplied by the raw data which is in units of volts, and converts the wave data into meters. All processed wave data uses this method, and is therefore reported in meters. The function$CalCoeff$ is able to produce any calibration coefficient given a channel number (1-30) and UTC date, and in turn, calibrated wave heights.

2.1.4 Data format and Organization

Wave gage data from the WEC-Array experiment was reported in units of volts, and stored in large text files with the nomenclature "...analog_master.txt". Each trial has its own text file that contains 30 columns of wave data, and approximately fifty lines of metadata. The

thirty data columns are from data collection channels; 24 of which are wave gages used for experimental analysis, one of these is an ultrasonic wave gage. The remaining channels are used by the wave lab staff for various operational reasons. Data was collected at 50Hz in all of the tests.

Processed data for the experiment is organized in Matlab structure files by test name. The processed data files contain data extracted from the raw text files, which are then converted to meters using the function $CalCoeff$ as described in equation 11, and truncated to include only data measured during steady state. The raw text files are fairly consistent, but not entirely so; the command inputs had to be modified occasionally between trials and tests to accurately import the necessary information such as the time and date for each trial, the incident conditions, and the wave data. This information, as well as wave characteristics, fill the data structures.

When opening the structure files the user will encounter a four element structure comprised of:

- 'Testfolder', the name of the folder in which the raw data is located, in the experiment data

- 'TrialNumbers'. This vector contains the trial numbers from the test folder of interest (Amplitude Scan, Frequency Scan), in order. All of these trials are included in the TrialData structure. It links each of the trial entries in TrialData to their corresponding trial order in the TestFolder.

- 'TrialData' contains the data from corresponding trials in 'TrialNumbers' from the original test folder of interest .

TrialData is organized by trial number and then by wave gauge, i.e. ProcData.Trial.Wavegage. TrialData opens to many structures, one for each of the TrialNumbers. The user may notice some trials are missing from the data set, these are trials that did not pass an exhaustive quality control analysis. Each of these trial structures contains eight entries: Trial Number, UTCDate (1-360 for each year), TrialDescription, TrialConditions, Trial Tank Temp, Buoy Number (WEC), Rawpoints (# of points in raw DAQ file), and WaveGages. The structure, 'WaveGages', lists each wave gauge for the current trial. There are twenty-three wave gauge structures, listed 1-23, within the WaveGages structure. Regular waves and real seas data have different wave characteristics of interest, so the data that fills the WaveGages structure differs between the two types. Each regular wave test has fourteen entries in it's respective wave gauge structure:

- Channel Number,
- xpos (x-position in basin),
- ypos (y-position in basin)
- Hseries (calculated as crest to trough)

- Tseries, Hmean (of Hseries)
- AmpSeriesRMS (waveform amplitudes calculates as sqrt(2)*RMS(waveform)
- HRMS (mean wave height as calculated by RMS)
- Hdev (standard deviation of crest to trough)
- Hmean, Tmean, Tdev (standard deviation)
- Number of waves (between QCindicies)
- QCindices (starting and ending points of steady state)
- CalibrationCoefficient

Real seas data contains calculations based on either 280 or 480 seconds of steady state wave data. This size of "window" was chosen so that the frequency resolution is .05, which corresponds to 28 and 48 degrees of freedom, respectively. The eighteen data entries in the real seas data sets are slightly different than regular waves:

- Channel Number
- xpos (x-position in basin)
- ypos (y-position in basin)
- PSD (Power Spectral Density, mˆ2/Hz)
- Frequencies (associated with PSD)
- Hm0 (four times the square root of the sum of the power spectral density, summed between $\frac{1}{2}$ of the peak frequency to 5Hz)
- Tp (Peak frequency in PSD)
- Te (Energy Period, negative first moment divided by the zeroth moment)
- J (Omnidirectional Wave Power = density*9.81*sum(group_velocity*PSD*df);
- DegreesOfFreedom
- df (Frequency resolution in PSD)
- QCindices (starting and ending points of steady state identifier algorithm)
- NumWaves (Number of waves between QCindicies)
- Hseries

- Tseries
- Hmean
- CalibrationCoefficient

As an example, to access the spectral density for each trial one and gage 16, the user simply types $ProcData.TrialData(1).WaveGages(16).PSD$.

Averaged incident wave conditions for the experiment are collected in a separate master file. It covers all regular waves with a target wave height of six centimeters, and all real seas simulations with no directional spreading. Like the processed data, this data is most easily organized into a structure. However, this structure includes both regular wave and real seas data. For more on this see section 3.3.

2.2 Data Processing

2.2.1 Regular Waves

Regular (monochromatic) waves are the simplest and easiest waves to understand, and are a good starting point for understanding how WECs affect waves. In these experiments there were sixteen regular waves tests which spanned the range of wave periods from 0.9 seconds to 2.8 seconds, range in wave height from three centimeters to fifteen centimeters, and have incident directions of shore-normal and 22.5^ooff normal. This section details how wave height and wave period of these waves are calculated, and also sets a criteria for determining when full wavemaker action is in effect.

Determining Steady State for Regular Waves When the wavemaker begins to make waves there is an initial ramp-up period during which the wavemaker stroke steadily increases from rest to target amplitude. Wave data of interest occurs when the waves recorded are those created by the wavemaker when it is in full action. Since the WEC-array experiments contained a range of wave periods the amount of sample time the wavemaker at full action running varies. Also varying in the data set was the still-water time that was recorded before wavemaker action began. The following accounts for this, finds the wave data of interest, and extracts it from the time series of the whole run.

To figure out how many data points should be included in the "good", or steady state, wave data, first a database containing the wave period for each run is compiled. The test plan sheets tell how many waves are going to be made under full wavemaker action for each run. Every trial during the experiments was run at a sampling rate of 50 points per second. So for example, during a certain run we know there are 50 waves made at a period of 1.0 seconds and there are 50 data points per second. The data we want to look at is

then approximately $50waves * 1.0sec/wave * 50pts/sec = 2500pts$, twenty-five hundred data points long.

The gages, however, were not equidistant in the cross-shore from the wavemaker so the waves passing through each gage will reach full height at different points in time. We have defined this initiation point to be when the wave heights measured by the gages have exceeded one half the maximum recorded wave height in the trial, $0.5 * max(H)$ for each gage. When the $0.5 * max(H)$ threshold was exceeded the wavemaker action was at least half-ramped up. By inspection it is known that the total ramp-up time was just under 20 seconds, and was not dependent on wave height or frequency. Therefore the 'good' wave data under full wavemaker action must be in action ten seconds (500 data points) past the threshold exceedance. The same methodology was applied to the tail end of the trial to get the chopped time-series of wave data we call $wavedata$.

Wave Characteristics After determining the steady state portion of the wave gage time series, the processed wave data routine can begin. The data was first run through a filter that is the same length as the nominal wave period, which de-means and de-trends the data set. Wave heights are calculated by a zero up-crossing method, and are done so twice; once to determine the steady state boundaries, and again to determine the steady state wave heights. The zero up-crossing method identifies individual waveforms, and their height by noting indices each time the wave form crosses the zero sea surface elevation, in a positive (upwards) direction, $zero_i = find(eta < 0 \& eta1 \geq 0)$, where $eta = wavedata(1 : end - 2)$ and $eta1 = wavedata(2 : end - 1)$. Wave periods, T, are the length of time between $zero_i$ indices, and wave heights, H, are the difference between minimum and maximum sea surface elevations, eta, between $zero_i$ and $zero_{i+1}$. This method gives vectors for both H and T and the mean of these are the characteristic wave height and period for the trial.

The root mean squared wave height, H_{rms}, is an alternate way of determining wave height. For each wave form, ς (that is, eta between $zero_i$ and $zero_{i+1}$), $H_{rms} = 2 * std(\varsigma)$. Both measures of wave height were reported, and their results are nearly identical. Individual wave heights are needed to complete this routine. The wave height of record in this data set was H_{rms} .

Repeatability An important check in any experiment is repeatability, in this section we check the repeatability of both the wave maker and WEC effects. For a single target wave height (six centimeters), the repeatability of wave data between like trials of four regular wave periods were investigated for 1-WEC, 3-WEC, and 5-WEC array configurations. Figure 7 shows longshore transects of wave height in both the offshore and lee, with associated error bars of one standard deviation for these trials. The error bars are small in the offshore, indicating to us that there was good repeatability in wavemaker ability. Small error bars in the lee tell us the WEC effects on the lee wave field are also repeatable.

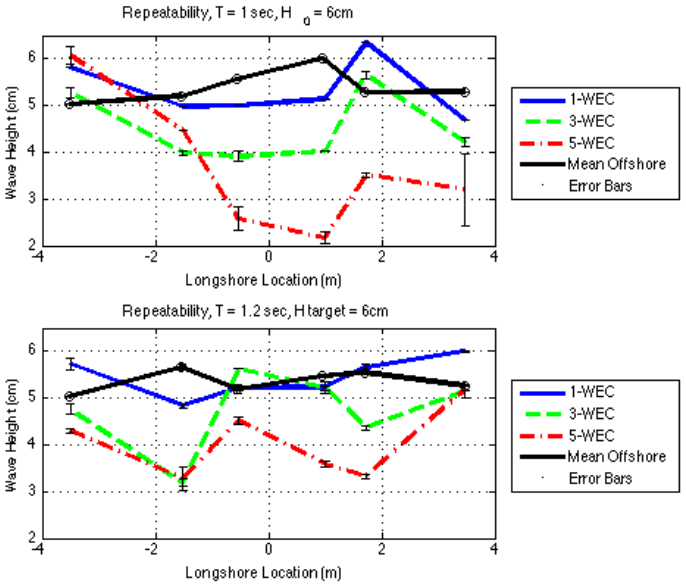

(a) Repeatability in 1.0 and 1.2 second regular waves

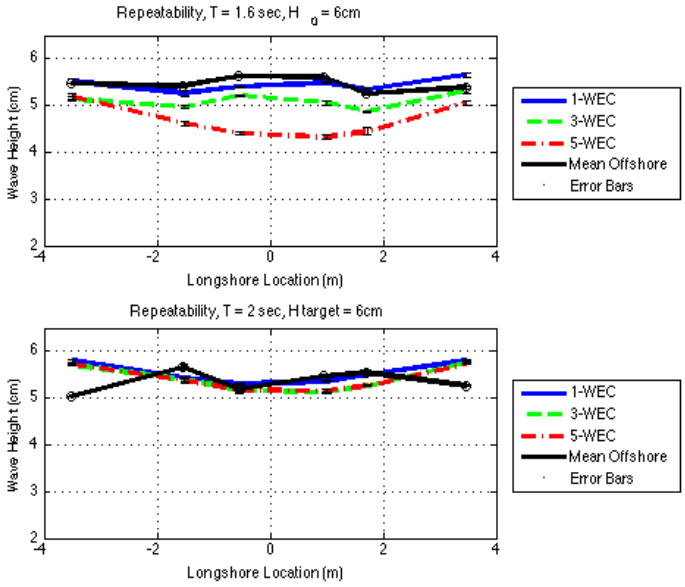

(b) Repeatability in 1.6and 2.0 second regular waves

Figure 7: Wave maker and WEC influence repeatability of wave data between like trials of four regular wave periods in single, three, and five device WEC arrays. Error bars of one standard deviation show very good repeatability between like trials. The x-axis is longshore location, the y-axis is wave height.

2.2.2 Real Seas

Data analysis for real seas trials was similar in some ways to the regular waves trials, but since the sea surface elevation characteristics are not discernible to the naked eye, more faith in analysis is required. This section details how full wavemaker action were determined, how the frequency spectra was determined, how significant wave height was calculated, and how energy flux and power were found.

Determining Steady State for Real Seas Determining steady state in a random sea was quite different than from a regular wave situation since the expected wave height of each waveform is unknown and by nature random. The duration of time between the onset of data collection wave not automated (it was a manual process); hence, the need for an automated algorithm to determine the steady state conditions based on data alone. Our method was based on calculating the root mean squared wave height, H_{rmsWin} in a series of ten-second windows throughout the trial, on a gage-by-gage basis. For each trial and gage the "pre-chopped" wave data, $wvdata$, contained $WinNum = length(wvdata)/(10sec * 50pts/sec)$, where $WinNum$ is the number of windows. Characteristic wave heights for each ten-second window were calculated, and the cumulative elapsed sample time, t_s at the midpoint of each window was recorded. Windows were sorted by H_{rmsWin}, and a threshold was developed from mean of the top twenty-five windows, $0.2 * mean\,(H_{rmsWin}(1:25))$. The collection of windows that pass this threshold are sorted chronologically, and the midpoint in time is the mean of the first and last windows $Midpt = \frac{t_{s,1}+t_{s,end}}{2}$. Trial indices are then$Ind_1 = Midpt - \frac{t_{total}}{2} + 1$, and $Ind_2 = Midpt + \frac{t_{total}}{2}$, where $t_{total}$is the total sample time of the trial which is known in advance.

Spectral Analysis This section details some aspects of spectral analysis, and how the spectral density was calculated for the WEC-Array Experiments. The processed energy spectra was calculated at twenty-eight or forty-eight degrees of freedom (dof) depending on trial length, with constant $df = 0.05$, and ensemble (Bartlett) averaging, with a Hamming Window.

The energy spectrum describes a random sea state by the energy levels at different wave frequencies, where the sum of energy from all frequencies is the total energy in the wave field, and each frequency is a sinusoidal wave form with an component wave amplitude. To characterize random seas trials, common practice is to employ spectral analysis in order to find the energy spectrum, $S(f)$, and in turn calculate the significant wave height, H_s, the peak energy period, T_p, and the energy flux, E_f.

Spectral analysis based on the Fast Fourier Transform (FFT) was developed by Cooley and Tukey [Cooley & Tukey, 1965], which makes the assumption that any piecewise continuous function can be represented over an interval of time as the sum of sines and cosines

[Dean & Dalrymple, 1998]. An additional important assumption that the FFT takes is that the time-series is infinitely long. The fact that this is never true results in an imperfect and noisy FFT full of smearing and energy leakage. These issues are dealt with through windowing and averaging energies of frequencies together, or increasing the degrees of freedom (DOF). The raw frequencies at which energies are calculated at are called the Fourier frequencies, f_j, where $f_j = j/(N\Delta t)$ for $j = 0, 1, 2..., N-1$, where N is the number of data points in the time-series, and Δt is the sampling rate. The energy spectrum at this stage is extremely noisy, with many spikes and troughs; a result of a finite number of waves frequencies made by the wavemaker, the collection rate, and a finite record length.

To deal with problems in the energy spectrum associated finite record length and non-zero end points, windowing methods are applied. Leakage occurs because only energy at frequencies that coincide with a Fourier frequency will project onto a single basis vector; all other frequencies will exhibit non zero projections onto the entire set [Harris, 1978]. Windows are weighting functions applied to time-series data to reduce the spectral leakage associated with finite time-series [Harris, 1978], the problem is that they reduce the total amount of energy in the time series, seen in Figure 8. A correction factor must be used to scale or "boost" the energy spectrum back to it's nominal total energy. This scaling factor is calculated by:

$$bst = \sqrt{\frac{var(\eta)}{var(\eta * W)}} \tag{12}$$

where η is the sea surface elevation before the window is applied, and W is the window function of length η. Both the window and the boost are applied to the time-series before any FFT algorithms are done.

Two kinds of energy spectra averaging can be employed to smooth the energy spectra: bin-averaging in the frequency domain, and ensemble (or Bartlett) averaging in the time-domain. This paper uses ensemble averaging. To ensemble average, the time-series is broken up into equal ensembles of length $N_{ens} = N/(dof/2)$, and an FFT is taken of each ensemble. These ensembles are averaged together at each frequency to get the estimated energy spectra, S:

$$S_i = \frac{\left(\left|\frac{FFT(\eta_i * W * bst)}{N_{ens}}\right|\right)^2}{df_{ens}} \tag{13}$$

for $i = 1 : N_{ens}$, and $df_{ens} = s/N_{ens}$. The resulting spectra S_i are averaged together to obtain the ensemble averaged spectra, seen in Figure 9.

Increasing the degrees of freedom results in a more statistically significant spectra, but reduces the frequency resolution. The frequency interval is related to degrees of freedom by $df = s/\frac{2N}{dof}$. As discussed 2.1.2, some of the the single-WEC real seas trials had a shorter sample time, and therefore a smaller N than 3-WEC and 5-WEC trials. We opted to

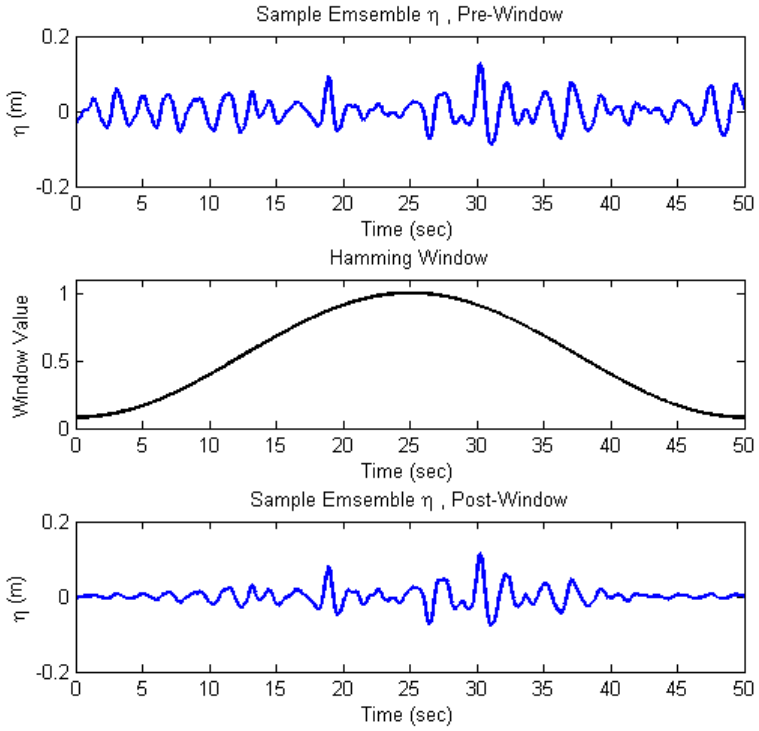

Figure 8: This example of the application of the Hamming window shows energy losses to the time-series, and the need for energy "boosting".

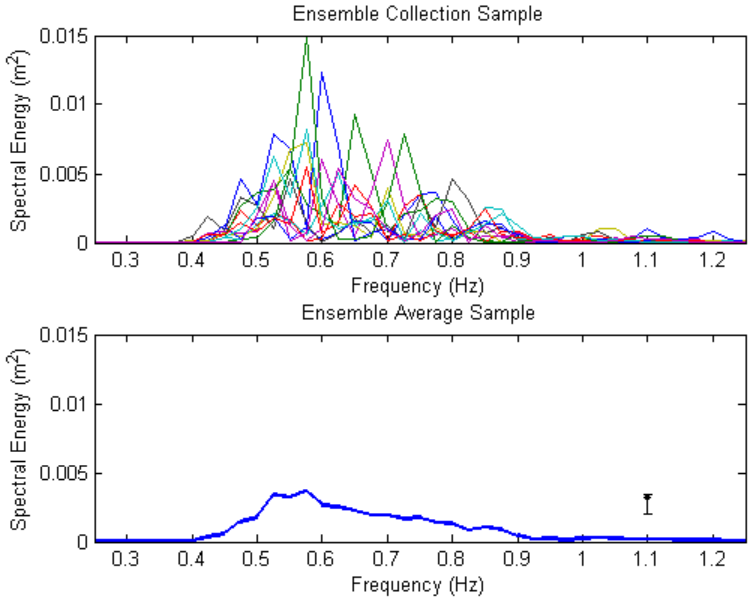

Figure 9: Many ensembles are averaged together from the top panel to get a single representative wave spectra of the entire time series in the bottom panel. Confidence interval plotted to the right.

keep *df* constant between these two sets of trials, and live with different levels of statistical significance. Although trial lengths of 313 seconds and 540 seconds were run, the best combination of N and *df* came from using 280 seconds of the shorter trials, and 480 seconds of the longer trials. With *df* constant, the resulting degrees of freedom were 28, and 48, respectively.

Confidence intervals for the spectra were calculated from the χ^2 distribution, and depend on the degrees of freedom, dof, the confidence level, α, and the spectral value, S. Upper and lower confidence bounds are calculated as:

$$Prob\left[\frac{dof}{q_{\chi^2\left[\frac{\alpha}{2},dof\right]}}S \leq S_{true} < \frac{dof}{q_{\chi^2\left[1-\frac{\alpha}{2},dof\right]}}S\right] = 1-\alpha$$

where S is the expected value of the spectral energy calculated by the methods outlined above, and S_{true} is the true spectrum. In the following analysis the confidence level is ninety-five percent. A function *PSDconfSpec* was created to find the upper and lower confidence interval bounds that could be plotted along with processed data spectra using the *errorbar* function in Matlab.

Characteristic Wave Statistics The primary wave parameters for real seas are significant wave height, H_s, and peak period, T_p. Peak period is determined by the inverse of the frequency bin that has the maximum energy of all frequencies in the energy spectrum, $f_{max} = max(S(f))$ and $T_p = f_{max}^{-1}$. The significant wave height can be measured as the average of the top one third of all wave heights recorded in each time-series, $H_{1/3}$. In the frequency domain, the significant wave height, H_{mo}, is typically calculated from the zeroth moment, $m_o = \sum S * df$, and defined as $H_{mo} = 4 * \sqrt{m_o}$. This thesis characterizes the significant wave height as $H_s = H_{mo}$.

2.2.3 Energy Flux and Power

Total energy flux is the spatial integration of energy flux. Energy flux per unit crest length, Ef, for monochromatic waves was described in equation 7, but the formulation to find energy flux of a spectrum is different. Unlike a monochromatic wave the energy spectrum contains many different frequencies of waves, all with different group velocities. Recall that $Ef = EC_g$; to accurately calculate energy flux in a spectral sea state, each frequency must be considered individually before a summation of energy flux can be made to characterize the data. Common practice is to calculate group velocity $C_{g,i}$ for each frequency, f_i, , multiply this value by the energy at associated frequency bin, S_i, and integrate across all frequencies.

$$Ef = \int \rho g * C_{g,i} * S_i * df \tag{14}$$

For regular waves the energy flux calculation must be multiplied by two because frequency integration for regular waves and real seas data yield different results (i.e., $trapz(f, S_f) = \frac{H_{m0}^2}{16}, \frac{H^2}{8}$, for real seas and regular waves, respectively), and was checked against numerous hand calculations of known energy flux for regular waves.

For this work we have only calculated energy flux for unidirectional conditions. Energy flux in multi-directional conditions will depend on the accuracy of the directional spectrum estimation, and will be perused at a later date. Net shoreward directed wave power was calculated as the longshore integration of energy flux. Because the six-gage offshore gage array and the six-gage lee gage array are both longshore transects, wave power passing through their respective footprints can be calculated and compared:

$$P = \int Ef * dy \tag{15}$$

which was done by the *trapz* integration method in Matlab. It was expected that the loss power loss between the two gage arrays should be approximately equal to the wave power absorbed by the WEC-array.

It is well known that WECs modify wave power in a frequency dependent fashion. In

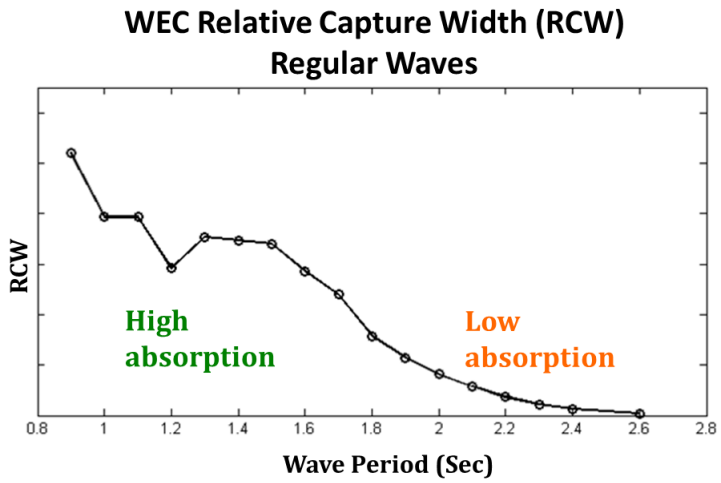

Figure 10: Qualitative relative capture width (RCW) curve for regular wave cases of the "Manta 3.1" wave energy converter

this thesis the frequency dependent relative capture width (RCW), or, the power capture relative to the available wave power within the longshore footprint of the WEC is analyzed. It was of interest to see if the same frequency dependent power absorption recorded by the WEC can be tracked from the offshore gage array to the lee gage array. Since WEC RCW is a ratio between units of power absorbed per unit width$[\frac{Watts/m/Hz}{Watts/m/Hz}]$, the wave gage comparison needed to be as well. In finding the energy flux for a single gage, the wave power spectra was also calculated; it is the energy flux before the frequency vector integration

$$S_{waveP} = \rho g * C_{g,i} * S_i * df \, [Watts/m/Hz] \tag{16}$$

The difference between the incident power and the power measured at the lee gages gives power lost from the wave field (deficit), at each frequency element. The ratio of power deficit to incident power gives relative power loss at each frequency, or the Relative Influence Width (RIW). It is characterized as influence because it is not a direct calculation of capture, but rather parametrizes the influence the WEC has had on the surrounding wave field.

2.2.4 Mechanical Power

Power takeoff from the "Manta" device was actuated by pitch motion of the float with respect to the nacelles (the wing-like objects on either side of the device). The nacelles rotated about the center float driving the linear damping, c. Mechanical power was calculated by

tracking relative position, θ, of the nacelles; for clarification of this geometry see Figure 2. Tracking enabled the calculation of velocity, $\omega = (\theta_{i+1} + \theta_i)/dt$, torque, $\tau = c\omega_i$, and power, $P = \frac{1}{N}\sum_i^N \omega_i \tau_i$.

Performance of the device was characterized by relative capture width (RCW), where $RCW = P/RPA$, and P is equal to mechanical power, and RPA is relative available power, or the amount of wave power available in the footprint of the device. Figure 10 shows qualitatively the RCW curve for the "Manta 3.1" wave energy converter device. The device was designed for higher relative capture in shorter wave periods.

To ensure the consistent comparisons, wave data and mechanical data processing and analysis has to be consistent. Only the following cases were included in RCW calculation: head-on regular waves with a target wave height of six centimeters, and head-on real seas waves with no spreading. Spectral analysis was needed to analyze real seas cases, and the same spectral methods as described in paragraph 2.2.2 were used. RCW for a single regular wave period was the mean of all RCWs for trials with the same nominal wave period. Similarly, for real seas each ordinate of the spectral RCW is calculated from all significant spectra in all repetitions regardless of WEC number. Spectral ordinates were considered significant in if the value was at least 0.5 percent of that spectrum's maximum spectral density. The number of trials for an ordinate ranges from two to twenty-six trials.

3 Results

Data analysis was extensive, and it was impossible to include all data analysis done on this data set in the following section. What follows are important aspects of the data analysis that follow along a critical path to the conclusions in this thesis. Results from regular waves with a target wave height of six centimeters and real seas trials with no directional spreading are presented. Reductions of wave height and power in the lee gage array due to the presence of WEC arrays are investigated.

The lee gage array (gages 11-16) best captures the wave height reductions in the basin that were due to WEC arrays since it is both the widest gage array shoreward of the WECs and is close enough to the WECs to have a large signal. As was shown in Haller et al. [2011], wave height reductions due to WECs are dependent on wave period. Figure 11 shows reduced wave heights in the lee gage array, it also shows incident wave heights in the offshore array and wave heights lateral of the WEC array in gage ten. It is clear that wave heights in the lee are reduced, and show a shadow like pattern with more reductions typically occurring near the middle of the array. The three WEC array case has some irregularities due to asymmetry in the array configuration.

Because in real seas conditions the WECs modify wave spectra at different magnitudes along the frequency domain, we compared incident wave spectra to the spectra measured in the lee of the array. Changes in spectral shape indicate at which frequencies the WECs are modifying the incident power and by how much. Alexandre et al. [2009] showed that if the WEC is tuned to the peak frequency of the incident spectrum, the leeward shape should be bi-modal compared to the single-mode incident spectra. Figure 12 shows statistically significant differences between incident and lee spectra for three and five WEC arrays, with five WEC arrays having larger differences. Lee spectra were characterized as the average spectra from gages thirteen and fourteen (see Figure 3), which are centrally located in the lee of the WEC array and have the largest wave height deficit. Incident spectra were measured for each sea state. Also shown are the 95% confidence intervals.

Differences between the incident spectra and the lee spectra change depending on the sea state, but one can see that at higher frequencies the differences are generally larger. At frequencies lower than 0.6 Hz there are no significant differences between spectral shape in any of the sea states. Although the shadow signals are smaller at higher frequencies, there was clearly more spectral modification from the WEC in this region. Unlike predictions by Alexandre et al. [2009], the resultant spectra are not bi-modal, but this is because the WEC is not tuned to a single wave period. Still some bi-modal characteristics were seen, especially in the Oregon3 sea state as seen in figure 12.

During the remainder of this thesis the incident wave characteristics for all target wave conditions are specified as the conditions measured during single WEC trials. That is, incident wave data for determining shadow magnitude in three and five device arrays is

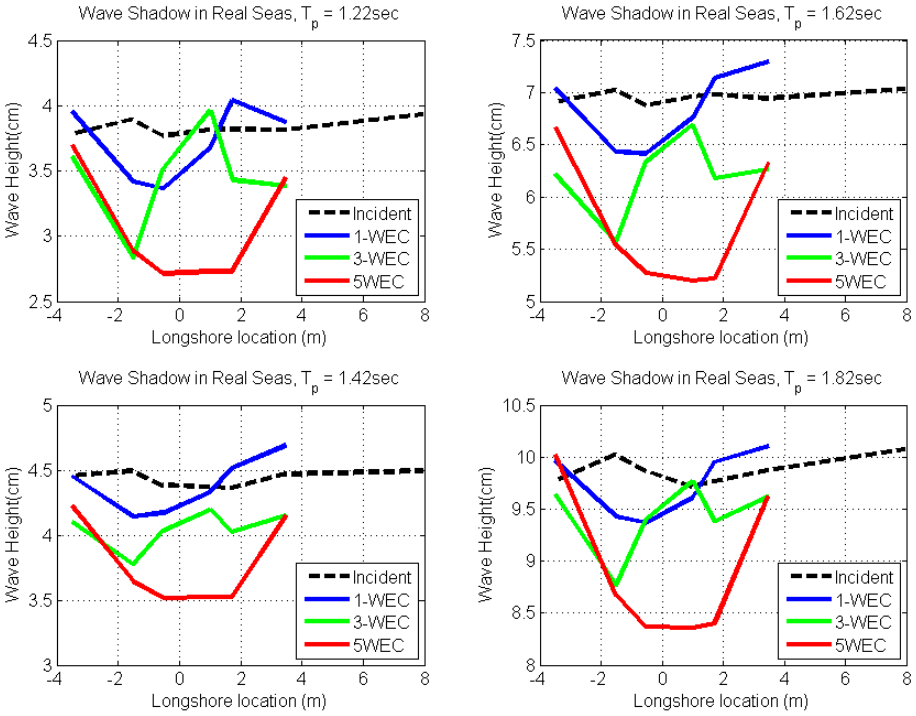

Figure 11: Wave height reductions in the lee gage array due to the presence of different sized WEC-arrays in four real seas sea states. Black is the incident wave condition, blue is the single-WEC case, green is the three device case, and red is from the five device case.

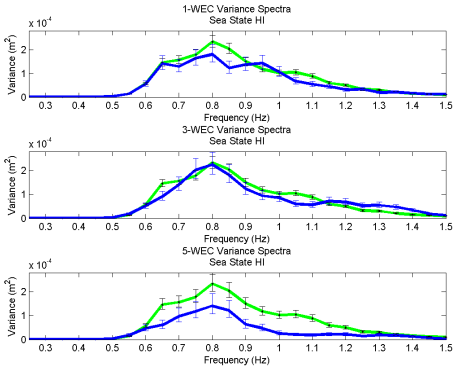

(a) Spectral Differences in Sea State: Hawaii

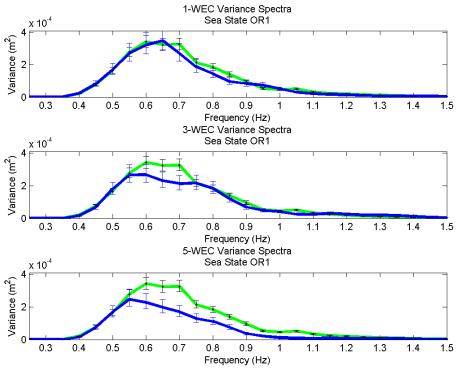

(b) Spectral Differences in Sea State: Oregon1

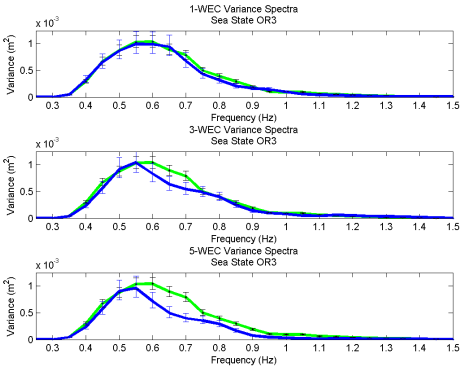

(c) Spectral Differences in Sea State: Oregon3

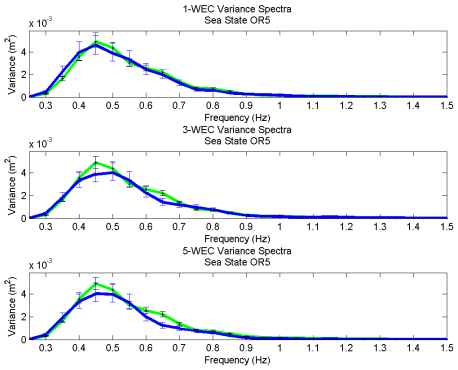

(d) Spectral Differences in Sea State: Oregon5

Figure 12: Measured changes to the variance spectra for four select sea states, between incident and the average of gages thirteen and fourteen in the lee of the array.

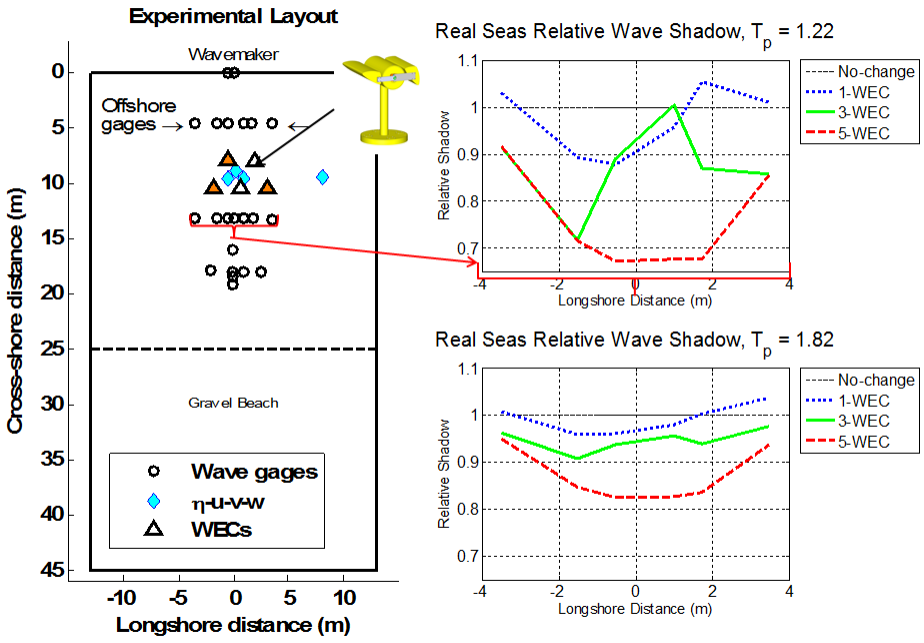

Figure 13: Wave Shadowing in two real seas trials (HI & OR3). The left panel shows where the the array shadow is measured in the experimental set-up. The right panel shows that more shadowing occurs in larger arrays, and in real seas with shorter peak wave periods.

from single device trials that had the same target wave conditions. This was done to reduce the influence of larger WEC arrays on the measured incident wave field. More on this can be found in Section 3.3. Using the wave data we now look at relative wave height reductions, with respect to the incident wave field. Figure 13 shows in the right panel relative wave height reduction plots in the lee of the WEC-array (wave shadowing) as a function of longshore location for two real seas sea states. The y-axis on this plot is relative wave height reduction, which is the ratio of wave heights recorded in the along the lee gage array with respect to the measured incident wave height. The red arrow indicates where the wave shadow calculations for the gages were made in the experimental layout. Black circles are the wave gages, triangles indicate the location(s) of WECs in the array, where orange triangles are the locations of the asymmetrical 3-WEC arrangement, and the blue diamonds locations of co-located current meters.

The total magnitude of shadowing was characterized as the power deficit between the incident wave field and the lee gages. Incident power was specified as the average energy flux from gages one through six and ten, and then multiplying by the length of the lee gage array. Conceptually the power deficit was the power lost between the offshore gages and the

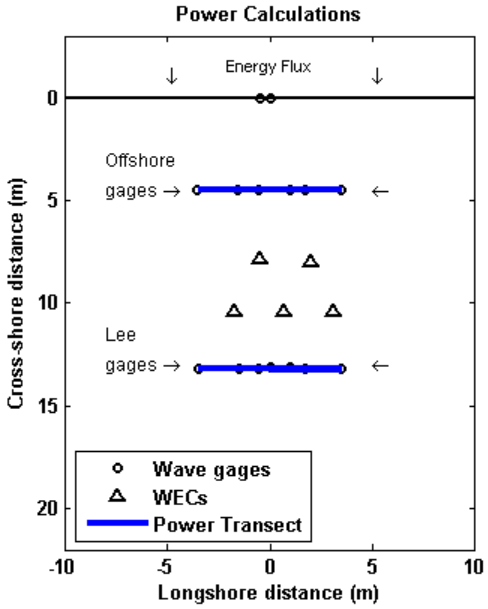

Figure 14: Power lost in the wave field is characterized as the difference between the incident power and the power measured at the lee gage array. Incident (offshore) power is the mean energy flux from gages one through six (the offshore gage array) and ten, multiplied by the width of the lee gage array.

lee gages due to the WEC array, as seen in Figure 14.

3.1 Monochromatic Wave Shadowing Analysis

Trends of wave shadow magnitude in regular wave trials are presented in this section, as are comparisons of these deficits to mechanical power capture measured from the WEC device. Also investigated were wave shadow magnitudes with respect to the incident wave power available, which gives a good estimate to how much influence the WEC-array had on a range of wave conditions. These results help to understand changes to the wave field in the real seas trials, as well as help to constrain future model results.

Energy Flux and Power WECs are designed to extract wave power; hence the power exchange from wave to device should be evident in the measured power loss of the waves in the basin. The WEC-Array Experiment data set has many trials to investigate the magnitude of this physical process, often there is more than one trial per wave condition. When the opportunity arose to average like trials, the wave data from the trials were averaged. Typically two trials were averaged; however, not all conditions contained multiple trials for analysis due to occasional bad data.

Analysis of the observed wave data showed that the power absorption ratio is frequency dependent, which is good considering that the WEC power generation ratio (relative capture width) is also frequency dependent. The relative capture width (RCW) of a WEC operating in isolation at a range of distinct frequencies was known: calculated by Columbia Power Technologies. Therefore a similar parameter should be designated for wave gage data. Relative influence width (RIW) is a proxy for shadow magnitude, and is calculated by the ratio of the relative power available (RPA) to measured power loss, where RPA is the incident energy flux multiplied by the nominal width W of a WEC (.55 meters), and by the number of WECs in the water.

$$RPA = W * Ef * \#WECs \tag{17}$$

$$RIW = \frac{P_{loss}[watts]}{RPA[watts]} \tag{18}$$

Measured power deficit and the Relative Power Available (RPA) from the regular wave trials are plotted in Figure 15. The parameters RPA and RIW are defined in equations 17 and 18. Measured RIW is the ratio of the measured power deficit in the waves to the RPA. Relative capture width (RCW) was calculated by Columbia Power Technologies from the measured power capture by an isolated WEC (see section 2.2.4), and corresponds well with the measured wave power.

The top panel of Figure 15 shows relative power available for the WEC-array as a function of wave period. This is the average incident wave power from the incident wave data set, multiplied by the summed longshore width of the WECs in the array for a given array size. For a given wave height RPA increases with wave period. The RPA curve reflects this trend with a leveling off at the higher periods due to a decreased wave height in those trials.

From 0.9 seconds to 1.9 seconds, there are significant amounts of wave power lost, which is mirrored in the RCW curve (lower panel), which was determined from the WEC mechanical power data only. At wave periods above 1.9 seconds the impact of the WEC-power absorption signal is likely not visible in the wave data above normal experimental variation and noise. In the wave periods where power absorption is present, the RIW curves for 3-WEC and 5-WEC are generally higher than the 1-WEC RIW curve, likely due to variability in the signal-to-noise ratio. At wave periods above two seconds, there is a consistent pattern of negative power loss, or power gain. This also is because of low signal to noise ratios. Wave power increases with wave periods given a constant wave height so it follows that errors in wave gage data are amplified in this region as well. It is known that the WEC was not designed to perform as well at these wave periods so it will have a small power capture.

The bottom panel of Figure 15 shows the ratio of power deficit (power deficit in wave data) to relative power available (RPA), this ratio was previously defined as relative influence

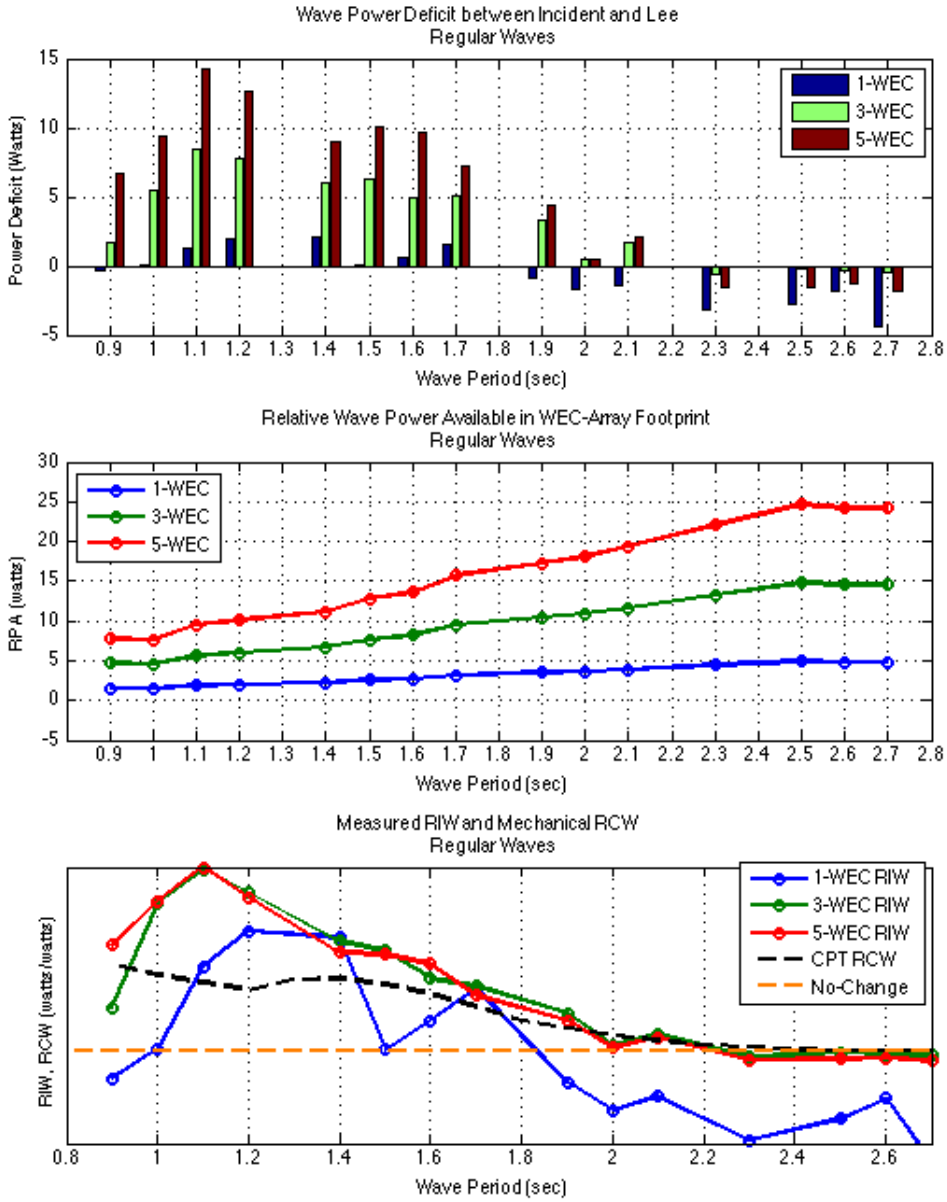

Figure 15: . The top panel shows the measured power loss, and relative power available (RPA) over a range of regular wave periods. The bottom panel displays the relative influence width (RIW) for differently sized WEC-array arrangements over a range of regular wave periods. The RCW curve is property of CPT so y-axis labels are not included.

width (RIW). RIW is plotted as a function of frequency for each array size, and against the mechanical RCW. The calculation for mechanical RCW is described in Section 2.2.4, and represents the performance of the device at different wave periods by the ratio of power absorbed by the device to the wave power available. Mechanical power absorbed (RCW) and power removed from the wave field (RIW) follow the same trends, decreasing in increased wave periods. In places where the magnitudes of the RIW curves are higher than the RCW curve this figure indicates other physics than WEC absorption are adding to the WEC shadow. Other physics must be present because the RCW only represents power removed by the wave field by WEC absorption. At shorter periods the differences between the RIW curves and the RCW are greater. The RIW for single device arrays is more variable because of low signal-to-noise ratio, as described earlier. More trust should be put into the three and five device results since their signals are stronger, and the fact that they are so similar gives even more reason to believe they are truly representing the power deficits in wave field. Because the power-based RIW curves between three and five WEC arrays are so similar, this implies at least moderate linearity of scaling between array sizes.

An additional parametrization of the linearity of power deficit between different WEC-array sizes is an investigation of the ratios of power deficits between different array sizes. If the relationships are completely linear, power absorption from the 3-WEC array, for example, should be three fifths that of the 5-WEC array. Figure 16 shows moderate linearity between 5-WEC and 3-WEC power deficits. The green dots represent the ratio of power deficit in the wave data from 3-WEC to 5-WEC, while the green line is equal to 0.6 which corresponds to perfectly linear scaling between array sizes. When the green dots are above the solid green line, this would indicate non-linear growth between array scaling, that is more power is removed than the nominal gain due to an increase in the number of WECs. Dots below the solid lines represent power deficits less than the nominal gain by the addition of WECs. Ratios of 1-WEC array deficits to 5-WEC deficits are extremely volatile due to the low signal-to-noise ratios in the 1-WEC array data as discussed earlier. Overall, signal-to-noise ratios are worse from left to right due to the amplification of wave gage noise and the decline in the WEC power absorption, which may help explain the very high ratios from 3-WEC to 5-WEC at higher periods. Periods over two seconds have not been included here because of the low signal-to-noise ratio. Within the range of decent signal-to-noise ratios, scaling between the array sizes appears to be moderately linear.

3.2 Real Seas Shadowing Analysis

Real seas analysis builds upon trends learned in regular waves analysis and is important for understanding what kind of effects WEC-arrays will have at in-situ commercial applications. This section details how the seven sea states (Oregon 1-5, Hawaii, and Ireland) are affected by different WEC-array configurations and directional spreading, by looking at power loss,

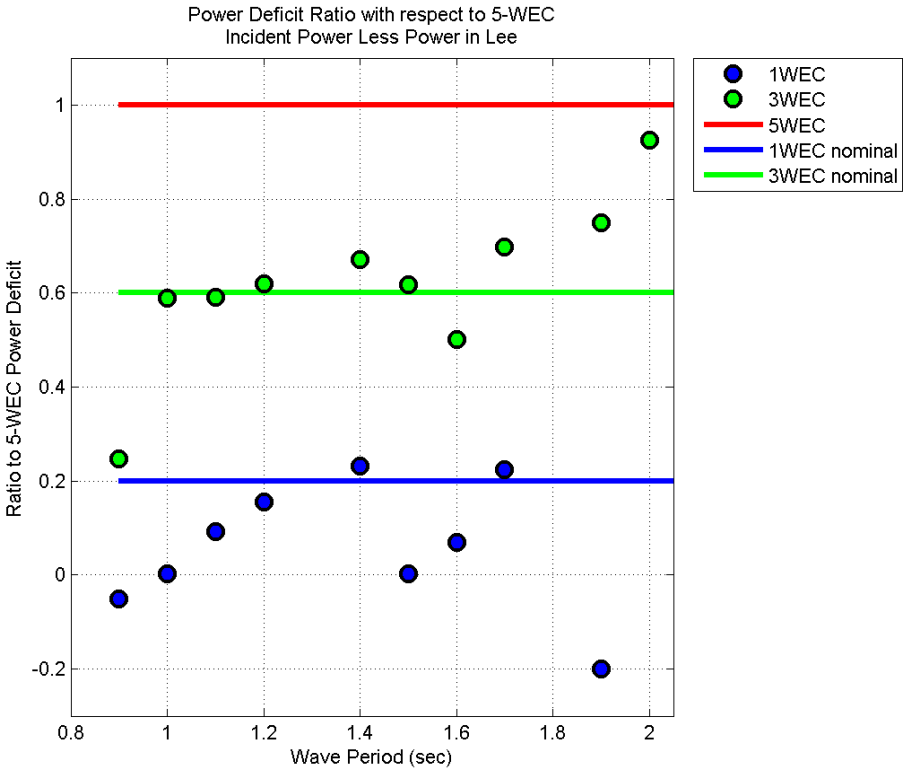

Figure 16: The green dots represent the ratio of power deficit in the wave data from 3-WEC to five WEC, while the green line is equal to 0.6 which corresponds to perfectly linear scaling between array sizes. When the green dots are above the solid green line, this would indicate non-linear growth between array scaling

Table 4: Real seas target wave conditions 2

Real Seas		
Sea State	**Wave height**	**Peak period**
	$H_{m0}(cm)$	$T_p(sec)$
HI	4.5	1.22
OR1	4.5	1.62
OR2	7.6	1.42
OR3	7.6	1.82
OR4	7.6	2.22
IR	10.6	1.62
OR5	13.6	2.22

and changes to the spectral shape. The sea states are described in Table 4

Energy Flux and Power This section will present results for linking power measured in the wave field to mechanical WEC power trends, and understanding the correlation between the two for real seas. Power deficits measured in wave spectra are investigated in bulk (summed across all frequencies) and frequency-dependent fashions. Several ratios were calculated to better understand to what degree the wave-field was modified, these were the relative power available (RPA), relative influence width (RIW), and the 5-WEC Power Ratio. A reminder as to what each sea state's characteristics can be found in Table 4.

This analysis will focus solely on unidirectional sea states. Directionally spread cases are not included because accurate calculations of shore-directed energy flux require directional spectra analysis, which have not been attempted yet. To accurately calculate power or energy flux in a spectral sea state, each frequency must be considered individually. The formulation for energy flux is described in equation 14. This section will describe how the bulk and frequency specific parameters of energy flux and power were attained.

Bulk parameters of energy flux and power were attained in a similar fashion to those parameters for regular waves. The incident wave power (as calculated in the incident data set) was compared to the power measured in the lee of the array; bulk power lost was the difference of the two. Relative power available (RPA) was calculated as as the average incident energy flux multiplied by the total footprint of WECs in the array. Bulk RIW was then the ratio of bulk power loss to RPA.

Frequency dependent parameters better inform as to how the WEC affect the wave field piece-by-piece; they can describe how the incident power has been lost on a frequency basis. Because energy flux can be evaluated at each frequency, so can power. Here, the wave power spectrum, which was described in equation 16, in units of [Watts/m/Hz], can be integrated in the longshore to obtain total power at each frequency for the domain of interest. This was

done for both the average incident wave power spectrum [Watts/m/Hz] and the lee gages array spectra [Watts/m/Hz], where both were integrated along the length of the lee gage array [meters] to obtain the wave power spectrum for each [Watts/Hz]. Power loss spectra was then calculated as the element-wise difference between incident wave power spectra [Watts/Hz] and the lee wave power spectra [Watts/Hz]. The relative power available (RPA) spectra [Watts/Hz] was calculated as the average incident wave power spectra [Watts/m/Hz] multiplied by the total longshore footprint [meters] of the WECs in the water [Watts/Hz]. WEC-array footprint width is characterized as the nominal width of of the device (.55m), multiplied by the number of WECs in the water (1, 3, or 5) to get a width in meters. Relative influence width (RIW) was then the ratio of the RPA spectra to the power loss spectra and is expressed in units of {[Watts/Hz]/[Watts/Hz]}, similar to equation 18, but at each frequency. This process was applied to wave data from the average of all unidirectional wave cases for each of the seven sea states.

Bulk power losses are calculated similarly for real seas as they were for regular waves. Bulk power parameters are shown in Figure 17 as a function of sea state. Incident wave power increases left to right, and peak period varies. In all panels the blue colors corresponds to 1-WEC, green to 3-WEC, and red to 5-WEC. The top panel shows that the Hawaii sea state has the smallest power deficit for each WEC arrangement, while Oregon5 has the largest. Some of the 1-WEC power deficits are negative due to low signal-to-noise ratios; as incident power increased so did the noise and in high period cases this overcame the low signal. The middle panel shows that the incident wave power is much greater Oregon5 than Hawaii. Relative influence of the WEC array was calculated as the ratio of power loss to power available. Relative influence width ratio is shown for each sea state in the bottom panel. Note that the WEC-arrays in the Hawaiian sea state had the largest influence, while the RIW for Oregon5 had much less. The RIW for single-WEC data is more variable than the three and five WEC arrays since the signal for single-WEC arrays is much smaller. Results from three and five device arrays give an good idea as to how the array modulated the wave field for each sea state since the signal-to-noise ratio was much higher. Generally, the RIW curve is higher in sea states with short peak periods, and drops in sea states with high periods (OR4, OR5), indicating the WEC has more influence in sea states with shorter peak periods. This was also true in regular waves, as seen in the bottom panel of Figure 15. Because the RIW values for three device arrays and five device arrays are very similar, linear scaling between array sizes may be present.

As with regular waves, a good estimate of the linearity of the power deficit between different WEC-array sizes was done by comparing the deficits of single and three device arrays to that of a five device array. If the relationships are completely linear, power absorption from the 3-WEC array, for example, should be three fifths that of the 5-WEC array. Figure 18 shows moderate linearity between 5-WEC and 3-WEC power deficits. The green dots

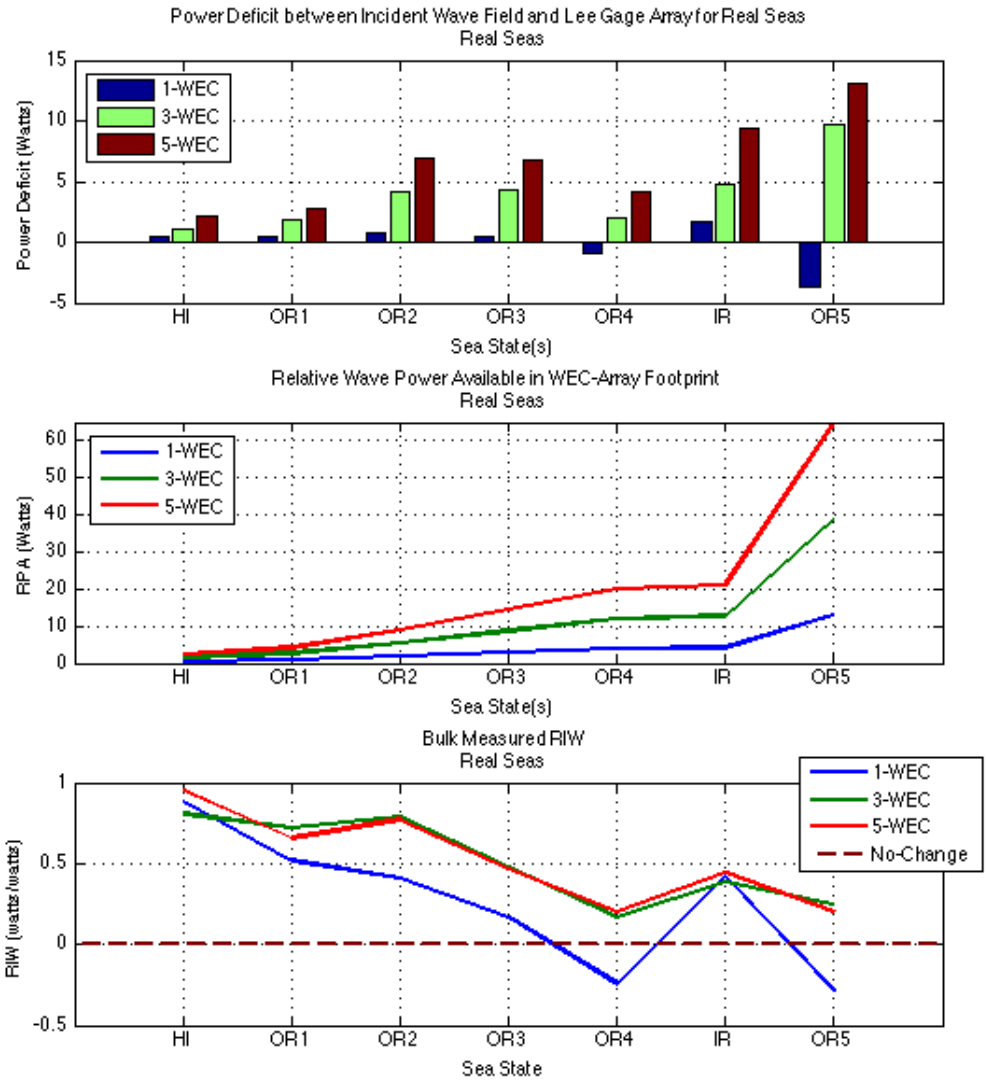

Figure 17: The top panel shows the measured power loss for each of the seven sea states. The middle panel shows wave power available in the footprint of the WEC-array. The bottom panel displays the relative influence width (RIW) for differently sized WEC-array arrangements for each sea state.

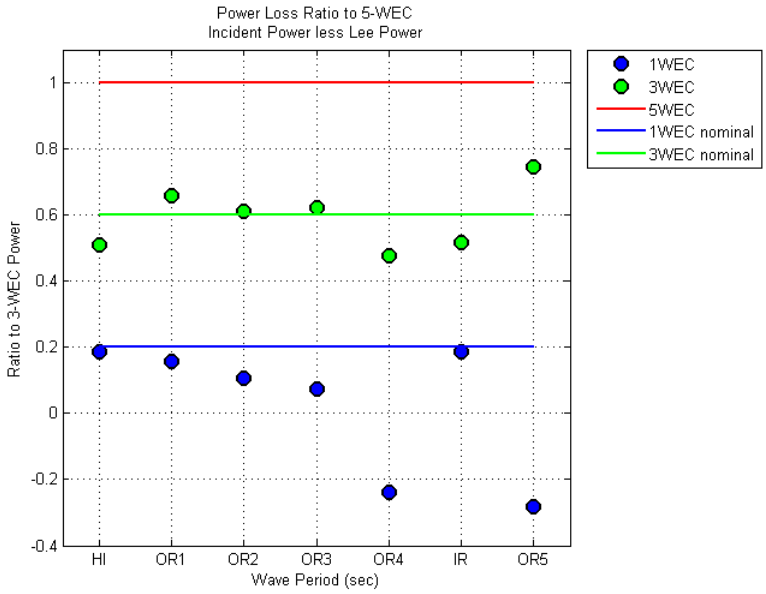

Figure 18: The green dots represent the ratio of power deficit in the wave data from 3-WEC to five WEC, while the green line is equal to 0.6 which corresponds to perfectly linear scaling between array sizes. When the green dots are above the solid green line, this would indicate non-linear growth between array scaling.

represent the ratio of power deficit in the wave data from 3-WEC to 5-WEC, while the green line is equal to 0.6 which corresponds to perfectly linear scaling between array sizes. When the green dots are above the solid green line, this would indicate non-linear growth between array scaling, that is more power is removed than the nominal gain due to an increase in the number of WECs. Dots below the solid lines represent power deficits less than the nominal gain by the addition of WECs. Ratios of the single-WEC power deficit were also moderately linear, except in the sea states Oregon4 and Oregon5 where there appears to be an increase in power. In these sea states the peak period was the highest (2.22 sec), therefore the shadow signal was lower than the noise signal. In sea states and arrays where the the signal-to-noise ratio was higher, this figure shows moderate linearity in scaling of array sizes.

Because the three and five device arrays have very similar bulk RIW curves and power deficits appear to scale moderately linear with size, we next examine how well these RIW curves match the mechanical relative capture width (RCW) curves. In real seas conditions the RCW curves were calculated in the frequency domain for each frequency. To compare the mechanical RCW to power loss measured in the wave field, the RIW spectrum is needed. Figure 19 shows power deficits from a 5-WEC array in the lee wave field as a function of frequency. Because of shadow signal strength considerations, only results from the five device

array are shown here. The top panel shows incident power spectra for seven unidirectional sea states; incident power from OR5 dominates since both the peak wave period and significant wave height were highest. The middle panel shows the element-wise deficit between the lee and incident power spectra, with OR5 having the largest signal. The bottom panel shows the ratio of deficit to incident power (RIW) along the frequency spectrum against the sea state averaged mechanical RCW (ratio of panels one and two). The fourth panel shows the seven point smoothed RIW against the measured RCW, which is easier to read than the unsmoothed one. This figure tells us that power deficits vary across the frequency spectrum in the wave data, similar to the power absorption in the mechanical data. In the high signal portions of incident spectra power deficit ratios were generally larger at higher frequencies, just like in the RCW. The level of power deficit ratios in the wave data varied by sea state. The Oregon5 sea state followed the RCW curve very closely, while sea states Oregon2 and Hawaii had the greatest deviation from the RCW.

A sea state specific RCW to RIW analysis was done to further investigate the correlation of mechanical power absorption to wave data power losses. The relative capture width measured for individual sea states under unidirectional cases only was compared to the RIW of the WEC measured in the wave data. Figure 20 on page 46 shows this comparison plotted on top of incident wave power spectra (blue dashed lines). Incident spectra are included in this plot to show at what frequencies the RIW/RCW comparisons are significant. Only RIW curves from three and five WEC arrays are included since the array signal was large enough in these cases to get a realistic RIW. Generally, the RIW curves for both three and five device arrays follow each other closely and are larger than the RCW curve across the frequency band of interest. In sea states with shorter peak periods (HI, OR2), the RCW and RIW diverge greater than in the sea states with larger peak periods (OR4, OR5). Similar results were observed in the RIW comparison to the average RCW seen in Figure 19 on the next page. Looking specifically at the RCW and RIW values measured at peak frequencies of each sea state is important because this is where the RCW will have the biggest impact on the wave field. Figure 21 on page 47 shows RIW and RCW values at the peak frequencies of each sea state. As frequency increases, so does the gap between RCW and RIW. At the low peak frequency sea states the RIW and RCW are very close, in the middle frequencies RIW values are slightly higher than RCW values, and in the sea state with the highest peak frequency (Hawaii) the RIW values are much higher than both the sea state specific RIW and average RIW.

Variations in the longshore transects of energy flux calculated from real seas trials are plotted in figures 22, 23 and 24 on page 51. This shows energy fluxes at the gages in the offshore (including gage ten) and energy fluxes at the lee gages as a function of longshore location in the wave tank. The red lines are associated with five device arrays, green with three device arrays, and blue with single device arrays. There were clear shadow structures

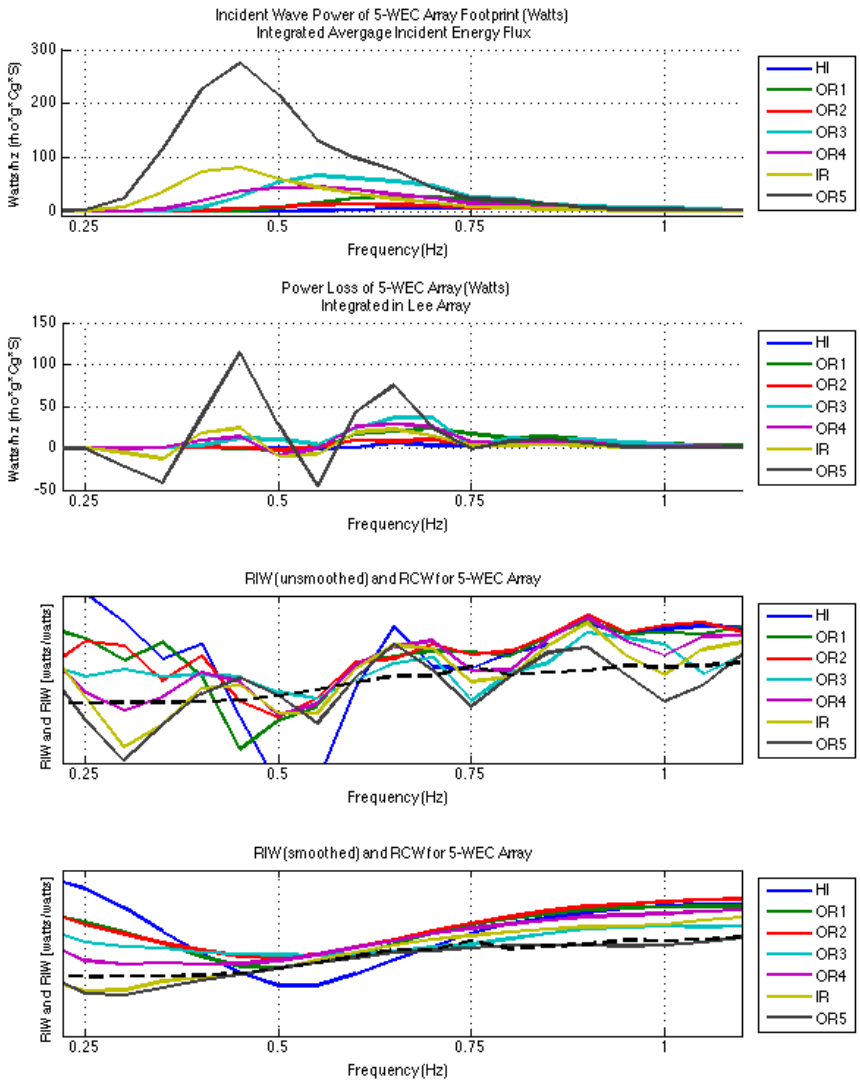

Figure 19: Power deficits in the lee wave field with respect to incident as a function of frequency. The top panel shows incident power spectra for seven unidirectional sea states. The middle panel shows the element-wise deficit between the lee and incident power spectra. The third panel shows the ratio of deficit to incident power (RIW) along the frequency spectrum against the sea state averaged mechanical RCW. And the fourth panel shows the seven point smoothed RIW against the measured RCW. The RCW curve is property of CPT so y-axis labels are not included.

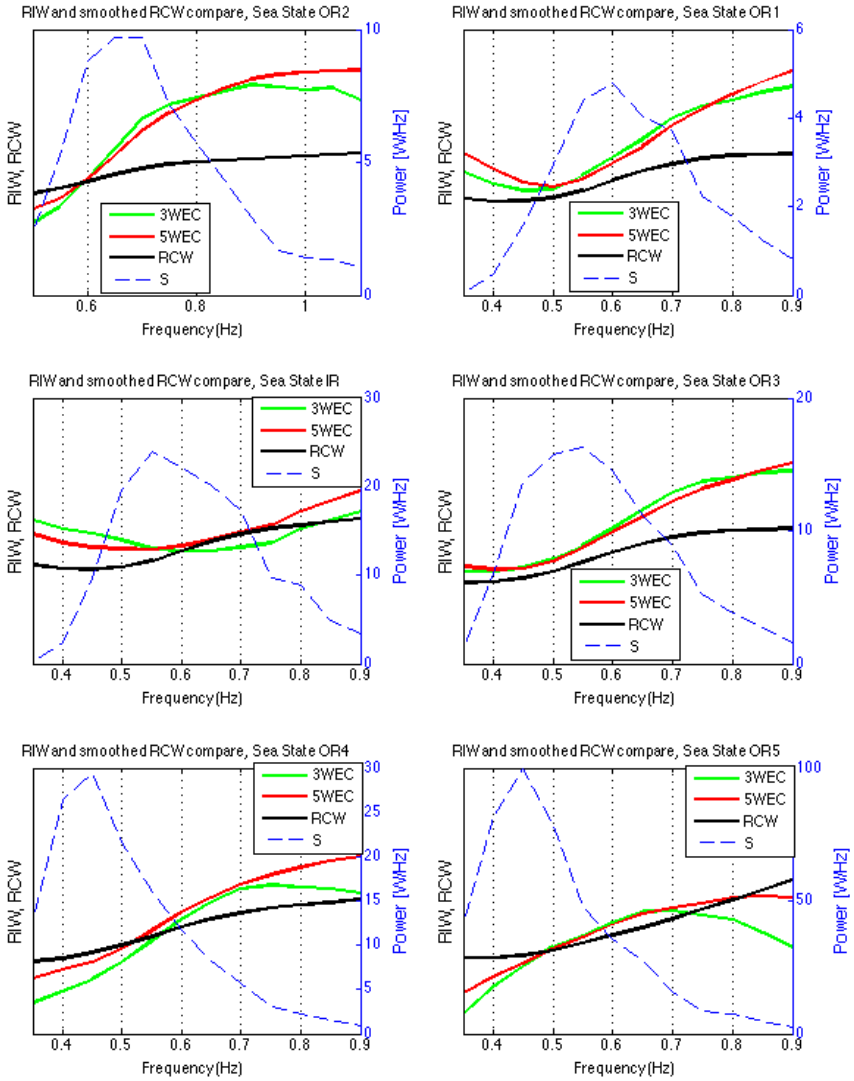

Figure 20: Power deficit ratios in the lee wave field for specific sea states as a function of frequency plotted on top of incident wave power spectra (Blue dashed lines). Green lines are the 3-WEC RIW, red lines are the 5-WEC RIW. Also pictured as the solid black lines are the sea state specific mechanical power RCW. Incident spectra are included in this plot to show at what frequencies the RIW/RCW comparisons are significant. Y-axis labels on the right side correspond to the incident spectra. The RCW curve is property of CPT so y-axis labels are not included for the left side.

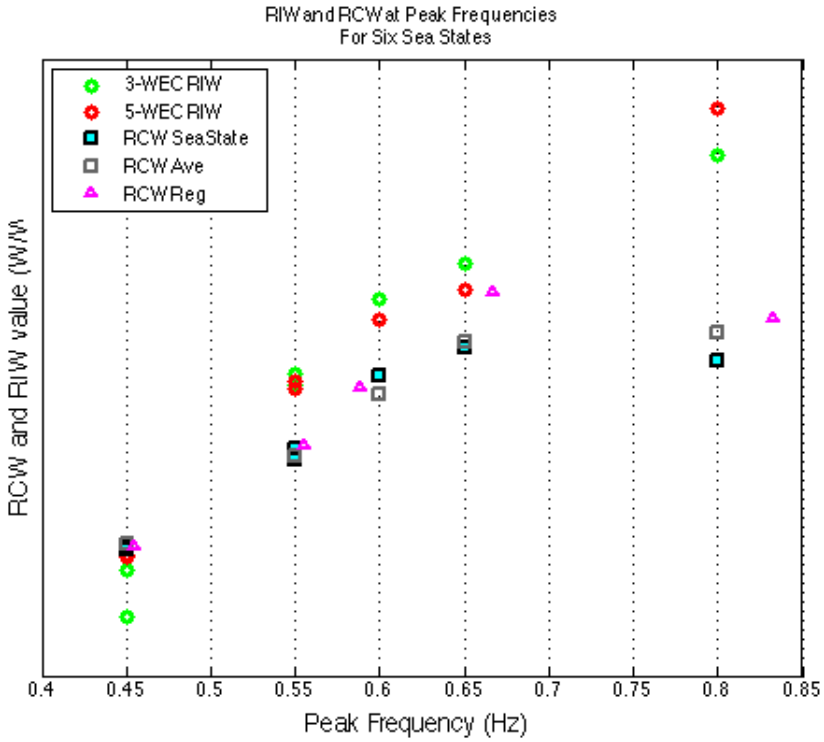

Figure 21: RIW and RCW values at peak frequencies of real seas sea states. The circles represent unsmoothed RIW values measured at the peak frequency of each sea state. Blue squares are the sea state specific RCW values, and the gray squares are the averaged RCW. Regular wave RCW values are plotted for reference as the triangles. The RCW curve is property of CPT so y-axis labels are not included.

present of all three array sizes in nearly all sea states, except for the single device array in the Oregon5 sea state. Of particular interest were the the shapes of the shadow in the three device array. It is easily seen that the shadow shapes have a distinct reflection of the asymmetrical array geometry, with two devices being placed towards the left side, and only one placed on the right side. Typically the shadows are deeper on the left than on the right in cases with three WECs, a direct result of array geometry. One more piece of information to note about the shapes of the three and five WEC shadows was that the shadow magnitudes at the extents of the lee gage array were nearly identical between the two sizes for all sea states. This means that the lee gage array captured the same portion of the longshore shadow for both cases, which was important for comparing power deficits between array sizes. It helps to validate linearity between array size scales.

3.3 Parametrization of the Incident Wave Field

The incident wave field for all shadowing and modeling analysis was determined to be best characterized by the mean wave parameters measured at gages one through six and ten for all like trials in regular waves and real seas. Characterizing the incident wave field was a difficult endeavor because of larger than expected WEC array influences on the offshore gage array. Wave data from single device arrays appears to have the least influence from the WEC arrays in the time, and frequency domains.

As shown in Figure 3, wave gages one through six are closest to the wavemaker, and were intended to characterize the incident wave conditions. As a group they are referred to as the “offshore gage array”. Gage ten, located approximately eight meters (or approximately fourteen WEC diameters) lateral of the WEC-array at nearly the same cross-shore distance as the array, was also intended to capture the incident wave conditions, with limited WEC-array influence. This section details how and why this argument is sound.

3.3.1 WEC-Array Effects on Incident Measurements

To analyze the best way to characterize the incident wave field, several analyses were conducted. To check whether the influences of the WECs on the incident wave field were not steady state, a comparison of power deficit ratios measured from only the first five waves of regular wave trials was compared to deficit ratios of wave data collected along the entirety of the steady state sample time. To investigate the effects of array size, longshore variability of incident wave height and spectra of real seas trials were evaluated for different array sizes. Accurate incident wave conditions were essential so that the relative wave shadow and power deficits from the wave field could be correctly determined.

Similar methods to that of those in Section 3.1 were used to provide an exact comparison, as shown in Figure 25. This figure shows the power deficit ratios from three and one WEC

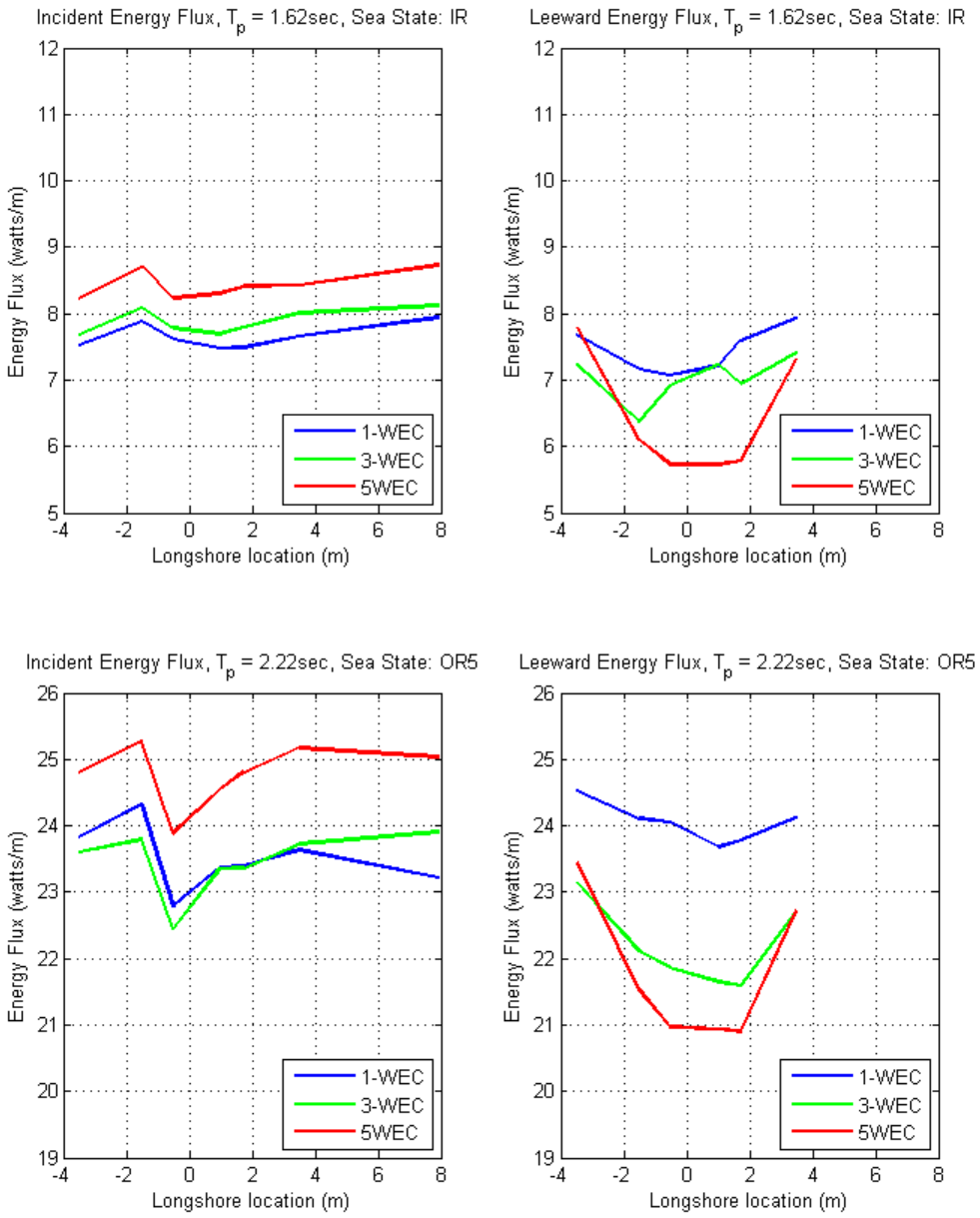

Figure 22: Longshore transects of energy flux in Ireland and OR5 sea states

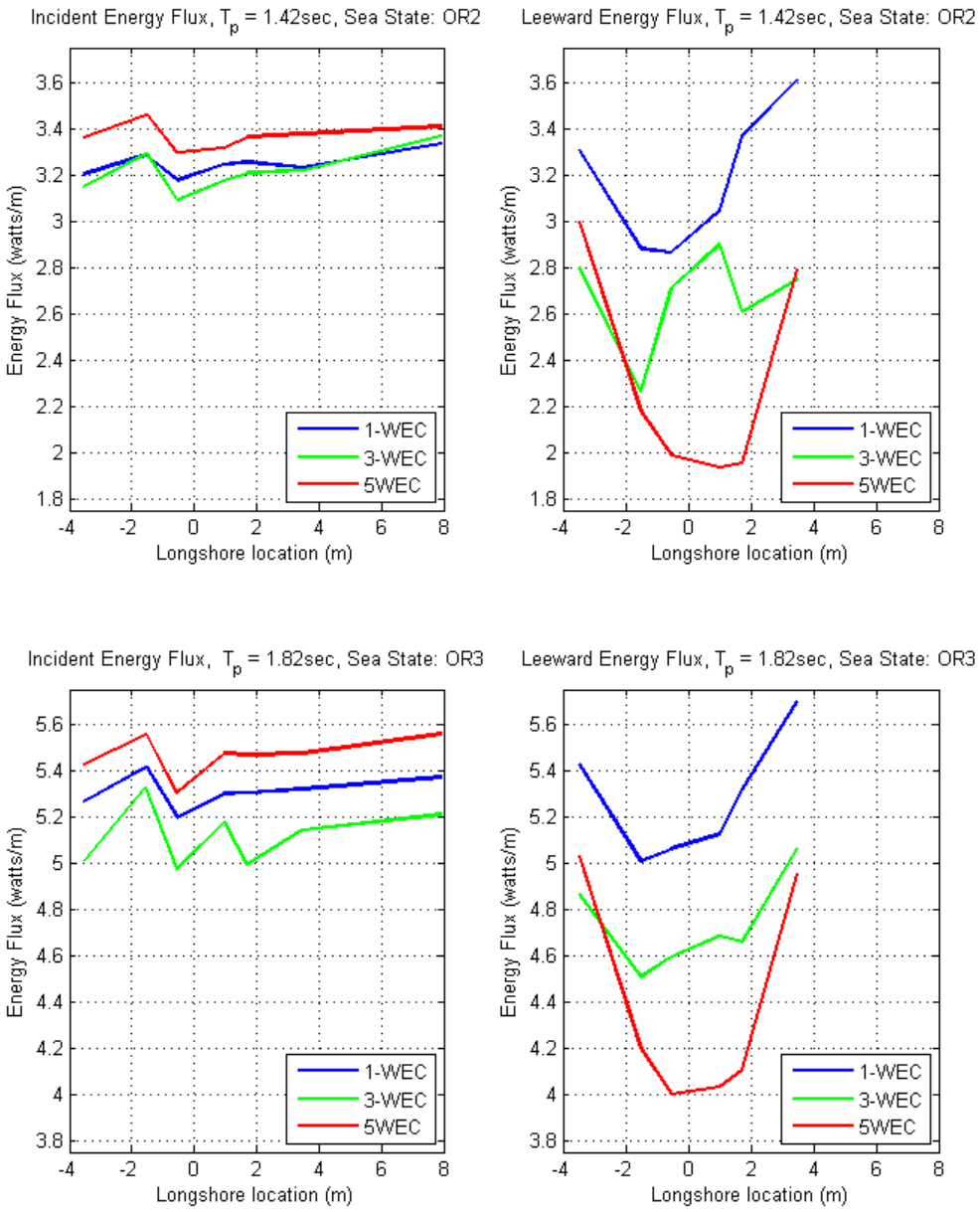

Figure 23: Longshore transects of energy flux in OR2 and OR3 sea states

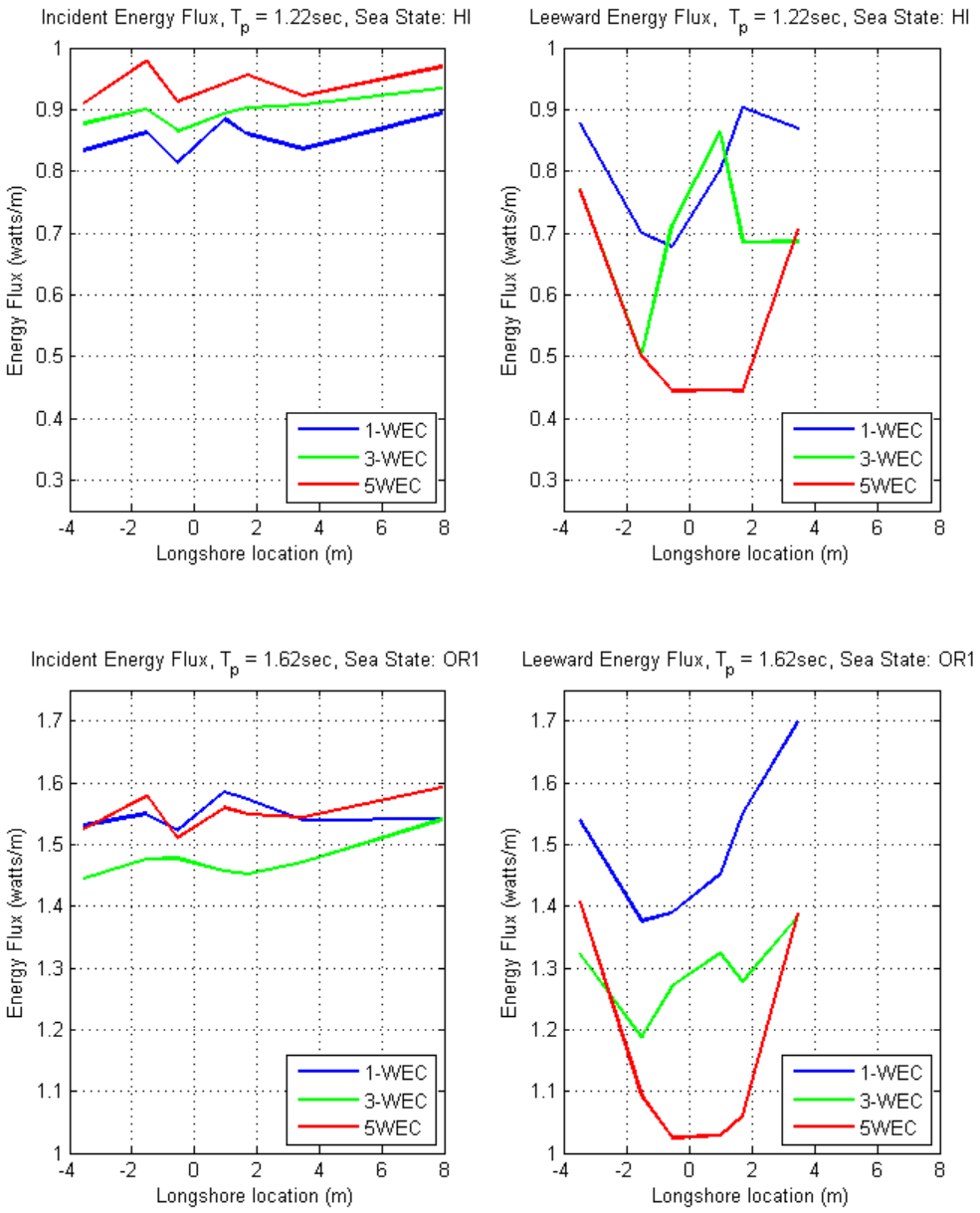

Figure 24: Longshore transects of energy flux in HI and OR1 sea states

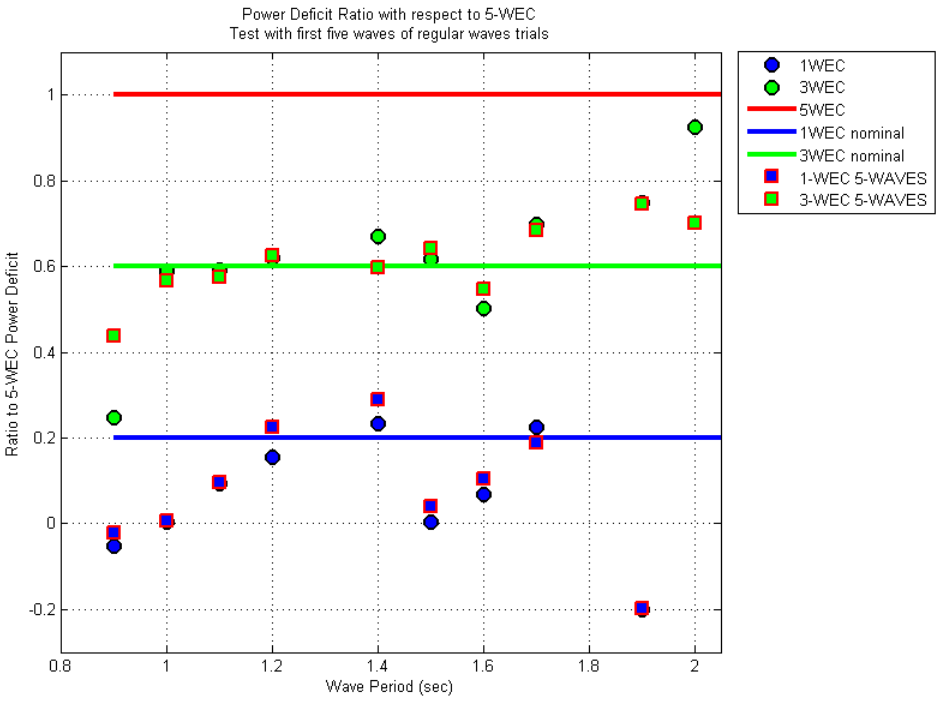

Figure 25: First Five Waves: WEC-Array Size Power Loss Ratios Compare

device arrays to that of a five WEC array in a suite of regular wave trials. The circles represent wave data from an entire trial, and the squares represent wave characteristics measured from only the first five waves in those respective trials. Because the differences between the circles and the squares are relatively minor, we can say that the WECs affect on the wave climate is consistent throughout the trial.

The results from an investigation of offshore wave height patterns from different WEC array sizes in numerous sea states is plotted in Figure 26. In all panels the blue colors corresponds to 1-WEC, green to 3-WEC, and red to 5-WEC arrays. These longshore transects of wave height show definite increased wave heights in 5-WEC arrays above 1-WEC arrays, and moderate increases in 3-WEC arrays above 1-WEC arrays. Effects from larger arrays on the offshore gages are pronounced, and likely would have an adverse effect on relative wave height reduction calculations.

On a spectral shape basis, the incident wave conditions also vary by array size. It has already been shown that the incident significant wave height was higher in larger arrays. Figure 27 shows that dependent on sea state, the single-WEC arrays have a peakier spectra than the three and five device arrays. Reduced peakiness in multiple-WEC arrays indicates an influence by the WECs on the shape of the incident spectra.

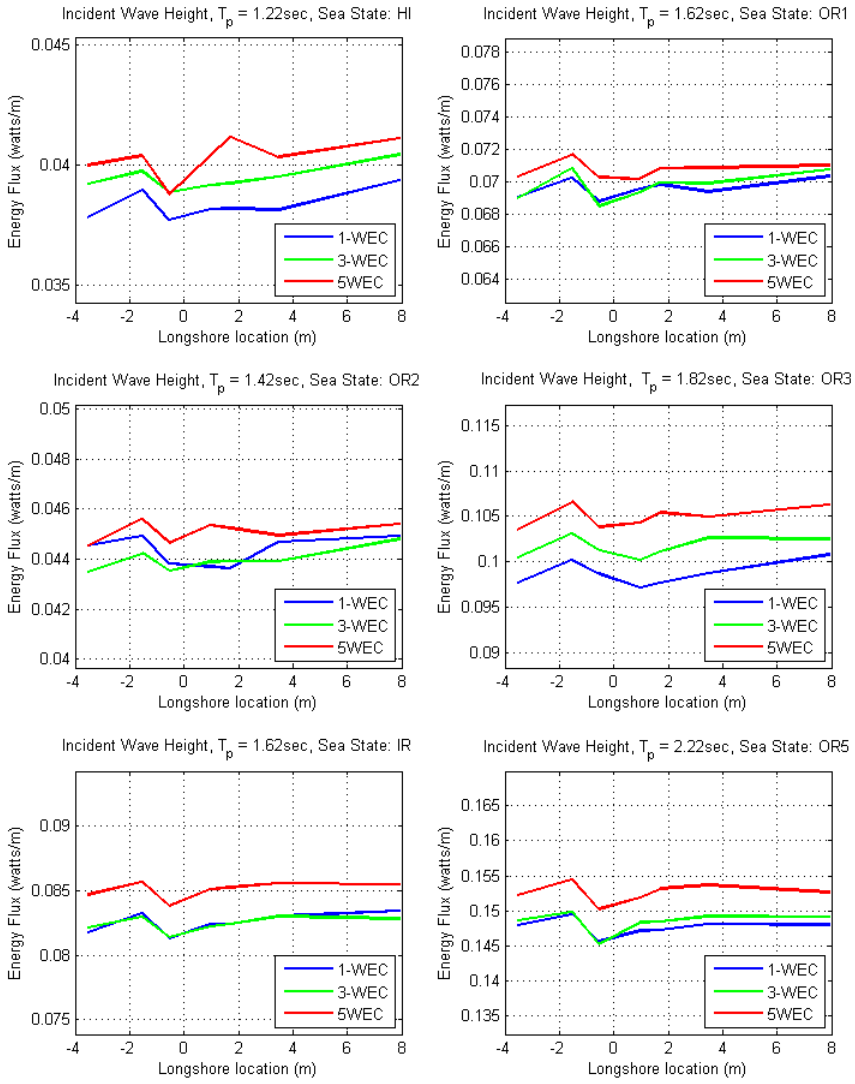

Figure 26: Offshore wave heights for six sea states in different array sizes. Blue lines represent 1-WEC arrays, green represent 3-WEC arrays, and red lines represent 5-WEC arrays. The 5-WEC arrays consistently have higher offshore wave heights.

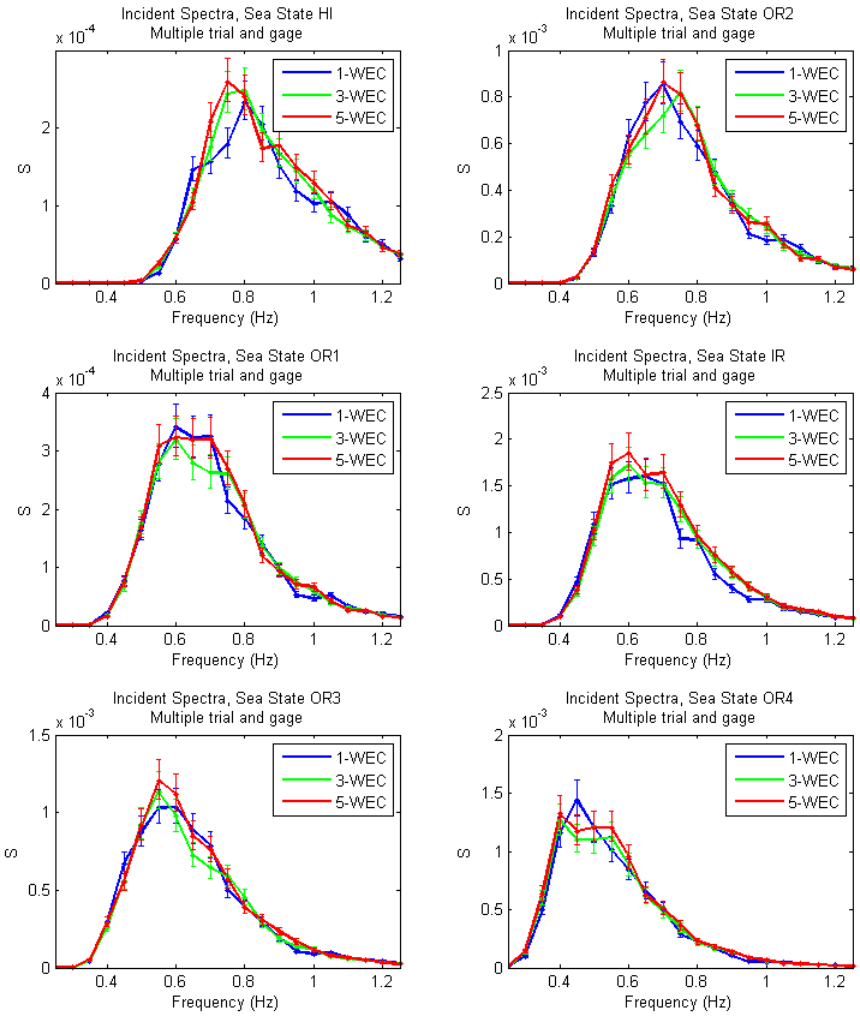

Figure 27: Measured incident wave spectra at forty-eight degrees of freedom, from one, three and five device arrays. In all panels the blue colors corresponds to 1-WEC, green to 3-WEC, and red to 5-WEC. Spectra were averaged from seven gages and two like trials. Confidence intervals were calculated from the χ^2distribution with associated degrees of freedom.

3.3.2 Phase and Coherence

To average the offshore wave gage with gage ten there must be a high level of confidence that the two sets of gages are experiencing the same wave field. If they are, results from the wave gages can be combined, which increases the degrees of freedom and decreases error bar size in the data set. Testing whether or not gage ten is statistically identical to the offshore wave gage array was done by calculating the coherence spectra. for spectra with twenty four degrees of freedom, the 99.999 percent confidence level, $\gamma^2_{critical}$, is 0.6489

Coherence spectra were calculated for all unidirectional trials of the seven sea states, in the five buoy array arrangement. It was expected that the limits of coherence would be tested in the 5-WEC arrangement due to a larger array, with increased WEC influence on the offshore gages. In this process similar trials were not averaged together to limit the degrees of freedom and run a more conservative test. It was found that the coherence at frequencies in the most energetic portions of the spectra (i.e., the portion of interest) was above $\gamma^2_{critical}$. Therefore gage ten is statistically identical to the offshore gage array for the frequencies of interest.

3.4 Laboratory Effects

3.4.1 Spatial Variance

A useful tool in analyzing this wave data is understanding characteristics of the wave basin in the absence of WECs, but in the presence of in-situ instruments and sidewalls. In this way the spatial variability observed in the wave data can be better interpreted. Since the wave basin is not infinitely wide or long, it will have certain natural frequencies that may create standing waves, and this could affect the wave data. Such standing wave shapes can be complex, occur in the cross-shore and the longshore directions, and will be different for each frequency and directional spreading case. Adding to the potential of spatial variance within the tank are possible reflected waves from the gravel beach; the beach was designed to reduce reflections, but it is not a perfect energy absorber.

Only a limited amount of data is available without WECs in the water. Eleven trials that were run to calibrate the Argus video system, which had no WECs in the basin. Data from these gives a glimpse into levels of spatial variability in the tank for regular waves and real seas. The seven were regular wave trials at three wave periods (T = 1.4s, 2.0s, 2.6s), and four real seas tests at two different wave periods (T = 1.42s, 2.22s) with varying levels of directional spreading (s = 10, 25). Wave data from these trials were processed into wave height transects in the longshore and cross-shore.

As shown in Figures 29 and 30, wave heights generally varied between +/- 5 percent of the mean incident wave height of the individual Empty Tank trials. This mean wave height was calculated as the average of gages one through six and gage ten. Tank behavior from

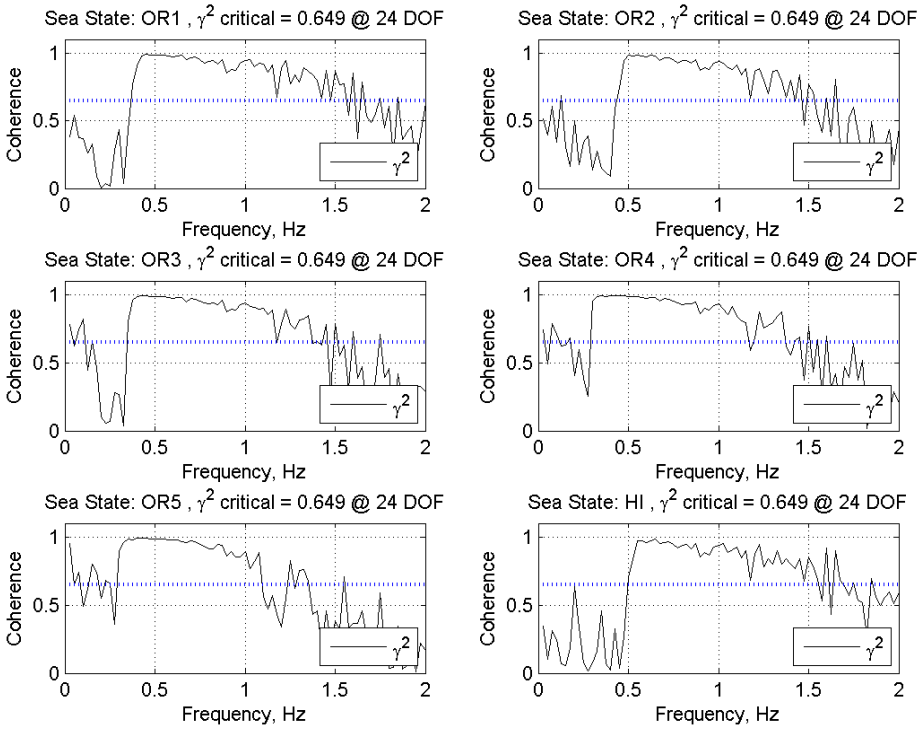

Figure 28: Coherence between gage ten and the offshore gage array. Computed during five-WEC array configurations for six sea states. The dashed line indicates the $\gamma^2_{critical}$ value, the solid black line indicates the coherence as a function of frequency.

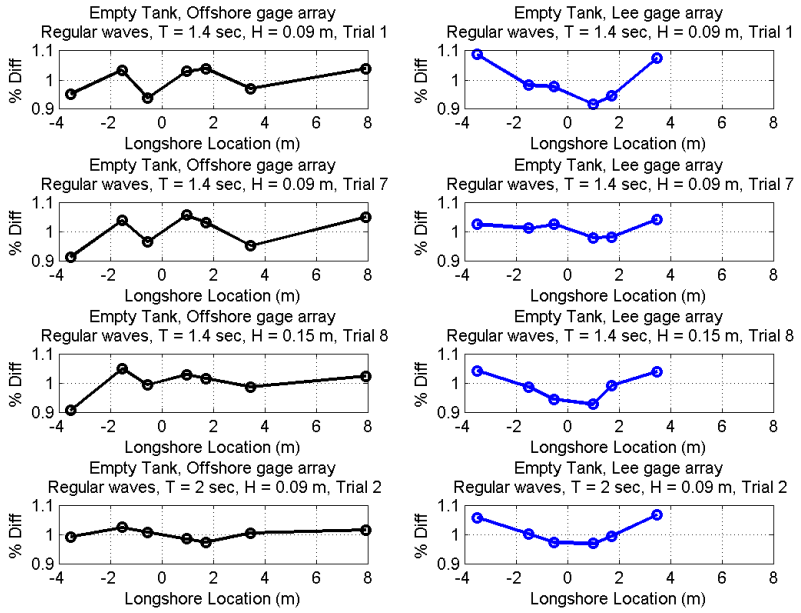

Figure 29: Empty tank analysis: regular wave longshore transects

multiple trials is shown in regular waves in Figure 29, and real seas in Figure 30.

Cross-shore wave height transects of the empty tank data were calculated from select gages near the middle of the basin except in the cases where there were many longshore gages such a cross-shore location, in which case the longshore average wave height was characteristic of that cross-shore location (i.e. offshore gages, lee gages, far-field gages).

To check cross-shore behavior in the empty tank, cross-shore transects of wave heights along the center of the basin were calculated and plotted in Figure 31. On the y-axis are the normalized wave heights with respect to the mean wave height of the offshore gages and gage ten, for each trial. This figure shows that wave heights in the offshore gage array are zero to five percent smaller than in the lee gage array (x = 13.2m) and far-field gage arrays (x = 18.0m). Although these percentages are small, there is a discernible pattern of higher wave heights closer to the beach than the wavemaker in both regular wave, and real seas wave fields. In real seas, the gage ten marker is zero to five percent less than the offshore gage array, but with no discernible pattern.

3.4.2 Cross-shore Beach Reflection

The beach installed in the wave basin during the WEC-Array Experiments was designed to dissipate energy to reduce the amount of wave energy reflected back towards the wave gages.

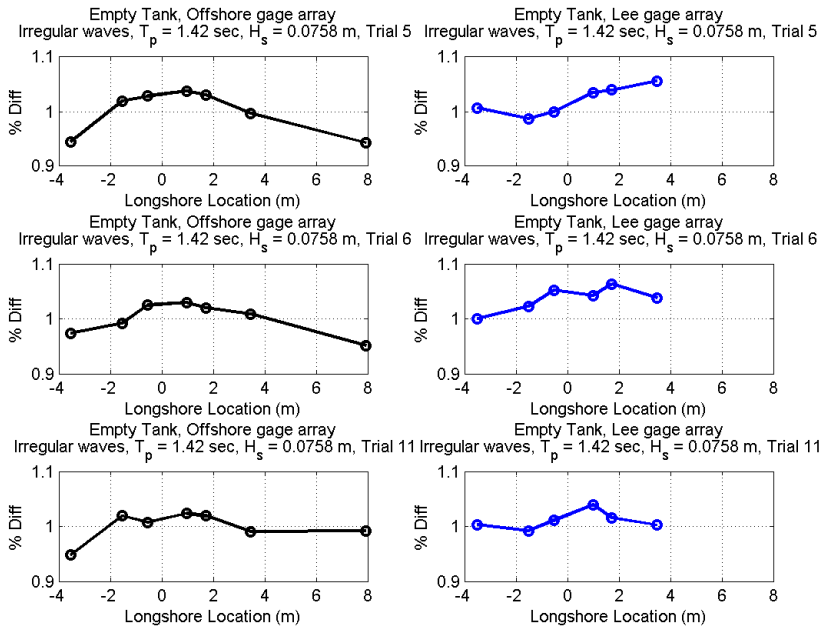

Figure 30: Empty tank analysis: real seas longshore transects

The far-field array was arranged with a closely spaced cross-shore gage transect in order to be able to resolve the incident and reflected wave components. To analyze reflection, a routine based off of Baldock's [Baldock & Simmonds, 1999] *ref_slope* code was chosen. Given two gages and their cross-shore location, depth, and sea surface time series, and collection rate, this routine will calculate the incident and reflected sea surface elevation time-series .

The best way to analyze cross-shore reflections is within an empty tank but, because of the lack of empty tank data available, 1-WEC trials were also analyzed as the best shot to understand beach reflection trends over many different sea states. Other tests such as three and five-WEC have a large signal due to the WEC-array effects and were not considered.

Regular wave trials from the *SingleBuoyCharacterization* tests was chosen as the basis for reflection analysis because it has more waves, fifty, than *SingleBuoyAmplitudeScan* or *SingleBuoyFrequencyScan*, which had twelve. Real Seas trials have a similar situation where the *SingleBuoyRealSeas* test ran a shorter sample time (313 seconds) than *SingleBuoyChar-RealSeas* (540 seconds), so the latter test was chosen for this analysis. A suite of frequencies was available for analysis, from 0.9 second waves to 2.8 second waves at an interval of one tenth of a second (except for 2.5 second waves). It is expected that longer period waves will have a higher reflection coefficient, as seen in previous experiments [Elgar et al., 1994].

At the onset of wavemaker action there should not be any reflection in the tank since

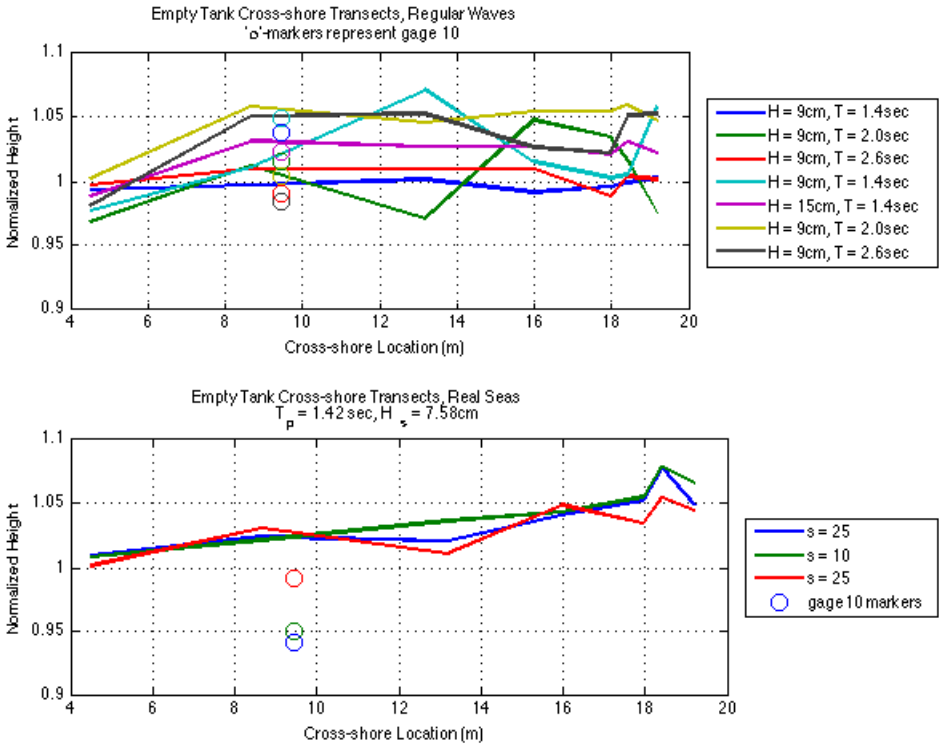

Figure 31: Wave heights from regular waves (top panel) and real seas (bottom panel) are plotted across the cross-shore extent of the empty basin. The longshore averaged wave height of each trial is indicated by a different colored line, and gage ten is plotted as a circle with the corresponding color.

the waves have not had sufficient time to reach the beach and reflect back to the gages. This analysis looks only at data that occurred in time after sufficient time had passed for the waves to reflect back to the far-field gage array. Wave speed was determined by the dispersion relationship and calculated for the peak frequency of each trial, and the time it took for that wave to reflect back to the far-field array was noted; only data past this point was considered for reflection analysis.

Reflection coefficients were calculated for regular and real seas wave conditions. The results from regular wave tests are shown in Figure 32. There appears to be a frequency dependence, however, the trend is opposite of what was expected i.e. there is increased reflection at smaller periods. The reflection coefficient is within the level of uncertainty measured by the empty tank data (+/- 5%). However, upon further analysis for trial numbers less than 130 the mean reflection coefficient was 0.052. These trials all occurred during the first fill/drain period (UTC dates 340-360, Figure 32 bottom panel) and show little dependence on wave period. Mostly the reflection coefficient is within eight precent. However, the trials performed after UTC date 390 show increased reflection levels for shorter wave periods. We suspect either that the separations algorithm is less robust for these cases (since time series including the reflection signal is shorter for shorter periods) or increased wave gage noise for these particular gages after the second fill.

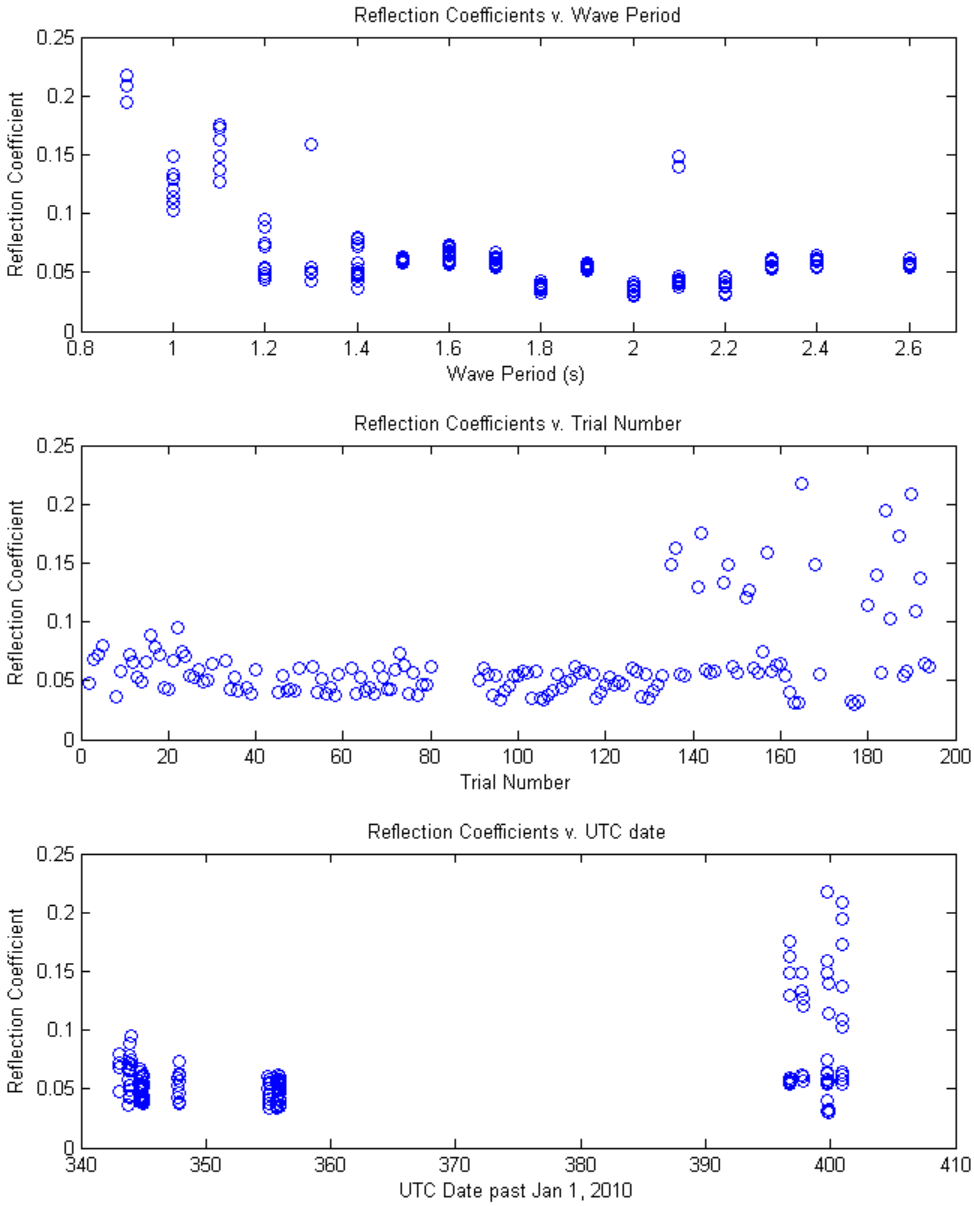

Figure 32: Reflection coefficients calculated from regular waves by Baldock's method. The top panel plots reflection coefficients as a function of wave period. The middle panel plots reflection coefficients as a function of trial number. The bottom panel plots reflection coefficients as a function of Coordinated Universal Time (UTC) date with Jan 1, 2010 as the datum.

4 Experimental Data Set Conclusions

Results from the extensive WEC-Array experiments have shown that the wave shadow is a function of wave period. Because the wave shadows is a function of wave period, and the same is true of mechanical WEC power capture, it can be concluded that a primary driver of wave shadowing is due to power absorption by the WEC. At certain small wave periods (T = 1-1.4 seconds) it was seen that the influence of the device on the wave field was not fully captured by absorption since the RIW curve was much higher than the RCW curve at these wave periods.

The data set is large, and has not yet been fully utilized. Future analysis should include more thorough real seas investigations since in-situ field applications will need to consider directionality. Whether this be in SWAN or some other model, the data set is extensive enough work with in almost any capacity.

Incident conditions for regular waves and real seas were best specified by wave data measured during 1-WEC trials at gages one through six and ten. Three and five device arrays showed repeated increased incident wave heights for the same conditions as in single device arrays. Measured incident spectral shapes of multiple device arrays were different than the single device array, indicating an influence by the WEC array on incident spectral shape as well. Getting the spectral shape correct is extremely important for modeling the effects of WECs on the wave field since the devices themselves modify the wave field on a frequency-wise basis.

Power deficits in the lee of the array with respect to the incident wave conditions have shown a great influence on frequency (wave period) and array size in regular waves and real seas trials. The scaling between three device and five device arrays is moderately linear for both real seas and regular waves. Shadow magnitudes calculated during single device array trials because of very low signal-to-noise ratios. Because scaling between array sizes has be shown to be moderately linear, several RCW curves measured from devices in isolation should do a fair job of representing multiple devices in a model. The relative influence of WECs measured in mechanical power (RCW) and wave power deficits (RIW) mirror each other well in regular waves and real seas, which tells us WEC power absorption is a primary driver of wave shadow behavior. Because the shadow is primarily driven by WEC absorption, the effect of the WEC array on the wave field may be able to be parametrized solely by absorption. At certain high frequencies (short wave periods) however, the RCW does not fully capture the influence of the WEC on the wave field, and it is likely that wave scattering has a significant influence on wave shadow magnitude and shape.

5 Numerical Modeling

This portion of the thesis compares WEC-array modeling results with the empirical data obtained and analyzed Section 3. Modeling was performed with the spectral model SWAN. Influences of WECs upon the wave field were parametrized by a frequency dependent sink function that was based on the behavior of mechanical power absorbed by a WEC in isolation. Three separate WEC-array sizes (1, 3, 5) were modeled, just as were tested in the WEC-Array Experiments. The analysis was limited to trial conditions with a normal incident wave direction and no directional spreading. Input wave climate boundary conditions for SWAN were taken from the empirical data collection described in Section 3.

SWAN is a third generation numerical wave model intended to compute short-crested waves based on spectral balances of wave action density [Booij et al., 1999]. In this case SWAN was implemented to imitate the WEC-array experiments in order to validate methods of WEC representation and modeling. The source code for SWAN was not altered, instead spectra at longshore transects within the domain were modified externally at several in-situ WEC locations by a transfer function that was based on WEC performance. This method involved several nested SWAN grids and mathematical manipulation external of SWAN calculations. The following section will illustrate why SWAN was chosen, the expectations of such modeling, the physics and settings in the models, explain methods of modeling WECs, and how well model results compare to experimental data.

5.1 SWAN Physics

SWAN was developed to numerically represent the effects of effects of spatial propagation, refraction, shoaling, wave generation, dissipation, and nonlinear wave-wave interactions. In order to accurately represent these effects, SWAN solves the spectral action balance equation:

$$\frac{\partial N}{\partial t} + \frac{\partial c_x N}{\partial x} + \frac{\partial c_y N}{\partial y} + \frac{\partial c_\sigma N}{\partial \sigma} + \frac{\partial c_\theta N}{\partial \theta} = \frac{S_{tot}}{\sigma} \tag{19}$$

where σ= radian frequency, N is the energy density $E(\sigma, \theta)$ distributed over radian frequencies σ and propagation directionsθ. The evolution of the action density, N, is determined in space and time; it is defined as $N = E/\sigma$ and is contained wholly on the left side of the equation. The right side S_{tot} is the sum of physical processes, or the "sources and sinks", that generate, dissipate, or redistribute wave energy. S_{tot} balances with the kinematics of the wave energy located on the left side of the equation. SWAN has six process that add to S_{tot} :

$$S_{tot} = S_{in} + S_{nl3} + S_{nl4} + S_{ds,w} + S_{ds,b} + S_{ds,br} \tag{20}$$

These terms, in order, represent: wave growth due to wind, nonlinear transfer of wave energy through three-wave and four wave interactions, wave decay due to white-capping, wave decay due to bottom friction, and wave decay due to wave breaking [SWANTeam, 2011].

5.1.1 Benefits and Limitation

As a spectral model, SWAN does not model individual wave forms, instead it tracks spectral energy in space and time as phase averaged quantities. This type of model creates both benefits and limitations. The major benefit is decreased computation time for large, management scale domains over varying bathymetry. A major limitation is that it cannot model constructive or destructive interference from multiple waves, or interactions between WECs. These limitations were kept in mind during modeling and interpretation of results. However, since SWAN is often used in field applications of coastal wave modeling, it is appropriate to use such a model herein.

5.1.2 Obstacles and WEC modeling

Typically in SWAN obstacles are modeled using the"OBSTACLE toggle in the input file, and choosing a relative significant wave height decrease, and locations of obstacle endpoints. Using this method results in energy being removed equally from all frequencies. WECs however, do not behave as such, instead the amount of power removed from the spectrum is a function of frequency. As of this thesis, the GNU SWAN releases do not have this capability. Although the source code has been modified by others to do this, such as the Wave Hub modeling group [Smith et al., 2012], we used an different method. One way to implement frequency dependent objects in SWAN is to nest SWAN at the each longshore transect of WECs in the array. Then to modify the wave field by a given transfer function outside of SWAN while it is stopped, and then run SWAN to the next cross-shore nest boundary. Whether it be it to the shore or to the next nest, it does not matter. Although reflection cannot be modeled in this way, it is not a goal of this paper to include such physics or inter-array interactions in the model since it is not expected that SWAN would be able to accurately resolve such near field physics.

5.1.3 Lateral Energy Spreading

Diffraction is the process of energy spreading laterally perpendicular to the direction of wave propagation [Dean & Dalrymple, 1998]. In this section diffraction was not enabled because we are more interested in accurately modeling downwave power of the wave field rather than the distribution of such energy. Additionally, the grid size resolution needed to resolve WEC geometry (10cm) was too fine for the diffraction calculations in SWAN to converge.

The SWAN manual suggests a wavelength to mesh size ratio of 1/5 to 1/10. Wavelength to mesh size ratios required to resolve the WECs herein was 1/40, approximately 10cm to 4 meter wavelength. Physics in SWAN do not account for diffraction, but it is approximated using the mild-slope equation. Later in this paper diffraction is toggled on during SWAN modeling for comparisons to WAMIT model results.

The Anti-Garden Sprinkler Effect (GSE) toggle in SWAN can also be used to increase lateral smoothing of the wave field to give a more realistic representation. Again though, lateral distributions of energy was not the main goal of this section. It is expected that a thorough sweep of GSE parameters could in fact eventually result in an accurate smoothing of the wave field, but not tried within this thesis.

5.1.4 Additional SWAN Physics

There are additional physics SWAN can model in addition to those listed above. SWAN has the capability to model wave breaking (BREAKING), white capping (WCAP), three and four wave interactions (TRIADS, QUAD), and bottom friction (FRICTION). Of these additional physics only wave breaking was turned on, the other physics were assumed to have minimal effect in such a small domain and in relatively deep water.

5.2 SWAN Model Simulations

Simulations of the WEC-Array experiments were done using SWAN. This section details how measured bathymetry and incident wave conditions, and WEC modification of the wave field were implemented in the computational grid. Because currently SWAN does not have the capability to internally model frequency dependent objects, and source code modifications were not attempted here, the wave field was modified externally from SWAN. Wave energy spectra at points in the longshore where WECs were located, were modified using the relative capture performance curve measured from the “Manta 3.1” WEC used in the WEC-Array Experiments. This section details the process in which spectra modification was done in conjunction with SWAN models.

5.2.1 Bathymetry

Bathymetric surveys of the beach were taken before and after the WEC-Array experiments occurred. The surveys were taken using LIDAR technology, by the OSU Geomatics unit, at a resolution of 5 cm, with a total number of points of 222,744. For the purposes of this experiment five centimeter spacing was not needed, so the original regular grid was interpolated to a 10cm regular grid. The 10cm grid was normalized by a nominal water depth of 1.365m, so that the survey is transformed from elevations to depth. Additionally,

surveys before and after show a slight change in shoreline bathymetry near the sidewalls, likely due to increased levels of positive interference in the surf-zone at these locations.

5.2.2 Incident Wave Spectra

Incident spectra for this modeling analysis come directly from wave data measured in the WEC-array experiments. The goal is replicate the incident wave data in the experiments as close as possible so that model results may be compared to experimental results. Here we model a frequency sweep of regular waves, and unidirectional wave spectra measured from the seven sea states listed in table 4. All of the incident spectra in this analysis are from unidirectional waves, so the directional spreading must be minimized. In this case the unidirectional spreading was minimized in the boundary specification line BOUND SPEC by calling the standard deviation of $DSPR$ equal to one, where $DPSR$ [SWANTeam, 2011] is equal to:

$$DSPR = \sqrt{\left(\frac{180}{\pi}\right)\int_0^{2\pi}\left[2\sin\left(\frac{\theta-\theta_0}{2}\right)\right]^2 D(\theta)d\theta} \tag{21}$$

Incident wave spectra were calculated from the mean wave characteristics of gages one through six and ten, from trials with 1-WEC present only, and are identical to the data used to evaluate wave shadow in Section 3. Further discussion on this can be found in section 3.3 on page 48. Regular wave spectra were determined by a parametrized SWAN spectra that contains energy only at the frequency bin nearest the nominal frequency of the regular wave. This means that the incident spectra for regular waves is not from measured wave data, it is instead from a parametrized spectrum for a single frequency, which SWAN calls a BIN-parametrized spectra. Unidirectional real seas spectra were input as the mean of the measured spectra from gages one through six and ten; the resulting degrees of freedom for these spectra are $48\frac{dofs}{gage} * 7\frac{gages}{trial} * 2trials = 672dofs$.

Regular Waves Boundary conditions in SWAN simulations for regular waves use measured mean wave heights from the gages one through six and ten from data measured in trials with a single WEC only, and are identical to the data used to evaluate wave shadow in Section 3. The wave periods range from 0.9 seconds to 2.7 seconds and all have a target wave height of six centimeters. It is apparent that the 1.3 second wave period case is not listed. Waves with periods of 1.3 seconds were run in the WEC-Array Experiments, but were not included in this analysis because of an initial quality control flag that was later dismissed.

Real Seas Boundary conditions for model simulations of real seas trials consisted of a characteristic incident wave spectra for unidirectional waves of each of the seven sea states

Table 5: Regular wave boundary conditions for SWAN

Regular Wave Boundary Conditions		
Wave Height (cm)	**Nominal Wave Period (sec)**	**SWAN Wave Period (sec)**
5.70	0.9	.913
5.36	1	1.00
5.70	1.1	1.11
5.62	1.2	1.22
5.41	1.4	1.41
5.54	1.5	1.47
5.48	1.6	1.62
5.64	1.7	1.70
5.50	1.8	1.79
5.47	1.9	1.87
5.41	2.0	2.0
5.43	2.1	2.06
5.52	2.3	2.27
5.59	2.5	2.5
5.45	2.6	2.62
5.37	2.7	2.75

outlined in Table 6. As outlined in Section 3.3 the incident spectra are averaged spectra measured from gages one through six and gage ten over multiple trials from single-WEC trials in the WEC-Array Experiments. The incident spectra for the models are exactly the same as the incident spectra used to calculate power losses in the data analysis portion of this thesis (Section 3). However, the frequency resolution in SWAN is different than in the experimental data. The spectra were interpolated to the frequencies outlined in Table 7, while also forcing the significant wave height to stay constant.

5.2.3 Computational Grids

Computational grids are the framework for solving the wave action balance equation that is the basis of SWAN. The grid contained two spatial dimensions, a frequency space dimension, and a directional dimension. The resolutions of these were determined by evaluating the convergence across a range and combinations of resolutions. There were three different computational grids, one for each nest, a process which will be described in more detail in section 5.2.7. These computational grids are summarized in Table 7.

Table 6: Real seas boundary conditions for SWAN

Real Seas				
Sea State	**Incident wave height**	**Incident peak period**	**Nominal wave height**	**Nominal peak period**
	$H_{m0}(cm)$	$T_p(sec)$	$H_{m0}(cm)$	$T_p(sec)$
HI	3.83	1.25	4.5	1.22
OR1	4.43	1.67	4.5	1.62
OR2	6.96	1.43	7.6	1.42
OR3	7.80	1.67	7.6	1.82
OR4	8.25	2.22	7.6	2.22
IR	9.87	1.54	10.6	1.62
OR5	14.7	2.22	13.6	2.22

Table 7: Computational grids used in SWAN modeling. X-origin is the geographic location in the cross-shore where each of the nested grids begins. The stitched grid is an overlap of each of the nested grids, with the shoreward nest having precedence beginning at each "X-origin".

Domain	Size	X-origin	Mesh Size	Mesh #	Directional	Frequency
	x, y	x_{low}	$\triangle x$, $\triangle y$	mx, my	$\triangle\theta$	$f_{low}, f_{high}, f_{num}$
	[m]	[m]	[m]	[#]	[degrees]	[Hertz]
Nest1	37, 26.5	0	0.1, 0.1	370, 265	4	0.3, 3, 48
Nest2	5, 26.5	8.2	0.1, 0.1	50, 265	4	0.3, 3, 48
Nest3	26.3, 26.5	10.7	0.1, 0.1	263, 265	4	0.3, 3, 48
Stitched	37, 26.5	0	0.1, 0.1	370, 265	4	0.3, 3, 48

5.2.4 Boundary Conditions

The Western open boundary of the domain was forced with the spectra described in section 5.2.2, while the Northern and Southern boundaries are modeled as parametric PM spectra with the same peak period and significant wave height as the measured spectra. In Nest1 the measured spectra was forced at each computational point in the western boundary, and was constant along the width. The Northern and Southern boundaries were parametrized as spectra rather than one hundred percent reflecting sidewalls to remediate previous problems seen with edge effects due to the presence of the walls. In subsequent nests the Western boundary is forced with the WEC modified spectra from the previous nest at all points in the longshore.

5.2.5 Output files

In each nested grid, wave data and spectra are output at all longshore locations along the shoreward domain. Significant wave height, peak wave period, dominant direction an are output at each point in the computational grid. In Nest1, spectra are also output at the offshore gage array location, a point it the middle of the domain, in addition to at the cross-shore boundary with of Nest2 (8.2m). In Nest2 spectra are output at the cross-shore boundary with Nest3 (10.7m). Finally, in Nest3 spectra are output at the lee and far-field gage array locations, the longshore transect of the lee gage array, and the longshore transect at the nest origin. Spectra output at the following nest's origin are then modified outside of SWAN to emulate WEC behavior, and then used as the input boundary condition in the next nest.

5.2.6 Spectra Modification

Relative Capture Width Curve The relative capture curve (RCW) is the ratio of available power in the footprint of a WEC to the power absorbed from the wave field by the WEC. It has been shown that RCW can be greater than 1.0, or more energy is removed than is available in the footprint [Budal, 1977]. Columbia Power Technologies calculated the RCW curve for both regular waves and real seas based off their calculations of power absorbed by a WEC in isolation. Power absorbed is measured by the square of relative pitch velocity multiplied by the generator damping. See Section 2.2.4 for more detail.

Regular Waves vs. Real Seas RCW curves are calculated differently for regular waves and real seas. In regular wave cases the RCW is calculated simply by the ratio of: power absorbed by the WEC per unit meter divided by incident wave energy flux (power) per unit meter. An individual RCW value was calculated for trials with different wave periods; the RCW curve is the stitching together of the wave period sweep.

In real seas the RCW was determined as the element-wise ratio of two frequency spectra: power absorbed per unit width [W/m/Hz] and incident wave power [W/m/Hz]. Power absorbed is the total power spectral density of the fore and aft floats. Input conditions vary over sea state, directionality, and generator damping. An RCW was calculated for each input condition and a mean RCW was calculated from these trials. The resultant curve was still peaky, so a seven point moving filter was applied for the final (spectral) RCW.

WEC as RCW Sink Measured RCW curves are intended to parametrize the WEC's performance, and be a gage as to how much energy is removed from the wave field in a frequency dependent basis. The inverse of RCW curves should then give an estimate to how much energy is allowed to pass through the WEC on a unit basis. Additionally, the resolution of the computation grid was 0.1 meters and the nominal width of the WECs are 0.55m, so a representative WEC width of 0.6 meters is needed. This means the RCW had to be scaled accordingly by $RCW_{scale} = RCW_{nominal} * [0.55m/0.60m]$. The transfer function or transfer ratio was then $ratio = 1 - RCW_{scale}$. Energy spectra were multiplied by this frequency dependent curve to determine the amount of energy passing through the spectra to be input back into SWAN, and represent the leeward wave field.

Interpolation of RCW to SWAN Frequencies The RCW curves used in this model are defined at frequencies other than computational grid frequencies, so they were interpolated to the SWAN (computational grid) frequencies. Without interpolation of the RCW to SWAN frequencies, the spectra could not be modified. Associated wave periods resolved in SWAN are described in Table 5 on page 67.

Location and footprint of WECs At each nest boundary, spectra at longshore locations associated with WEC locations for the given WEC-arrangement were modulated by the RCW-based transfer ratio. Figure 33 on the following page shows an example of spectra modification by the transfer function at locations in the domain. Sub-figure "A" shows the frequency dependent transfer function, $[1 - RCW]$, multiplied by the spectra at the Nest1/Nest2 boundary, given by the equation

$$Spec_{WEC,i} = Spec_{Nest,i} * (1 - RCW_{scale,i}) \tag{22}$$

where i are the frequencies within $Spec$ and RCW. Sub-figure B shows the locations that the modifications took place by the blue squares on the dashed lines.

The blue squares are the locations of the WECs along each nest boundary; they are the locations in which the spectra was modified as shown in sub-figure A, at all other points in the boundary the spectra remains un-changed. The WEC locations were determined by the mean position of the WECs during select measured trials, then were placed closest as

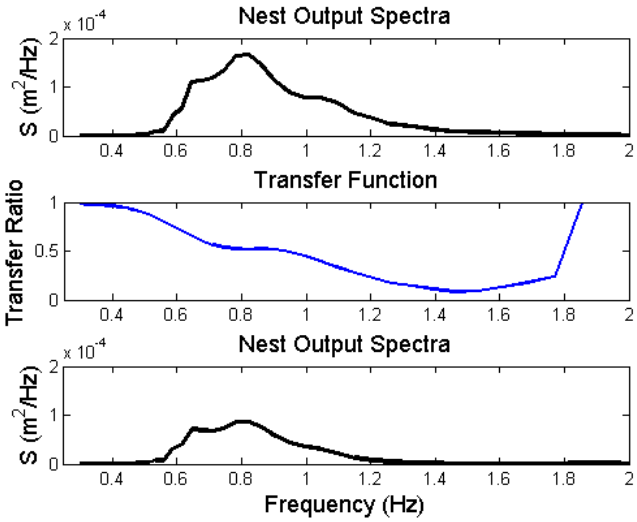

(a) An example of frequency dependent spectra modification. This modification occurs at each point in each nest boundary where a WEC is present. Otherwise there is no spectra modification.

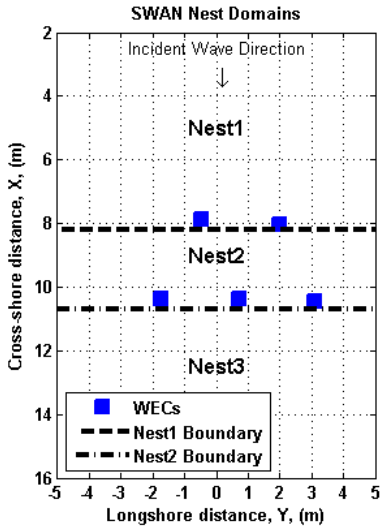

(b) Nests in SWAN models with locations of WECs. SWAN ran separately in each nest, with the spectra being modified by the RCW at longshore locations of the WECs at each nest boundary

Figure 33: The spectral modification process shown in sub-figure A is performed at WEC locations identified by blue squares in sub-figure B.

possible to those locations given the computational grid size resolution of SWAN.

5.2.7 Shell Script

Because currently SWAN does not have the capability to internally model frequency dependent objects, and source code modifications were not attempted here, the wave field was instead modified externally from SWAN. All of the processes listed above were included in a master shell script that ran the wrote the input files based on the incident data set for each case, ran each net within SWAN, and parametrized the WECs by transfer functions for both real seas and regular waves.

For each wave climate listed in Tables 5 and 6 on page 68 the incident wave conditions was determined by the incident data set, and then SWAN input files were written for each nest with with the current wave conditions. For regular waves the incident wave field for Nest1 was determined by BIN. In real seas simulations the incident spectra was the specified spectra of each unidirectional sea state. SWAN was then run for the Nest1, with spectra output at each location of the Nest1/Nest2 boundary (Nest1.spc). To represent the WEC influence on the wave field the WEC parametrization file "Row1PowerData" was run; it modifies the spectra (Nest1.spc) at WEC locations in row one for the current WEC arrangement. That file then wrote a new SWAN input spectra for all locations on the Nest1/Nest2 boundary (Nst2.bnd) which was used for the Nest2 SWAN simulation. After SWAN was run for Nest2, the spectra was modified by "Row2PowerData", which represents the WEC parametrization for row two of the array. The output from the external spectra modification (Nst3.bnd) was then modeled in SWAN to the shoreline.

The results from each nest were initially separate files, so it was crucial to combine the wave-field results into a single file. This was done in the shell script by cropping and patching the domains together in a piece-wise fashion. Energy flux calculations were done for each iteration within the shell script at nest boundaries, and at the longshore transect of the lee gage array. To calculate power at the gage array longshore transects, the spatial integration of energy flux in meshes along the transect was computed. To avoid including losses due to edge effects, the integration was cropped 2 meters (20 meshes) from each edge of the longshore boundary. Power deficits in SWAN were the difference between the incident wave power measured at the offshore gage array transect, and the wave power measured at the lee gage array transect. Power loss calculations for each trial were saved in each loop iteration, along with the raw spectra, energy flux calculations at each locations, and the wave height field for model to data comparisons. Because diffraction was not viable and sea states with directional spreading have not yet been characterized in the empirical data set, replicating the exact shape of the wave shadow was not considered a goal of this section. Therefore, the best way to compare model results to empirical data was to compare power deficits, and not wave height distributions.

6 Model/Data Results

Results from the SWAN model to the empirical data set showed that parameterizing WECs solely as power absorbers in SWAN does a fair job of predicting the wave shadow magnitude. They also showed that at shorter wave periods there must be some other physics present that affect the wave shadow.

6.1 Spectral Model and Comparison to Wave Data

The SWAN model can output wave heights, energy flux, radiation stress, and many other wave characteristics; this portion of the analysis we primarily evaluate energy flux. However, to check model output for quality control purposes wave height plots were produced. Figure 34 shows the significant wave height field for a 5-WEC array with the Oregon1 incident wave spectra. Although the incident wave field is unidirectional, and diffraction is turned off, some directional leakage occurs due to coarse directional resolution. Since no lateral spreading occurs due to wave physics, the directional leakage causes GSE like patterns further in the lee of the array. While these could be significant for field application, the shape of the shadow is not what we are after; here we have looked at power only. For reference, the lee gage array is located at a cross-shore distance of 13.2 meters. At this location the distinct shadow shape structures evident, and clearly very minimal shadowing occurs outside of the region directly in the lee of the array since no lateral spreading physics have been turned on. Figure 35 takes a closer look at the lee wave gage array transect by plotting the energy flux values of the model along this transect, and comparing to empirical data from trials with the same incident wave conditions. Most noticeable are the peaks and troughs of energy flux of the SWAN results by the red line; the troughs approximately correspond to the longshore locations of WECs in the array. The green line represents the energy flux shadow measured in the empirical data; it's shape shows lateral energy spreading. Clearly the edge of the shadow from the empirical data set is not resolved by the gage array, so the power losses could be slightly underestimated.

Because incident wave conditions in SWAN are intended to match those of the incident data set it was important to check the incident wave conditions of the SWAN results. SWAN did a good job of resolving the true incident wave climate. For example, take note that the Oregon1 sea state has a target significant wave height of 0.0454 meters, and the incident significant wave height in figure 34 is very close to that. Figure 35 shows energy flux transects of the offshore and lee gage arrays for model and empirical data results of the same case shown in Figure 34 (Oregon1). Incident energy flux values were nearly the same for model and empirical results. The difference between energy flux values of empirical data and model results is likely because frequencies in SWAN are not exactly the same as in the empirical data set, which creates small changes in the group velocity of each waveform, and hence the

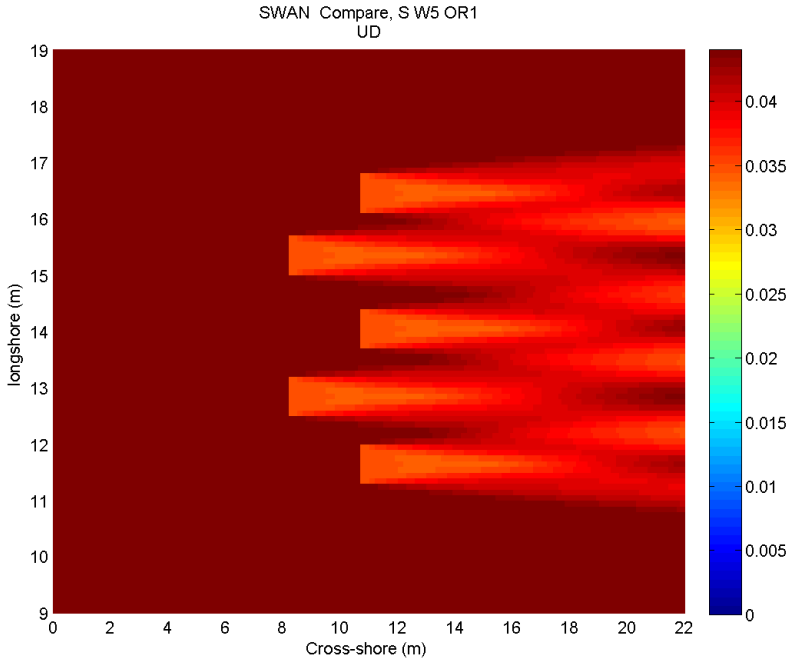

Figure 34: Typical SWAN significant wave height field result from a 5-WEC array with no directional spreading or diffraction. Units are in meters. Some directional spreading occurs due to directional mesh resolution, which also results in interference patterns in the lee. Bright colors represent more shadowing.

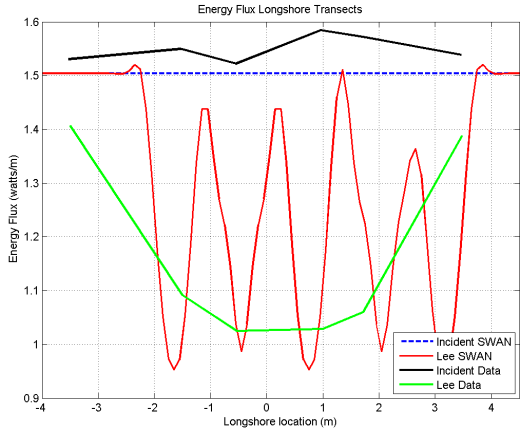

Figure 35: Typical model to data comparison of incident and lee energy flux transects. Data is from a 5-WEC array with no directional spreading or diffraction. Some directional spreading occurs due to directional mesh resolution. The blue and red lines are model results, black and green lines are empirical data results.

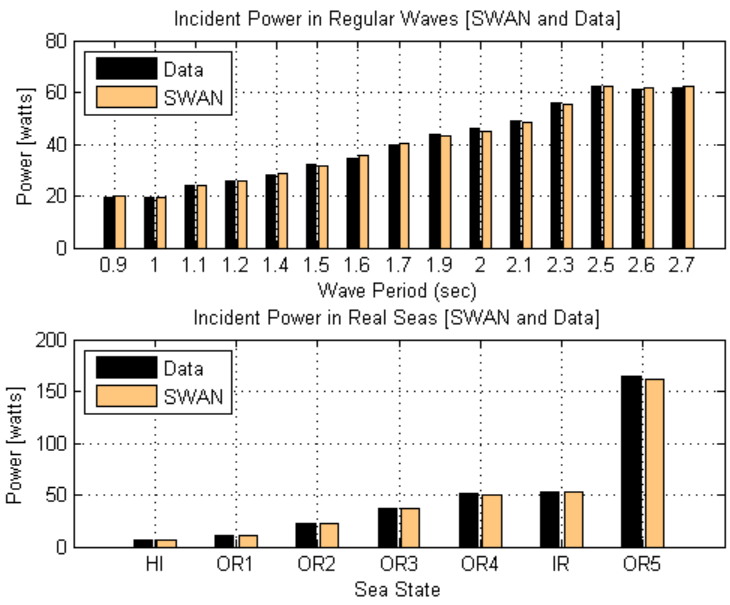

Figure 36: Incident wave power in empirical data (black) and SWAN results (copper). Because incident power in the model and the empirical data set were nearly the same, we have confidence in shadow results. Small variations occur due frequency resolution limitations in SWAN.

energy flux. These small differences occur in all wave conditions, but Figure 36 shows that such differences over all regular wave and real seas conditions tested are minimal.

Previously in this thesis, the influence of WEC-arrays on the waves was measured by the power deficit observed in the lee gage array relative to the incident wave conditions. The same method was applied to model results. Power deficits measured in the wave data from the WEC-Array Experiments were compared to deficits calculated from the model results for the same incident conditions. Figure 37 on page 77 plots this comparison from single, three, and five device arrays in regular wave, and real seas conditions. The black bars correspond to the empirical data set, and the copper bars correspond to model results. On the left side of the figure results from the regular waves tests are displayed. It is clear that in the 1-WEC case, the empirical data set is variable and that very little conclusions can be made. Power deficit calculations from the empirical data set for the single device array are variable because of small signal-to-noise ratios. The incident power in a typical regular wave case was anywhere from twenty to forty watts, while SWAN predicted power deficits of one to two watts. Resolving a change signal on the order of three percent in the lab environment would be difficult with natural variability of these experiments around +/- 5%.

Power deficits in regular waves from the three and five device WEC-arrays tell us the model does best in higher period waves. The shadow signal was much bigger in the larger arrays, 5-WEC arrays having the strongest signal; the results from 5-WEC arrays were the most trusted. In the 5-WEC array comparison, we saw that at most wave periods the model resolves power deficits reasonably well, but in several of the shorter wave periods (1.0-1.2 seconds) much larger power deficits were measured in the wave data. This was not surprising; as we saw in the RCW/RIW comparison the effective width measured in the wave data was much larger than predicted than the RCW curve (mechanical absorption) at the same regular wave periods (1.0-1.2 seconds). At these wave periods there must be physical processes present other than absorption which help to create the wave shadow.

The same wave period dependent behavior that occurs in the regular wave model-to-data comparison can help to explain the real seas simulations results. Looking at 5-WEC results, in the real seas states where the peak wave period is high (Oregon4, Oregon5) SWAN did an good job of predicting wave shadow. At sea states with shorter peak periods, the model did not do as well. This is because more energy in the spectrum is located at higher frequencies, where other physics than absorption induce a wave shadow. Recall Figure 21 on page 47 where RIW and RCW were plotted as a function of peak frequency; in the sea states with lower frequencies (high periods) the difference between RCW and RIW was very small, while at higher peak frequencies the RIW was greater (i.e., absorption did not fully predict shadow). The model exhibited the same tendencies since it was based on a parameterization of RCW behavior.

Because of this the model was built off the RCW curve behavior in both regular waves and real seas, we can approximate model results by the RCW curve. To examine how much some processes other than absorption affect the wave shadow we look at RIW results from the empirical data set, and the RCW curves. As a refresher, Relative Influence Width (RIW) is a proxy for shadow magnitude, and is calculated by the ratio of the relative power available (RPA) to measured power loss, where RPA is the incident energy flux multiplied by the nominal width of a WEC, and by the number of WECs in the water.

$$RPA = .55 * Ef * \#WECs \tag{23}$$

$$RIW = \frac{P_{deficit}[watts]}{RPA[watts]} \tag{24}$$

Sub-figure A of Figure 38 on page 79 recalls data analysis from Part 1, and plots average RIW and RCW and a function of period for regular wave and real seas. If the shadow were completely due to absorption, the RIW lines would plot directly on top of the RCW lines. It is clear in the top panel that other processes than absorption were present at periods of 1.0 seconds to 1.4 seconds since the RIW curve is higher than the RCW curve. In real seas

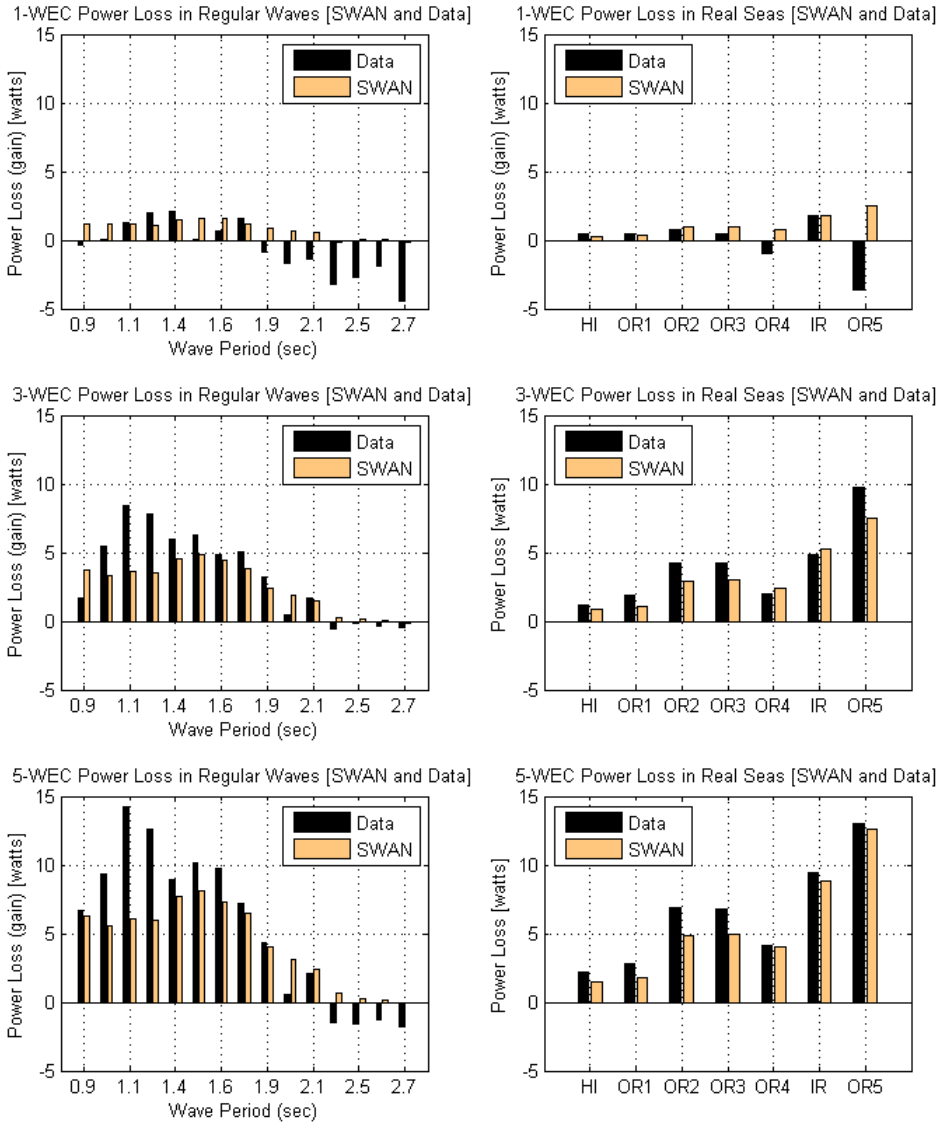

Figure 37: Comparison of model results (copper color) to empirical data (black) in regular waves, in the seven real seas sea states, for three WEC-array sizes. The mode of comparison is power lost from the wave field between upwave and downwave transects of the WEC-array.

the greatest difference between RIW and RCW curves occurs at these frequencies as well.

To approximate the portion of the shadow that is not accounted for by absorption, the ratio of RIW to RCW was taken. Ratio values above 1.0 indicate more shadowing occurs than predicted by absorption, and under 1.0 the opposite. Sub-figure B of Figure 38 on the next page plots this ratio as function of wave period for one, three and five device arrays. Results from single device arrays (blue) are of little use, since the wave shadow signal is so low and this plot is taking the ratio of two ratios which amplifies errors. Take note that the y-axis of this figure is the ratio of two ratios, so even in higher signals the results are vert susceptible to noise. The three and five device RIW curves show that at wave periods between 1.0sec and 1.4sec some other effects must be contributing to the shadow. In the rest of the domain, however, the RIW and RCW curves show that absorption is the primary driver of the shadow. This is why the model did better in sea states that have higher peak wave periods, absorption is responsible for nearly all the shadowing and the model only accounts for absorption.

6.2 Comparison to Mechanical Power Captured

In the SWAN simulations the WECs were parametrized using data that described the mechanical power absorption behavior of a single device over a range of wave periods. Because of this, the power deficit result trends (RIW) from SWAN simulations for single device arrays should be very similar to that of the power deficit trends in mechanical power absorbed (RCW) by a single WEC. We tested this by comparing the incident wave power in SWAN to the incident wave power data that was used to calculate the mechanical RCW. Sub-figure A of Figure 39 on page 80 confirmed the incident power was the same. This validated that a comparison between mechanical RCW and the RIW in SWAN is sufficient to test mechanical power against SWAN, the results of which are shown in sub-figure B of Figure 39 on page 80. Three data sets are plotted, the reference RCW from mechanical power absorption in black, RIW calculated in SWAN as the red circles, and the RIW calculated in the external spectra modification, “RIWnest” in blue. Two curves, RCW and RIWnest are nearly identical since RIWnest is simply the RCW interpolated to SWAN frequencies. The red circles vary from the RCW curve to some degree, but the overall shape and magnitudes are similar. RIW values from SWAN results should vary slightly from RCW curve values because the RIW was calculated approximately eight WEC diameters in the lee of the device, unlike the RCW which was by definition calculated at the device. Overall, this comparison to mechanical power validates the SWAN model methods.

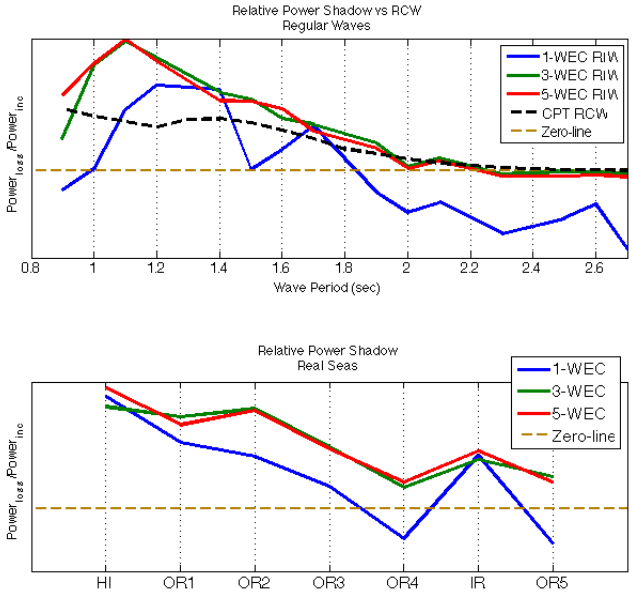

(a) Relative influence widths (RIW) measured from wave data for multiple array sizes (blue, green, red), and relative capture widths (RCW) of regular wave and real seas conditions (black). Real seas values are the mean of the seven sea states in unidirectional seas.

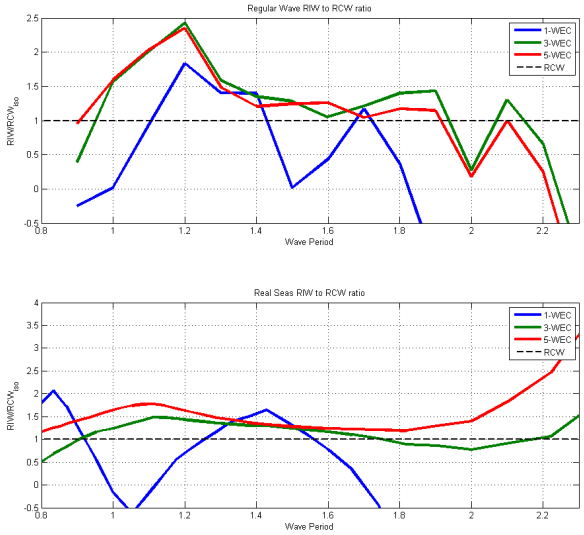

(b) Ratio of RIW to RCW as a function of wave period for regular waves and real seas. RIW values above 1.0 indicate more shadowing in wave data than predicted by WEC absorption trends (RCW).

Figure 38: These figures compare pure WEC absorption trends (RCW) used to parametrize WECs in the SWAN model to shadow magnitude trends of the empirical data set.

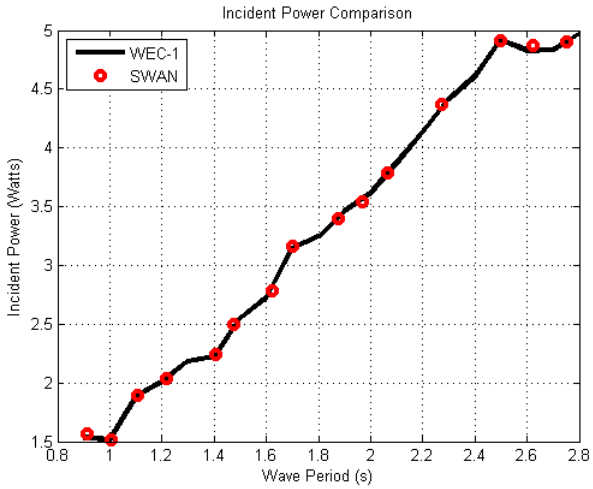

(a) Incident Power in SWAN and in Mechanical RCW. Red dots correspond to power measured in SWAN, and the black line is incident wave power measured in the wave data.

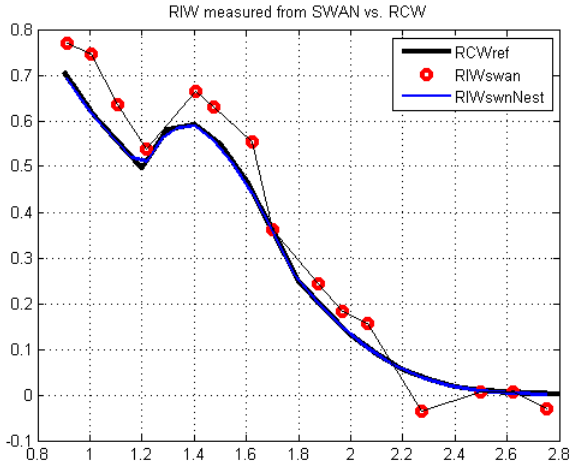

(b) Relative influence width measured in SWAN results (red dots), RCW of device (black line), and RIW measured in external spectral modification.

Figure 39: Relative influence and capture widths measured from SWAN results, mechanical data, and external spectra transformation

7 Numerical Model Conclusions

In conjunction with the spectral model, "SWAN", the parametrization and modeling WECs solely as point absorbing power sinks does a fair job of accurately predicting the power of the wave field in the lee of wave energy converter array. In regular waves it does well at higher periods, but misses some shadow magnitude at shorter wave periods. In the shorter period waves there must have been physical processes present which the current model methodology does not account for; therefore there some of the power deficit is not resolved. In high period waves a greater portion of the resultant wave shadow in the empirical data set was due purely to absorption, so the model did a better job of predicting the wave field in the downwave side of the array in these conditions. The same phenomenon was observed in real seas simulations, where wave shadows from sea states with higher peak period waves were better resolved than shorter peak period waves (as in Oregon5 v. Hawaii). In sea states where a large portion of the spectral energy is located at frequencies where shadowing driven nearly completely by WEC power absorption this modeling method will do well.

8 WAMIT/SWAN WEC Model Comparison

The modeling programs SWAN and WAMIT model the waves in entirely different manners and usually serve different purposes. SWAN is generally applied to large coarse domains and varying bathymetry with the intent of short computation times, and WAMIT generally to small dense flat domains with longer computation times. Computation time of WAMIT goes up as the number of WECs squared, while SWAN computation time is only a function of domain size and computational grid resolution. It is of great interest whether SWAN can produce similar results to WAMIT for WEC-arrays because of the great gap in computation time for modeling WEC arrays and the ability of WAMIT to model the near-field. This portion of analysis compared modeling results from SWAN to modeling results from WAMIT, in order to better gage the abilities and limitations of SWAN to resolve the effects of a WEC. The extent and magnitude of wave shadows were compared in this analysis.

The effects of WECs are resolved differently in WAMIT and SWAN. WECs in SWAN were parametrized entirely as power absorbing devices and did not account for wave scattering (spatial re-distribution of wave energy) due to the presence of an object, say as like a pile will affect the wave field. Additionally, the movement of the WEC in the water causes radiated waves, which SWAN does not resolve. WAMIT however, was able to resolve these effects, so the comparison between the two models helped us to understand in which cases parameterizing WEC as power absorbers is a fair representation of the effects from the array.

Identical wave fields were fed into SWAN and WAMIT, with idealized identical WECs, and the wave fields produced in each model were compared in longshore and cross-shore transects. SWAN was ran with and without diffraction "on", which required coarse computational grid spacing. WAMIT was fed parametric incident wave spectra exported from SWAN to ensure true apples-to-apples comparison. The WAMIT simulations come from the concurrent thesis work of McNatt [McNatt, 2012b]. Single WEC conditions were considered, and the WECs were longshore centered in a flat-bottom numerical domain.

8.1 Model Physics

SWAN and WAMIT differ in their ability to capture certain physics. WAMIT is a radiation/diffraction program developed for the linear analysis of the interaction of surface waves with various types of floating and submerged structures [WAMIT]. It has the capability to then model wave-wave interference since it is not phase-averaged like SWAN. The computation times of modeling WEC arrays for WAMIT and SWAN vary greatly

WAMIT is based on the linear and second-order potential theory for analyzing floating or submerged bodies, in the presence of ocean waves. The boundary integral equation method (BIEM), also known as the panel method, is used to solve for the velocity potential and fluid pressure on the submerged surfaces of the bodies. Separate solutions are carried out

simultaneously for the diffraction problem, giving the effects of incident waves on the body, and the radiation problems for each of the prescribed modes of motion of the bodies. These solutions are then used to obtain the relevant hydrodynamic parameters including added-mass and damping coefficients, exciting forces, response-amplitude operators (RAO's), the pressure and fluid velocity, and the mean drift forces and moments [WAMIT]

SWAN physics were described in detail in section 5.1, but the purpose of this comparison is to see whether or not SWAN physics can reasonably predict the same shadow WAMIT does. For large domains SWAN modeling is required rather than WAMIT, since WAMIT cannot model such large domains (such as the entire nearshore). It would also be computationally unfeasible to model very large arrays (50+) WECs since BEM computation time increases with the square of the number of WECs being modeled.

This portion of analysis enables diffraction in SWAN, unlike the model results shown earlier in this thesis (Section 6). Diffraction in SWAN is approximated based on the mild-slope equation for refraction-diffraction of individual waveforms, but without using any phase information. The mild-slope equation approximates linear waves propagating over a mild-sloping bottom as

$$\nabla \bullet cc_g \nabla\zeta + \kappa^2 cc_g \zeta = 0 \tag{25}$$

where c is wave velocity (celerity), $c_g$is group velocity, $\zeta = a\exp(i\psi)$ is the complex wave function and κ is determined by $\omega^2 = gk\tanh(\kappa d)$. Adding diffraction to the spectral energy balance involved only modifying the group velocity and the temporal rate of turning (in equation 8) [Holthuijsen et al., 2003].

8.2 Comparison Methods

8.2.1 Wave Conditions

This analysis tested two regular wave cases and two parametrized real seas cases. Trial conditions were limited by the ratio between computational grid size resolution and wavelength. SWAN can only converge on a solution if the wave length to grid size resolution is near $1/10 - 1/5$ the wavelength, any larger ratio and SWAN will not converge. After balancing the need for fine grid resolution and wave periods the following conditions were tested, and are listed in table 8, the trials center around periods of 1.0 and 2.0 seconds. The analysis was done at the same model scale as the WEC-array Experiments, one to thirty three length scale. At field scale wave periods of 1.0 and 2.0 seconds scale to 5.7 seconds and 11.5 seconds, respectively. Diffraction was turned on for the cases in which SWAN would converge at the current mesh size; regular waves with a period of two seconds did not converge, so diffraction for this case is not provided herein. Wave heights in this analysis are normalized by the incident wave height. Since WAMIT operates assuming linearity in wave

Table 8: Incident wave conditions for SWAN/WAMIT comparisons

Regular Waves	
T	Diffraction
[sec]	[on/off]
1.0	On, Off
2.0	Off

(a) Regular Waves

Real Seas		
T_P	s[1]	Diffraction
[sec]	[s]	[on/off]
1.0	4, 10, UD[2]	On, Off
2.0	4, 10, UD	On, Off
[1]Directional spread parameter, s, for distribution $[0.5\cos(\theta - \theta_{mean})]^{2s}$		
[2]Unidirectional		

(b) Real Seas

heights, and there was linearity with height behavior in the data, a range of wave heights was not considered for this analysis.

8.2.2 WEC performance

In this case, the relative capture width (RCW) curve was calculated by McNatt [2012b] in WAMIT for an idealized WEC that was represented by a smooth cylinder as seen in Figure 40, which extracts power only in surge. The WEC was designed to have an RCW similar to that of the "Manta 3.1" WEC built and developed by Columbia Power Technologies, which was in use during the WEC-array Experiments. The WEC RCW curve was determined by the physical characteristics and damping of such WEC. This RCW curve was used to modify the wave field by the method outlined in section 5.2.6, and is plotted in Figure 41. The RCW values at 1.0 and 2.0 seconds are both approximately 0.3.

Unlike the previous comparison of SWAN results to experimental wave data, this analysis uses a single RCW curve for real seas, and for regular waves. This is because WAMIT operates on the assumption of linearity, and the regular wave cases in a sense build the real seas cases by the superposition of waves from all frequencies within a spectra.

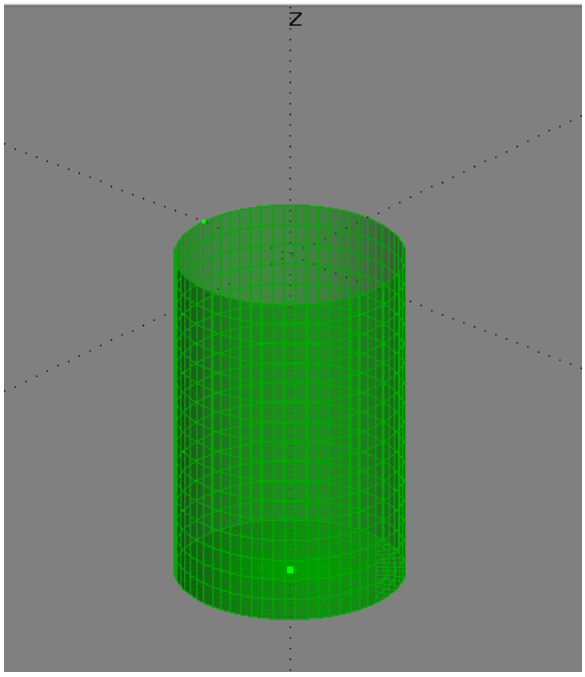

Figure 40: Idealized WEC (0.6m diameter, 0.8m draft) used to compute RCW

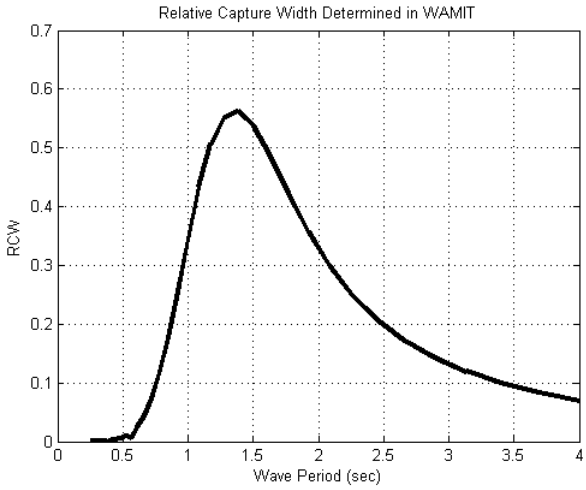

Figure 41: Relative capture width (RCW) as function of wave period for WAMIT/SWAN model comparison

9 WAMIT/SWAN Results

This section examines the model results of SWAN and WAMIT for identical incident wave conditions and idealized WEC performance for regular waves and real seas conditions. The shape and magnitude of the wave shadow of regular wave and real seas cases, and transects of wave heights in the longshore and the cross-shore directions. Unlike previous analysis in this thesis directional spreading cases results were also considered. Diffraction in SWAN is included in both unidirectional and directional seas, but one may notice that in the diffraction cases there are larger edge effects; however, materially the edge effects do not change the results.

A major difference you will notice are the differences in the offshore wave field between SWAN and WAMIT results. Since the WECs are being modeled solely as power absorbers in SWAN there is no wave reflection from the devices back to the offshore to create a standing wave pattern. Additionally, SWAN does not resolve phase, so standing waves caused by the presence of WECs are not modeled in SWAN. Standing waves created a highly variable wave field in the WAMIT results, and are best seen in the regular wave cases.

9.1 Unidirectional Waves

Wave shadow results for regular waves and unidirectional real seas simulations for WAMIT and SWAN are presented in this section. Regular wave shadow magnitudes in WAMIT results rely heavily on the incident wave period, even though the RCW value for one second and two second waves is nearly the same. WAMIT results show much more shadowing in the one second regular wave case than in the two second regular wave case. The root of this is that a significant portion of the shadow is due to scattered waves at shorter wave periods than higher wave periods. Since the RCW values are nearly the same it is not surprising that the SWAN results for one and two second waves are nearly identical, because the SWAN WEC parametrization is based sonly on RCW (absorption). Diffraction in SWAN made the shape of the shadow closer to that of WAMIT, but the shadow magnitude remained unchanged. These results can be see in Figures 42 and 47, which show wave height measured throughout the domains for SWAN in the top panel, WAMIT in the middle panel and the difference between the two models in the bottom panel. The wave shadow is shown by relative wave height reduction indicated by blue colors, and the red colors indicate increased wave heights. As mentioned previously, the WAMIT results show some very interesting offshore patterns, as well as patterns to the sides of the WEC array. These standing wave patterns are due to the scattered short-wave patterns caused by WEC-wave interactions with the incident wave field. For a more detailed explanation of this physical phenomenon see McNatt [2012b].

In real seas simulations the shadow magnitudes in WAMIT rely on incident peak period much more than in SWAN, this is because the wave field in SWAN is only modulated by

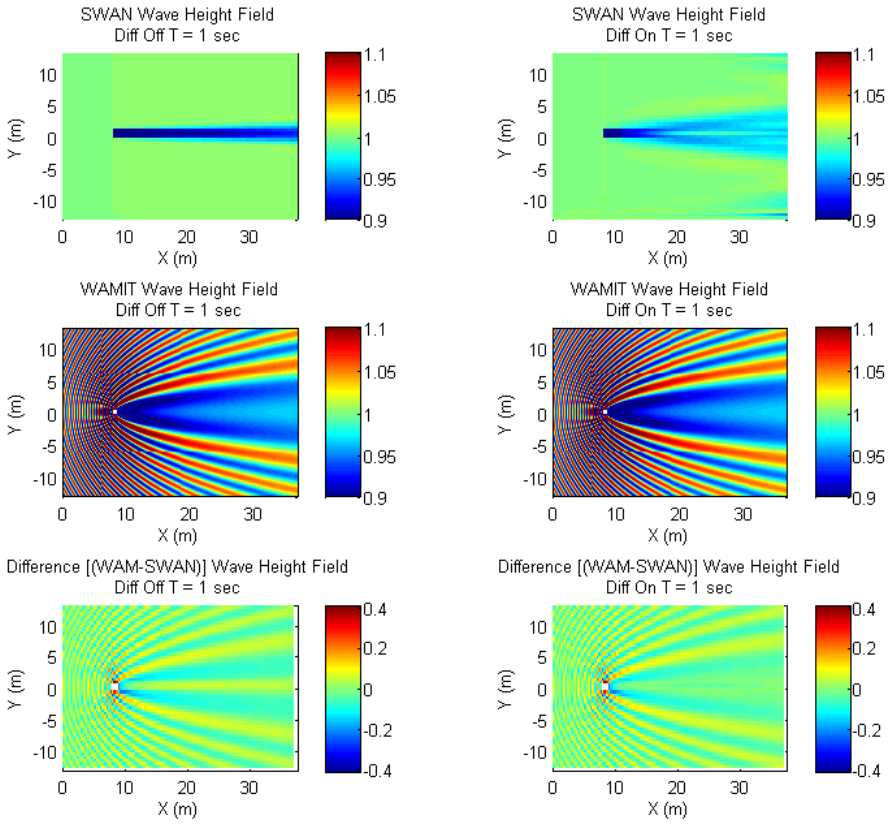

Figure 42: Regular Wave Shadowing in WAMIT and SWAN for T = 1 sec. Diffraction in SWAN is toggled on and off. Blue colors indicate shadowing, where red values indicate increased wave heights

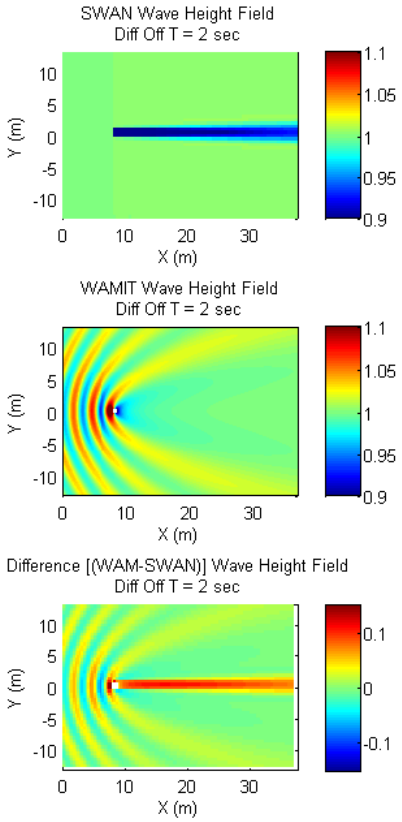

Figure 43: Regular Wave Shadowing in WAMIT and SWAN for T = 2 sec. Diffraction in SWAN is off since regular waves of two seconds would not converge. Blue colors indicate shadowing, where red values indicate increased wave height. WAMIT has very little shadowing in this case, but large offshore standing waves.

the RCW value, and not scattering. This can be seen in figures 44 and 45. More shadowing occurred in WAMIT results in the first set of trials' (1.0 second peak period) wave fields than the 2.0 second cases. In the 1.0 second cases WAMIT and SWAN do not mirror each other well, in both diffraction on and diffraction off cases. Increasing the peak wave period to 2.0 seconds has very different results

The second set of trials (2.0 second peak period) show good mirroring between WAMIT and SWAN results. Less short-wave scattering is present in this sea state, so a larger majority of the shadow is due to power absorption by the WEC than in the first set of trials (where more scattering was present, like in the one second regular wave case). Comparisons between SWAN and WAMIT in the second set of trials not only show similar shadow magnitudes, but also, when diffraction in SWAN is toggled "ON", they have very similar shadow shapes (see Figure 45), which is very promising.

A measure of total shadowing is to take the average wave height across the longshore domain, this accounts for the standing wave patterns seen in the WAMIT results. The bottom panels in Figures 46 and 47 show the total shadowing in terms of longshore averaged wave height as a function of cross-shore position. There is much more total shadowing in the WAMIT tests in the first case than in the second, but the SWAN results are very similar. Since in the second figure the total shadow lines are very similar we observe that SWAN has done an fair job of representing the shadow in the lee of the array, with respect to WAMIT results. One can also see the standing wave patterns created in the offshore by the presence of the WEC in the WAMIT trials.

9.2 Directional Spreading

In this section, results from effect of directional spreading on the wave field for comparison between SWAN and WAMIT are presented. Generally, SWAN does better with directionally spread seas than unidirectional waves since it was designed to simulate real seas. Since it was shown in Section 9.1 that at short wave periods SWAN and WAMIT differ more than in longer wave periods (with similar RCW values) this section will only present results based on peak wave periods of 2.0 seconds.

With directional spreading on SWAN did a very good job of replicating the wave field in the lee of the WEC predicted by WAMIT with both diffraction on, and diffraction off. There was very little difference between SWAN wave fields with diffraction "on" or "off" in the directionally spread seas. Wave energy adequately was spread laterally without the inclusion of artificial diffraction in these cases. This can be see in figures 49 and 49 where the wave shadow shapes are nearly identical between diffraction on and off, as well as WAMIT results. Additionally, figures 50 and 51 show that in SWAN the cross-shore wave shadow magnitude directly in the lee of the WEC and the total wave shadow magnitude (estimated by longshore averaged wave height) are both very similar to the WAMIT results.

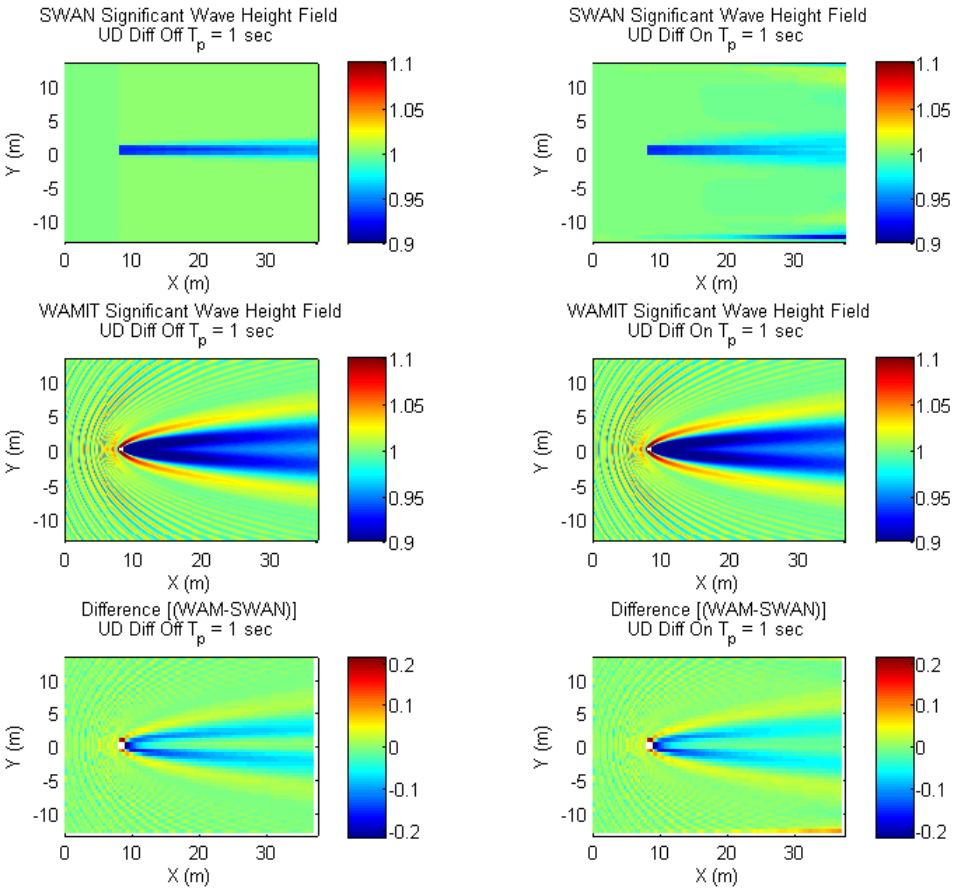

Figure 44: Wave field shadowing results from WAMIT and SWAN real seas simulations with unidirectional waves for a peak period of 1.0 seconds. Blue colors indicate relative wave reduction (shadowing), while red colors indicate increased wave heights. The bottom panel shows the difference between the two models in space

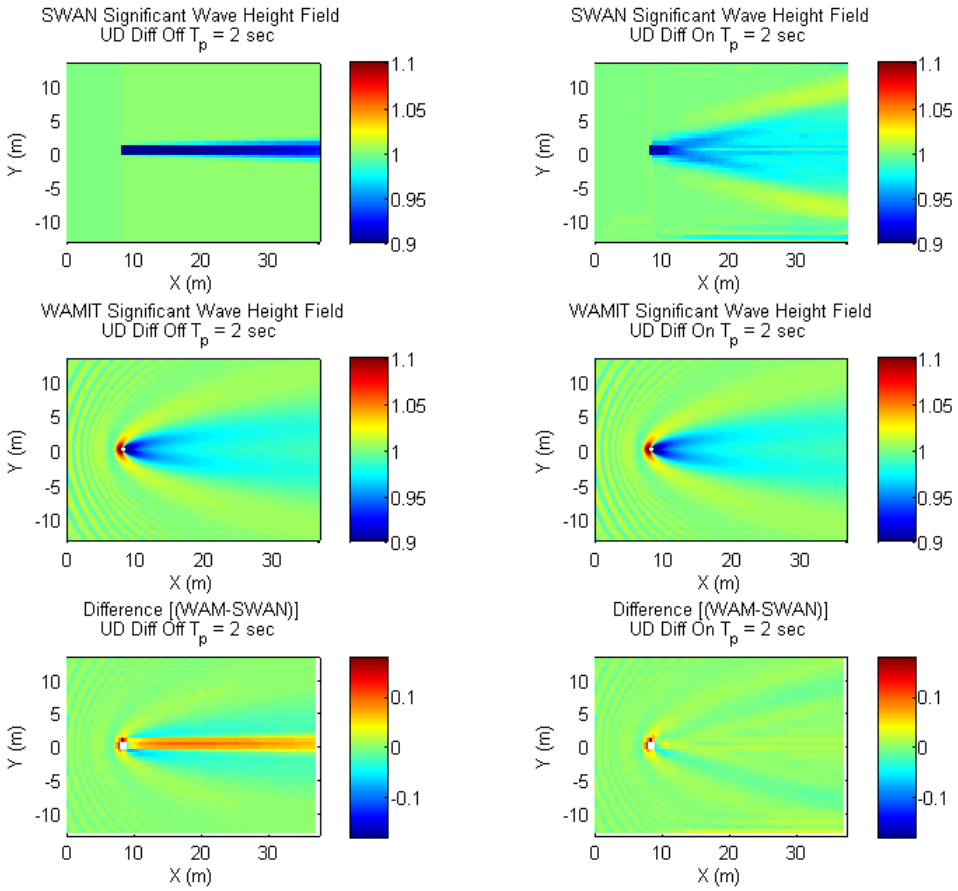

Figure 45: Wave field shadowing results from WAMIT and SWAN real seas simulations with unidirectional waves for a peak period of 2.0 seconds. Blue colors indicate relative wave reduction (shadowing), while red colors indicate increased wave heights. The bottom panel shows the difference between the two models in space

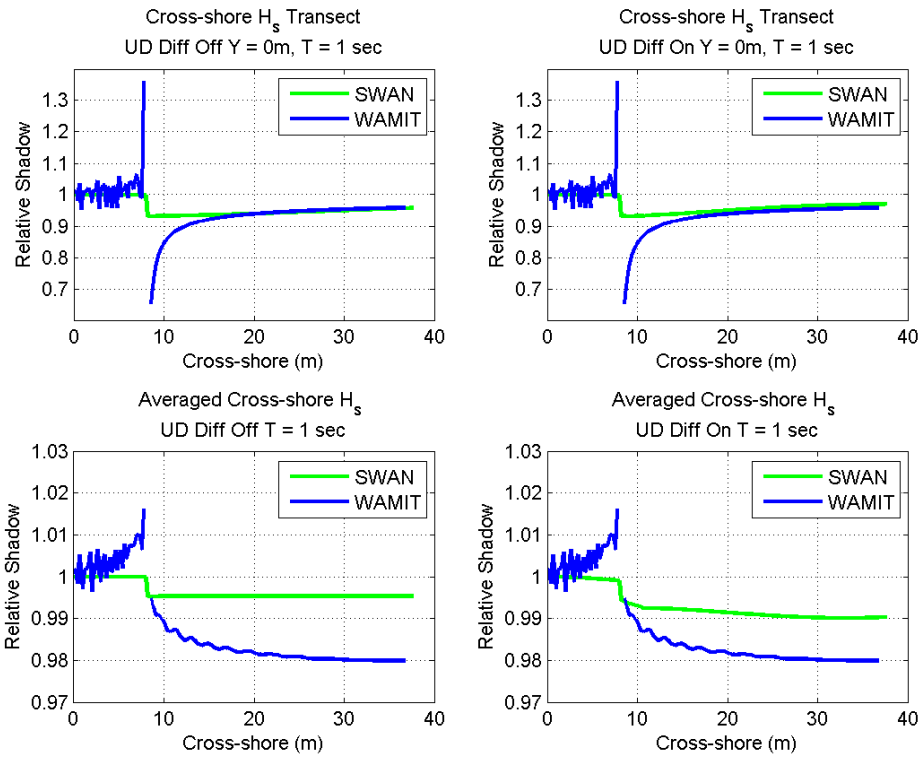

Figure 46: Cross-shore relative shadow transects of real seas simulations with unidirectional waves for a peak period of 1.0 seconds. The transects are measured at the longshore location of the WEC, and as the average wave height across the longshore domain.

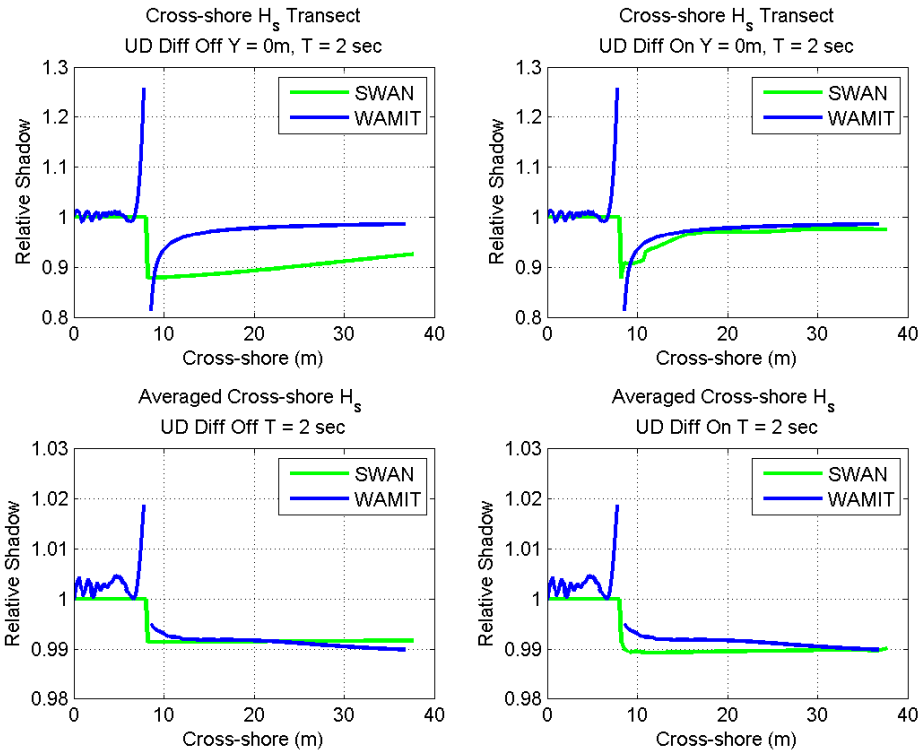

Figure 47: Cross-shore relative shadow transects of real seas simulations with unidirectional waves for a peak period of 2.0 seconds. The transects are measured at the longshore location of the WEC, and as the average wave height across the longshore domain.

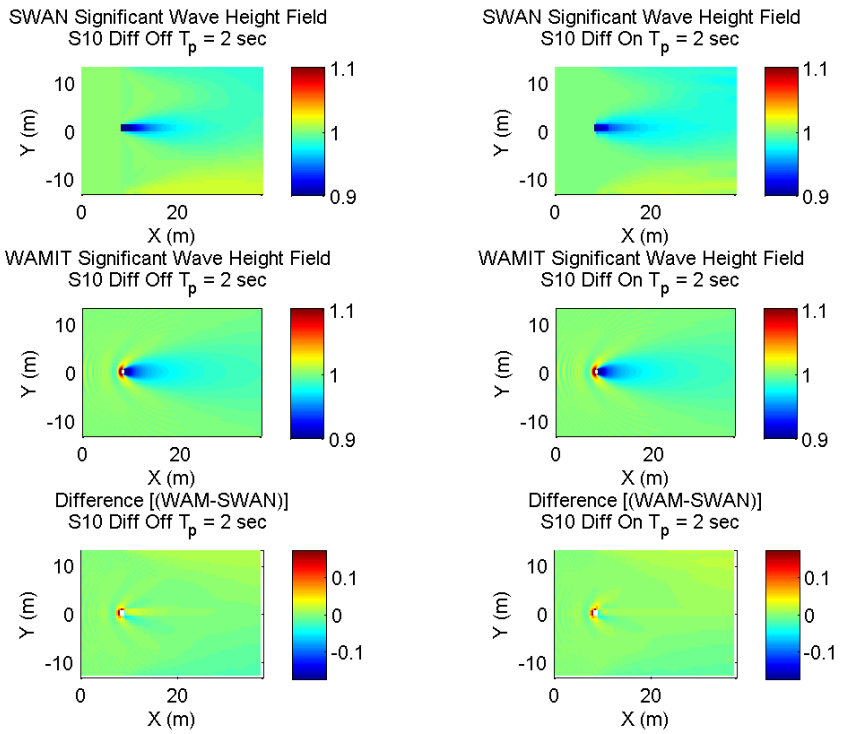

Figure 48: Wave field shadowing results from real seas simulations with a directional spreading factor of s = 10 with a peak period of 2.0 seconds. Blue colors indicate relative wave reduction (shadowing), while red colors indicate increased wave heights. The bottom panel shows the difference between the two models in space

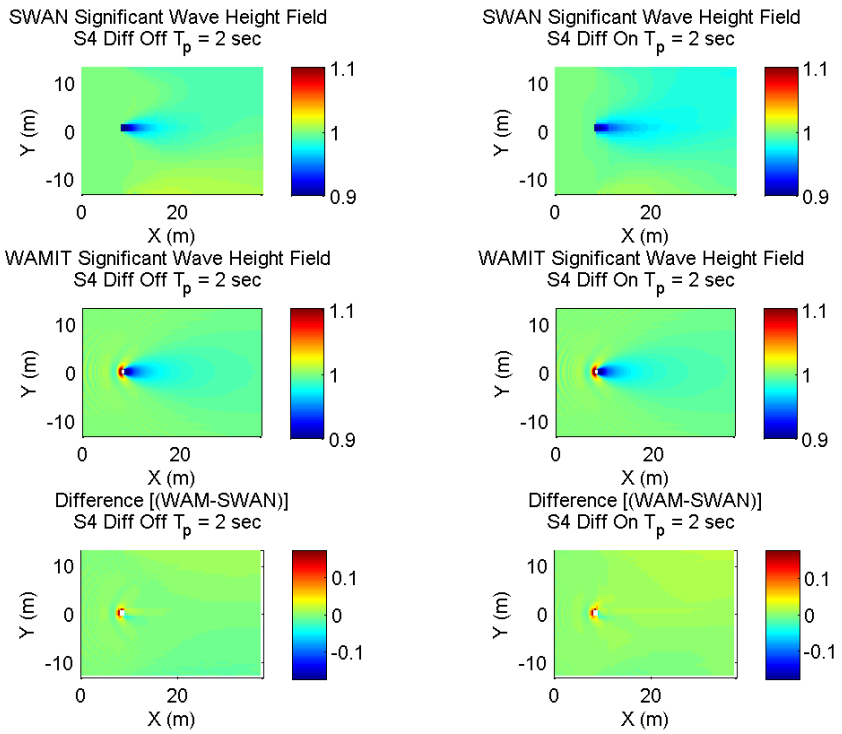

Figure 49: Wave field shadowing results from real seas simulations with a directional spreading factor of s = 4 with a peak period of 2.0 second. Blue colors indicate relative wave reduction (shadowing), while red colors indicate increased wave heights. The bottom panel shows the difference between the two models in space

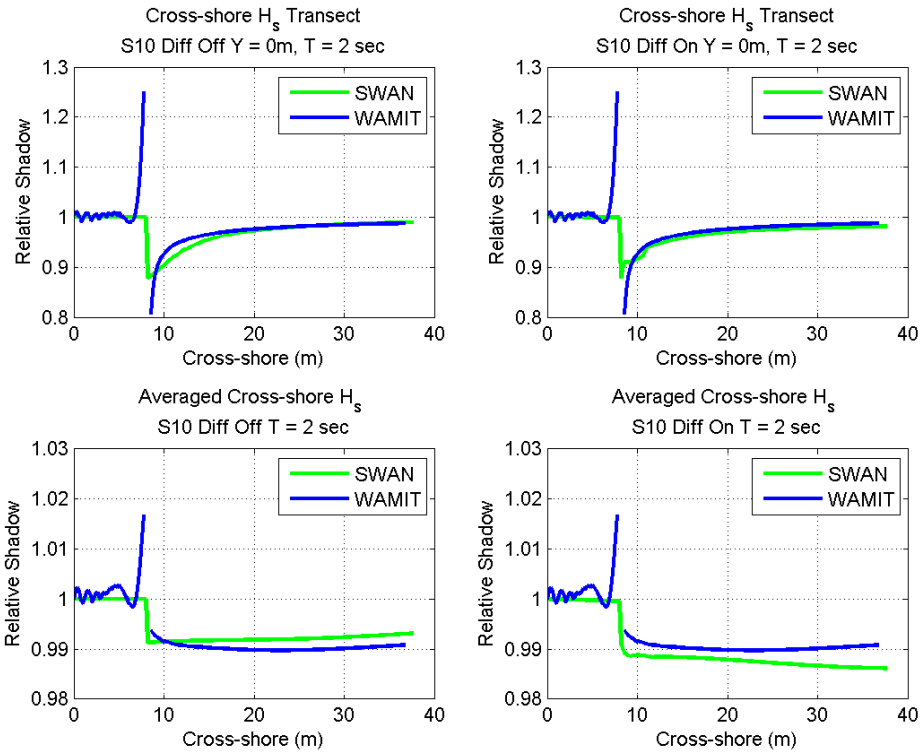

Figure 50: Cross-shore transect results from real seas simulations with a directional spreading factor of s = 10 with a peak period of 2.0 seconds. SWAN and WAMIT results are very similar.

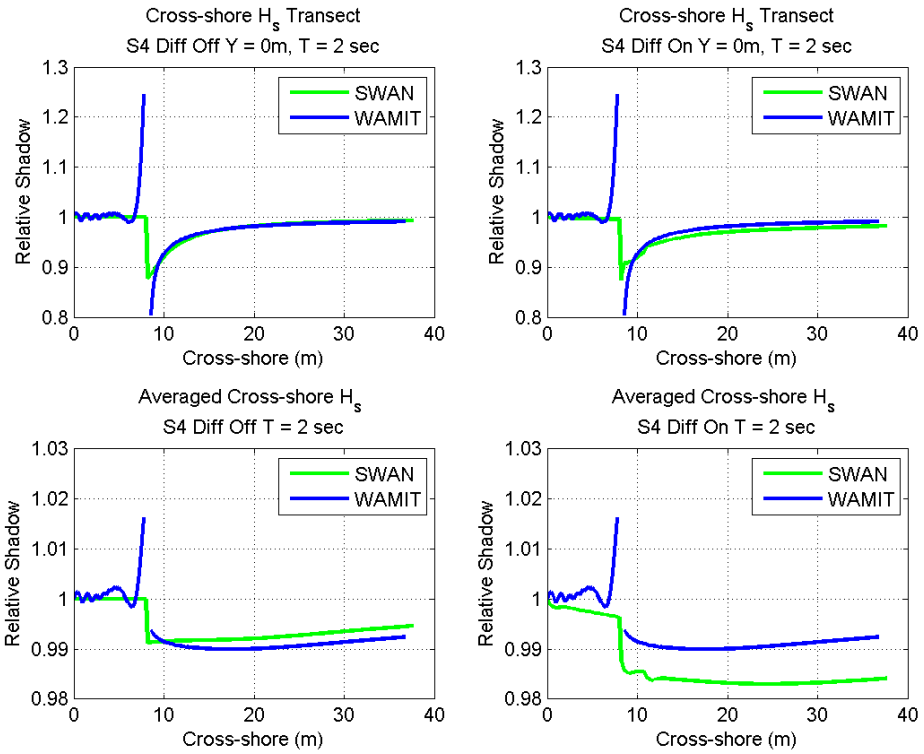

Figure 51: Wave field shadowing results from real seas simulations with a directional spreading factor of s = 4 with a peak period of 2.0 seconds. SWAN and WAMIT results are very similar.

10 WAMIT/SWAN Conclusions

The WAMIT to SWAN comparison proved very useful in taking a look at the physics SWAN can and cannot capture, and helps to understand exactly what is going on in the model to observational data comparisons. At very short wave periods the WEC shadow is greatly influenced by patterns created by scattered waves from hydrodynamic interaction in the array, as well as shadowing due to WEC absorption. SWAN is not able to resolve the scattered short-waves, such as $T_p = 1sec$ waves; it does not perform as well in this regime as compared to higher wave periods. At the higher wave periods, such as $T_p = 2sec$, the shadow is due almost completely to absorption. We know this since the WAMIT and SWAN models match each other well and this SWAN model only models absorption.

In regular waves SWAN did not match the wave field shape of WAMIT well in any case, but SWAN is not built for regular waves so this was not surprising. Similarly, we did not expect SWAN to provide any sort of estimation of the offshore reflected wave field as seen in the WAMIT results. Reflection was not turned on in SWAN, and it cannot model standing waves due to phase differences since it is a phase-averaged model. In this portion of the thesis of interest was solely the shape and magnitude of the shadow in the *lee* of the WEC, normalized by incident conditions, which was very promising.

In unidirectional cases when diffraction was toggled on, and lateral spreading was due to this only, the shape of the SWAN shadow matched that of the WAMIT shadow well. It can be concluded that diffraction in SWAN for unidirectional seas does an good job of replicating the actual wave field for real seas simulations. In directionally spread seas when the shadow was primarily due to wave power absorption by the WEC (i.e. $T_P = 2sec$), lateral energy spreading in SWAN without the aid of artificial diffraction did a very good job of replicating the shadow in WAMIT unlike in unidirectional cases. In the field, where directional spread seas are expected, diffraction will likely not need to be included to accurately predict the wave shadow shape.

11 Discussion

The skill of the model to predict wave shadow magnitudes was dependent on wave period, but this may not be an issue for modeling full-size wave farms. Because the WEC-parameterization in the SWAN model was based on absorption (RCW), results from the model are similar to the the comparison of RCW to measured shadow magnitude. Data to model results showed the model does reasonable well in all sea states, but as was learned from the WAMIT-SWAN comparison, it performs best where frequencies containing the most energy also have minimal diffraction and radiated wave amplitudes. It is expected that WEC-arrays will be deployed in areas where the wave power resource is large, in which case the peak wave periods of the incident wave field will be relatively high since power (energy flux) is a function of group velocity, $E_F = EC_g$. Therefore the WECs will create shadows more so from higher period waves than smaller period waves, which are better modeled by absorption behavior. This was similar to the $T_P = 2sec$ case shown in the WAMIT/SWAN comparison. It is then reasonable to say that this method can be applied to future field sites with good accuracy.

The the data set has been used to validate work from two very different models, WAMIT [McNatt, 2012b] and SWAN. Observed wave used to verify these models was from unidirectional waves only, which comprise only one quarter of all real seas simulations ran. Future work from this data set should include resolving and parameterizing the directional wave spectra. Predicting the longshore structure of the shadow is a key to field application. However, the WAMIT-SWAN comparisons showed that even without directional dependence SWAN did a fair job of predicting the wave shadow for two separate directionally spread seas cases. An application of the SWAN method to field scale should give an approximate prediction of the wave expected wave shadow.

The comparison of model results to empirical data yielded good wave shadow predictions by the model, especially since it accounts for only absorption. At the longshore extent of the shadow in the lee gage array some shadowing was still evident, that is, the lee gage array did not fully resolve the shadow width. It is possible that measurements from the empirical data set did not capture the entire magnitude of the shadow. Power loss calculations could have then been under-estimated in the empirical data set, which is why power losses from the model which are based solely on absorption are so close to empirical results. The additional power losses in the empirical data however, are likely small, and do not alter the conclusions of this report. Materially, the results and conclusions presented within this report are not affected by this, but it was worth noting.

12 Conclusions

This thesis showed that the parametrization of WEC-array effects based on WEC power capture behavior does a fair job of predicting the shadow in the lee of a WEC-array, and does a better job as wave period and directional spreading increases. Experimental results showed us that the wave shadows created by WEC-arrays were frequency dependent. Power deficits in the lee were predicted with fair accuracy by the frequency dependent WEC power absorption proxy, Relative Capture Width. This allowed us to conclude that the shadows were primarily a function of absorption by the WECs. Shadow magnitudes were well predicted in the higher wave period regimes, but under-predicted in small wave periods. Wave data showed that in regular waves with a period of 1.0-1.4 seconds the under-prediction of the magnitude was on the order of twofold. Results from the WAMIT-SWAN comparison showed us that the difference between the predicted shadow and measured shadow was due to scattered short waves caused by additional hydrodynamic interactions of the WEC with the incident wave field. At wave periods higher than this (1.5 sec +), the wave shadow magnitude was predicted by absorption (RCW) fairly well in both regular waves and the real seas frequency spectra. Scaling shadow magnitude between array sizes was shown to be moderately linear. An investigation into the ability of the spectral model SWAN to predict WEC-effects on the wave-field against a phase-resolving model, WAMIT, proved extremely useful in determining scattered waves as the sources of difference between SWAN and observations. The extensive observational data set validated not only the SWAN model, but the WAMIT model as well [McNatt, 2012b]. It provided us with great insight for investigating effects of WEC arrays on the wave-field, and the subsequent modeling. Verification at lab scale of modeling WECs based on device absorption behavior is very promising for expecting reasonable predictions at field scale.

Modeling of the WEC-Array Experiments was done with SWAN for normally incident unidirectional real seas conditions and regular waves. Only unidirectional waves were considered because relative wave reductions (wave shadow) magnitude was often characterized by the power deficit between in the incident wave field and the lee gage array, and only waves with normally incident energy flux could currently be resolved. Incident wave conditions were difficult to ascertain due to WEC-array influence on the offshore gage array. The incident wave field for data analysis and model input of all array sizes was best described by the measured incident wave conditions for like trials of the single-WEC array since offshore wave heights in these cases were the least affected (smallest).

SWAN does good job of predicting the wave shadow with WEC-array parametrization based on device absorption behavior from a single device. This modeling method was shown to predict the wave shadow in real seas more consistently than in regular waves. However, in both regular waves and real seas the shadow was predicted better in higher period sea states because short wave scattering is minimal. More scattering occurs at the shorter wave

periods because the wavelength to device size ratio is maximized. Our parameterization-by-absorption method does not account for shadowing due to scattering, so the power deficit of the shadow in the model results is sometimes underestimated. As shown in the WAMIT-SWAN comparison, at very short wave periods wave scattering can be significant. This was also evident in model-data comparisons where the power deficit was under-predicted by two-fold in small period (1.0-1.4 sec) regular waves. Larger period waves have longer wavelengths, so less scattering due to the presence of the WEC occurs. In sea states where a large portion of energy is located at frequencies whose wavelength are much longer than the characteristic device length, this modeling method should do a good job of predicting the wave shadow in the lee of a WEC-array.

In addition to the the WEC-array experiments and associated modeling, the WAMIT-SWAN model comparison showed us that with diffraction on, or in directionally spread seas, SWAN is able to make good predictions of the magnitude and shape of the wave shadow in the lee of a single device, except at small wave periods. In directionally spread seas, having diffraction "on" or "off" did not make an observable difference in results. The short wave periods tested showed that SWAN underestimates the wave shadow because of increased scattered short waves. Because of these findings the WAMIT-SWAN comparison gave great insight into what roles the different wave field physics play in wave shadows, and improved our understanding of the empirical data set.

Bibliography

Alexandre, A., Stallard, T. & Stansby, P. (2009) Transformation of wave spectra across a line of wave devices. In: Proceedings of the 8th European Wave and Tidal Energy Conference. Uppsala, Sweden.

Ashton, I., Johanning, L. & Linfoot, B. (1999) Measurement of the effect of power absorption in the lee of a wave energy converter. ASME pp. 1021–1030.

Baldock, T. & Simmonds, D. (1999) Seperation of incident and reflected waves over sloping bathymetry. Coastal Engineering 38(3):167–176.

Beels, C., Troch, P., De Visch, K., Kofoed, J. & De Backer, G. (2010) Application of the time-dependent mild-slope equations for the simulation of wave effects in the lee of a farm of wave dragon wave energy converters. Renewable Energy (35):1644–1661.

Booij, N., Ris, R. C. & Holthuijsen, L. H. (1999) A third generation wave model for coastal regions 1. model description and validation. Journal of Geophysical Research 104(C4):7649–7666.

Borgarino, B., Babarit, A. & Ferrant, P. (2012) Impact of long separating distances on the energy production of two interacting wave energy converters. Ocean Engineering 41:79–88.

Boyle, L., Elsaesser, B. & Folley, M., W. T. (2011) Assesment of wave basin homogenuity for wave energy converter array studies. In: Proceedings of the 9th European Wave and Tidal Energy Conference, Southamption, UK.

Budal, K. (1977) Theory for absorption of wave power by a system of interacting bodies. Journal of Ship Research 21(4):248–253.

Cooley, J. & Tukey, J. (1965) An algorithm for the machine calculation of complex fourier series. Mathematics of Computation 19:297–301.

Cruz, J., Skykes, R., Siddorn, P. & Taylor, R. (September 2009) Wave farm design: Preliminary studies on the influence of wave climate, array layout and farm control. In: Proceedings of the 8th European Wave and Tidal Energy Conference, Uppsala, Sweeden.

Dean, R. G. & Dalrymple, R. (1998) Water Wave Mechanics for Engineers & Scientists (Advanced Series on Ocean Engineering-Vol2).

Elgar, S., Herbers, T. H. C. & Guza, R. T. (1994) Reflection of ocean surface gravity waves from a natural beach. Journal of Physical Oceanography 24:1503–1511.

Farley, F. J. M. (2011) Far-field theory of wave power capture by oscillating systems. Philosophical Transactions of the Royal Society A: Mathematical, Physical and Engineering Sciences 370(1959):278–287.

Folley, M. & Whittaker, T. (2011) The adequacy of phase-averaged wave models for modelling wave farms. In: Proc. Of the ASME 2011 30th International Conference on Ocean, Offshore and Arctic Engineering.

Folley, M., Babarit, A., Child, B., Forehand, D., O'Boyle, L., Silverthorne, K., Spinneken, J., Stratigaki, V. & Troch, P. (2012) A review of numerical modelling of wave energy converter arrays. In: Proc. Of the ASME 2012 31th International Conference on Ocean, Offshore and Arctic Engineering.

Goring, G. & Nikora, V. (2002) Despiking acoustic doppler velocimiters. Journal of Hydraulic Engineering 128:117–126.

Haller, M., Porter, A., Lenee-Bluhm, P., Rhinefrank, K., Hammagren, E., Ozkan-Haller, H. T. & Newborn, D. (2011) Laboratory observations of waves in the vicinity of WEC-arrays. In: Proceedings of the 9th European Wave and Tidal Energy Conference, Southamption, UK.

Harris, F. J. (1978) On the use of windoes for harmonic analysis with the discrete fourier transform. In: Proceedings of the IEEE 66. pp. 51–83.

Holthuijsen, L., Herman, A. & Booij, N. (2003) Phase-decoupled refraction–diffraction for spectral wave models. Coastal Engineering 49(4):291–305.

Komar, P. D. (1998) Beach Processes and Sedimentation. Prentince Hall.

Lenee-Bluhm, P. (2012) Personal correspondance. E-mail.

McIver, P. (1994) Some hydrodynamic aspects of arrays of wave-energy devices. Applied Ocean Research 16:61–69.

McNatt, C. (2012a) Personal correspondance. E-mail.

McNatt, C. (2012b) Wave field patterns generated by wave energy converters. Master's thesis, Oregon State University.

Millar, D., Smith, H. & Reeve, D. (2007) Modelling analysis of the sensitivity of shoreline change to a wave farm. Ocean Engineering 34(5-6):884–901.

Monk, K., Zou, Q. & Conley, D. (2011) Numerical and analytical simulations of waver interference about a single row array of wave energy converters. Coastal Engineering .

Mori, N., Suzuki, T. & Kakuno, S. (2007) Noise of acoustic doopler velocimeter data in bubbly flow. Journal of Engineering Mechanics, American Society of Civil Engineers .

Ricci, P., Saulnier, J. B. & de O. Falcão, A. F. (2007) Point-absorber arrays: configuration study off the potuguese west coast. In: Proceedings of the 7th European Wave and Tidal Energy Conference, Porto, Portugal.

Silverthorne, K. E. & Folley, M. (2011) A new numerical representation of wave energy converters in a spectral wave model. In: Proceedings of the 9th European Wave and Tidal Energy Conference. Southhampton, UK.

Smith, H., Pearce, C. & Millar, D. (2012) Further analysis of change in nearshore wave climate due to an offshore wave farm: An enhanced case study for the proposed wave hub site. Renewable Energy 40:51–64.

Sorensen, R. (2006) Basic Coastal Engineering. Springer.

SWANTeam (2011) SWAN Users Manual. http://www.swan.tudelft.nl.

The SWAN Team (2011) SWAN Technical Manual. http://www.swan.tudelft.nl.

Troch, P., Beels, C., De Rouck, J. & De Backer, G. (2010) Wake effects behind a farm of wave energy converters for irregular long-crested and short-crested waves. Coastal Engineering .

Venugopal, V. & Smith, G. (2007) Wave climate investigation for an array of wave power devices. In: Proceedings of the 7th European Wave and Tidal Energy Conference, Porto, Portugal.

WAMIT (????) Wamit user guide. Website: www.wamit.com/manual.

Weller, S., Stallard, T. & Stansby, P. (2009) Experimental measurements of irregular wave interaction factors in closely spaced arrays. In: Proceedings of 8th European Wave and Tidal Energy Conference, Uppsala , Sweeden,.

APPENDIX

A. Trial Conditions

Target trial conditions for the WEC-Array Experiments are contained in this appendix. Wave conditions are organized according to array size, real or regular wave conditions, and trial purpose. Unless otherwise noted, the trials used WEC #1.

Listed in regular waves are wave period (T), wave height (H), incident angle (Theta), trial number (Trial), and test type (Test). Test type refers to whether the trial was ran in the amplitude scan tests (A) or the frequency scan tests (F).

Listed in real seas are peak period (Tp), significant wave height (Hs), sea state (SeaState), incident angle (Theta), trial number (Trial), Test type (Test), and WEC number.

1-WEC Regular Waves

T (s)	H	Theta	Trial	Test
1.0	6	0	2	A
1.0	9	0	3	A
1.2	3	0	4	A
1.2	6	0	6	A
1.2	9	0	7	A
1.4	3	0	8	A
1.4	6	0	9	A
1.4	9	0	10	A
1.4	12	0	11	A
1.4	15	0	12	A
1.6	3	0	14	A
1.6	6	0	15	A
1.6	9	0	16	A
1.8	3	0	17	A
1.8	6	0	18	A
1.8	9	0	19	A
2.0	3	0	20	A
2.0	6	0	21	A
2.0	9	0	22	A
2.0	12	0	23	A
2.0	15	0	24	A
2.2	3	0	25	A
2.2	6	0	26	A
2.2	9	0	27	A
2.4	3	0	28	A
2.4	6	0	29	A
2.4	9	0	30	A
2.6	3	0	31	A
2.6	6	0	32	A
2.6	9	0	33	A
2.6	12	0	34	A
2.6	15	0	35	A
2.8	3	0	36	A
2.8	6	0	37	A
2.8	9	0	38	A
1.0	3	0	39	A
1.0	6	0	40	A
1.0	9	0	41	A
1.2	3	0	42	A
1.2	6	0	43	A
1.2	9	0	44	A
1.4	3	0	45	A
1.4	6	0	46	A
1.4	9	0	47	A
1.4	12	0	48	A
1.4	15	0	49	A
1.6	3	0	50	A
1.6	6	0	51	A
1.6	9	0	52	A
1.8	3	0	53	A
1.8	6	0	54	A
1.8	9	0	55	A
2.0	3	0	56	A
2.0	6	0	57	A
2.0	9	0	58	A

1-WEC Regular Waves

T (s)	H	Theta	Trial	Test
2.0	12	0	59	A
2.0	15	0	60	A
2.2	3	0	61	A
2.2	6	0	62	A
2.2	9	0	63	A
2.4	3	0	64	A
2.4	6	0	65	A
2.4	9	0	66	A
2.6	3	0	67	A
2.6	6	0	68	A
2.6	9	0	69	A
2.6	12	0	70	A
2.6	15	0	71	A
2.8	3	0	72	A
2.8	6	0	74	A
2.8	9	0	75	A
0.9	6	0	2	F
1.1	6	0	3	F
1.5	6	0	5	F
1.7	6	0	6	F
1.9	6	0	7	F
2.1	6	0	9	F
2.3	6	0	10	F
2.5	6	0	11	F
2.7	6	0	12	F
0.9	6	22.5	13	F
1.1	6	22.5	14	F
1.3	6	22.5	15	F
1.5	6	22.5	16	F
1.7	6	22.5	17	F
1.9	6	22.5	18	F
2.1	6	22.5	19	F
2.3	6	22.5	20	F
2.5	6	22.5	21	F
2.7	6	22.5	22	F
1.0	6	22.5	23	F
1.2	6	22.5	24	F
1.4	6	22.5	25	F
1.6	6	22.5	26	F
1.8	6	22.5	27	F
2.0	6	22.5	28	F
2.2	6	22.5	29	F
2.4	6	22.5	30	F
2.6	6	22.5	31	F
2.8	6	22.5	32	F
0.9	6	0	33	F
1.1	6	0	34	F
1.5	6	0	36	F
1.7	6	0	37	F
1.9	6	0	38	F
2.1	6	0	39	F
2.3	6	0	40	F
2.5	6	0	41	F
2.7	6	0	42	F
0.9	6	22.5	43	F

1-WEC Regular Waves

T (s)	H	Theta	Trial	Test
1.1	6	22.5	44	F
1.3	6	22.5	45	F
1.5	6	22.5	46	F
1.7	6	22.5	47	F
1.9	6	22.5	48	F
2.1	6	22.5	49	F
2.3	6	22.5	50	F
2.5	6	22.5	51	F
2.7	6	22.5	52	F
1.0	6	22.5	53	F
1.2	6	22.5	54	F
1.4	6	22.5	55	F
1.6	6	22.5	56	F
1.8	6	22.5	57	F
2.0	6	22.5	58	F
2.2	6	22.5	59	F
2.4	6	22.5	60	F
2.6	6	22.5	61	F
2.8	6	22.5	62	F
1.0	6	0	63	F
1.0	6	0	64	F
1.2	6	0	65	F
1.4	6	0	66	F
1.6	6	0	67	F
1.8	6	0	68	F
2.0	6	0	69	F
2.2	6	0	70	F
2.4	6	0	71	F
1.0	6	0	72	F
1.2	6	0	73	F
1.4	6	0	74	F
1.6	6	0	75	F
1.8	6	0	76	F
2.0	6	0	77	F
2.2	6	0	78	F
2.4	6	0	79	F
1.2	6	0	80	F
1.0	6	0	81	F
1.4	6	0	82	F
1.6	6	0	16	A

1-WEC Real Seas

T (s)	H	SeaState	s	Theta	Trial	Test
1.22	4.54	HI	UD	22	46	Real
1.22	4.54	HI	UD	0.0	52	Real
1.22	4.54	HI	UD	22	53	Real
1.22	4.54	HI	UD	22	60	Real
1.22	4.54	HI	UD	0.0	70	Real
1.22	4.54	HI	UD	22	71	Real
1.22	4.54	HI	UD	22	72	Real
1.42	7.58	OR2	UD	0.0	7	Real
1.42	7.58	OR2	UD	22	8	Real
1.42	7.58	OR2	UD	0.0	29	Real
1.42	7.58	OR2	UD	22	30	Real
1.42	7.58	OR2	UD	22	59	Real
1.42	7.58	OR2	UD	22	63	Real
1.62	4.54	OR1	UD	0.0	4	Real
1.62	4.54	OR1	UD	22	5	Real
1.62	4.54	OR1	UD	0.0	24	Real
1.62	4.54	OR1	UD	22	25	Real
1.62	10.6	IR	UD	22	49	Real
1.62	10.6	IR	UD	0.0	50	Real
1.62	10.6	IR	UD	22	56	Real
1.62	10.6	IR	UD	0.0	57	Real
1.62	10.6	IR	UD	22	61	Real
1.62	10.6	IR	UD	22	65	Real
1.62	10.6	IR	UD	0.0	75	Real
1.62	10.6	IR	UD	22	76	Real
1.82	7.58	OR3	UD	0.0	11	Real
1.82	7.58	OR3	UD	22	12	Real
1.82	7.58	OR3	UD	0.0	33	Real
1.82	7.58	OR3	UD	22	34	Real
2.22	7.58	OR 4	UD	0.0	15	Real
2.22	7.58	OR 4	UD	22	16	Real
2.22	13.6	OR 5	UD	0.0	19	Real
2.22	13.6	OR 5	UD	22	20	Real
2.22	7.58	OR 4	UD	0.0	37	Real
2.22	7.58	OR 4	UD	22	38	Real
2.22	13.6	OR 5	UD	0.0	40	Real
2.22	13.6	OR 5	UD	22	41	Real
2.22	13.6	OR 5	UD	0.0	66	Real
2.22	13.6	OR 5	UD	22	67	Real
1.22	4.54	HI	4.0	0.0	21	Real
1.22	4.54	HI	4.0	0.0	43	Real
1.22	4.54	HI	4.0	0.0	68	Real
1.42	7.58	OR2	4.0	0.0	6	Real
1.42	7.58	OR2	4.0	0.0	27	Real

1-WEC Real Seas

T (s)	H	SeaState	s	Theta	Trial	Test
1.42	7.58	OR2	4.0	0.0	58	Real
1.42	7.58	OR2	4.0	0.0	62	Real
1.62	4.54	OR1	4.0	0.0	1	Real
1.62	4.54	OR1	4.0	0.0	22	Real
1.62	10.6	IR	4.0	0.0	47	Real
1.62	10.6	IR	4.0	0.0	54	Real
1.62	10.6	IR	4.0	0.0	64	Real
1.62	10.6	IR	4.0	0.0	73	Real
1.82	7.58	OR3	4.0	0.0	9	Real
1.82	7.58	OR3	4.0	0.0	31	Real
2.22	7.58	OR 4	4.0	0.0	13	Real
2.22	13.6	OR 5	4.0	0.0	17	Real
2.22	7.58	OR 4	4.0	0.0	35	Real
2.22	13.6	OR 5	4.0	0.0	39	Real
1.22	4.54	HI	10.0	0.0	44	Real
1.22	4.54	HI	10.0	0.0	51	Real
1.22	4.54	HI	10.0	0.0	69	Real
1.42	7.58	OR2	10.0	0.0	2	Real
1.42	7.58	OR2	10.0	0.0	28	Real
1.62	4.54	OR1	10.0	0.0	3	Real
1.62	4.54	OR1	10.0	0.0	23	Real
1.62	10.6	IR	10.0	0.0	48	Real
1.62	10.6	IR	10.0	0.0	55	Real
1.62	10.6	IR	10.0	0.0	74	Real
1.82	7.58	OR3	10.0	0.0	10	Real
1.82	7.58	OR3	10.0	0.0	32	Real
2.22	7.58	OR 4	10.0	0.0	14	Real
2.22	13.6	OR 5	10.0	0.0	18	Real
2.22	7.58	OR 4	10.0	0.0	36	Real
1.22	4.54	HI	UD	0.0	45	Real

3-WEC Regular Waves

T (s)	H	Theta	Trial	Test
1.0	6	0	1	A
1.0	9	0	2	A
1.2	6	0	3	A
1.2	9	0	4	A
1.2	12	0	5	A
1.3	6	0	6	A
1.3	9	0	7	A
1.3	12	0	8	A
1.3	15	0	9	A
1.4	6	0	10	A
1.4	9	0	11	A
1.4	12	0	12	A
1.4	15	0	13	A
1.6	6	0	14	A
1.6	9	0	15	A
1.6	12	0	16	A
1.6	15	0	17	A
2.0	6	0	18	A
2.0	9	0	19	A
2.0	12	0	20	A
2.0	15	0	21	A
2.6	6	0	22	A
2.6	9	0	23	A
2.6	12	0	24	A
2.6	15	0	25	A
1.0	6	0	26	A
1.0	9	0	27	A
1.2	6	0	28	A
1.2	9	0	29	A
1.2	12	0	30	A
1.3	6	0	31	A
1.3	9	0	32	A
1.3	12	0	33	A
1.3	15	0	34	A
1.4	6	0	35	A
1.4	9	0	36	A
1.4	12	0	37	A
1.4	15	0	38	A
1.6	6	0	39	A
1.6	9	0	40	A
1.6	12	0	41	A
1.6	15	0	42	A
2.0	6	0	43	A
2.0	9	0	44	A

3-WEC Regular Waves

T (s)	H	Theta	Trial	Test
2.0	12	0	45	A
2.0	15	0	46	A
2.6	6	0	47	A
2.6	9	0	48	A
2.6	12	0	49	A
2.6	15	0	50	A
1.2	12	0	51	A
0.9	6	0	1	F
1.1	6	0	2	F
1.5	6	0	3	F
1.7	6	0	4	F
1.9	6	0	5	F
2.1	6	0	6	F
2.3	6	0	7	F
2.5	6	0	8	F
2.7	6	0	9	F
0.9	6	0	34	F
1.1	6	0	35	F
1.5	6	0	36	F
1.7	6	0	37	F
1.9	6	0	39	F
2.1	6	0	38	F
2.3	6	0	40	F
2.5	6	0	41	F
2.7	6	0	42	F
0.9	6	22.5	10	F
1.1	6	22.5	11	F
1.3	6	22.5	12	F
1.5	6	22.5	13	F
1.7	6	22.5	14	F
1.9	6	22.5	15	F
2.1	6	22.5	16	F
2.3	6	22.5	17	F
2.5	6	22.5	18	F
2.7	6	22.5	19	F
1.0	6	22.5	20	F
1.2	6	22.5	21	F
1.2	6	22.5	22	F
1.4	6	22.5	23	F
1.4	6	22.5	25	F
1.6	6	22.5	24	F
1.8	6	22.5	27	F
2.0	6	22.5	28	F
2.2	6	22.5	29	F

3-WEC Regular Waves

T (s)	H	Theta	Trial	Test
2.4	6	22.5	30	F
2.6	6	22.5	31	F
2.6	6	22.5	32	F
2.8	6	22.5	33	F
0.9	6	22.5	43	F
1.1	6	22.5	44	F
1.3	6	22.5	45	F
1.5	6	22.5	46	F
1.7	6	22.5	47	F
1.9	6	22.5	48	F
2.1	6	22.5	49	F
2.3	6	22.5	50	F
2.5	6	22.5	51	F
2.7	6	22.5	52	F
1.0	6	22.5	53	F
1.2	6	22.5	54	F
1.4	6	22.5	55	F
1.6	6	22.5	26	F
1.8	6	22.5	56	F
2.0	6	22.5	57	F
2.2	6	22.5	58	F
2.4	6	22.5	59	F
2.6	6	22.5	60	F
2.8	6	22.5	61	F
1.5	6	22.5	62	F

3-WEC Real Seas

Tp (s)	Hs (cm)	SeaState	s	Theta	Trial	Test
1.62	4.54	OR1	2	0.00	1	Real
1.62	4.54	OR1	4	0.00	2	Real
1.62	4.54	OR1	10	0.00	3	Real
1.62	4.54	OR1	0	0.00	4	Real
1.62	4.54	OR1	0	22.5	5	Real
1.42	7.58	OR2	2	0.00	6	Real
1.42	7.58	OR2	4	0.00	7	Real
1.42	7.58	OR2	10	0.00	8	Real
1.42	7.58	OR2	0	0.00	9	Real
1.42	7.58	OR2	0	22.5	10	Real
1.82	7.58	OR3	2	0.00	11	Real
1.82	7.58	OR3	4	0.00	12	Real
1.82	7.58	OR3	10	0.00	13	Real
1.82	7.58	OR3	0	0.00	14	Real
1.82	7.58	OR3	0	22.5	15	Real
2.22	7.58	OR4	2	0.00	16	Real
2.22	7.58	OR4	4	0.00	17	Real
2.22	7.58	OR4	10	0.00	18	Real
2.22	7.58	OR4	0	0.00	19	Real
2.22	7.58	OR4	0	22.5	20	Real
2.22	13.6	OR5	2	0.00	21	Real
2.22	13.6	OR5	4	0.00	22	Real
2.22	13.6	OR5	10	0.00	23	Real
2.22	13.6	OR5	0	0.00	24	Real
2.22	13.6	OR5	0	22.5	25	Real
1.22	4.54	HI	2	0.00	26	Real
1.22	4.54	HI	4	0.00	27	Real
1.22	4.54	HI	10	0.00	28	Real
1.22	4.54	HI	0	0.00	29	Real
1.22	4.54	HI	0	22.5	30	Real
1.62	10.6	IR	2	0.00	31	Real
1.62	10.6	IR	4	0.00	32	Real
1.62	10.6	IR	10	0.00	33	Real
1.62	10.6	IR	0	0.00	34	Real
1.62	10.6	IR	0	22.5	35	Real
1.62	4.54	OR1	2	0.00	36	Real
1.62	4.54	OR1	4	0.00	37	Real
1.62	4.54	OR1	10	0.00	38	Real
1.62	4.54	OR1	0	0.00	39	Real
1.62	4.54	OR1	0	22.5	40	Real
1.42	7.58	OR2	2	0.00	41	Real
1.42	7.58	OR2	4	0.00	42	Real
1.42	7.58	OR2	10	0.00	43	Real
1.42	7.58	OR2	0	0.00	44	Real

3-WEC Real Seas

Tp (s)	Hs (cm)	SeaState	s	Theta	Trial	Test
1.42	7.58	OR2	0	22.5	45	Real
1.82	7.58	OR3	2	0.00	46	Real
1.82	7.58	OR3	4	0.00	47	Real
1.82	7.58	OR3	10	0.00	48	Real
1.82	7.58	OR3	0	0.00	49	Real
1.82	7.58	OR3	0	22.5	50	Real
2.22	7.58	OR4	2	0.00	51	Real
2.22	7.58	OR4	4	0.00	52	Real
2.22	7.58	OR4	10	0.00	53	Real
2.22	7.58	OR4	0	0.00	54	Real
2.22	7.58	OR4	0	22.5	55	Real
2.22	13.6	OR5	2	0.00	56	Real
2.22	13.6	OR5	4	0.00	57	Real
2.22	13.6	OR5	10	0.00	58	Real
2.22	13.6	OR5	0	0.00	59	Real
2.22	13.6	OR5	0	22.5	60	Real
1.22	4.54	HI	2	0.00	61	Real
1.22	4.54	HI	4	0.00	62	Real
1.22	4.54	HI	10	0.00	63	Real
1.22	4.54	HI	0	0.00	64	Real
1.22	4.54	HI	0	22.5	65	Real
1.62	10.6	IR	2	0.00	66	Real
1.62	10.6	IR	4	0.00	67	Real
1.62	10.6	IR	10	0.00	68	Real
1.62	10.6	IR	0	0.00	69	Real
1.62	10.6	IR	0	22.5	70	Real

5-WEC Regular Waves

T (s)	H	Theta	Trial	Test
1	6	0	1	A
1	9	0	2	A
1.2	6	0	3	A
1.2	9	0	4	A
1.2	12	0	5	A
1.3	6	0	6	A
1.3	9	0	7	A
1.3	12	0	8	A
1.3	15	0	9	A
1.4	6	0	10	A
1.4	9	0	11	A
1.4	12	0	12	A
1.4	15	0	13	A
1.6	6	0	14	A
1.6	9	0	15	A
1.6	12	0	16	A
1.6	15	0	17	A
2	6	0	18	A
2	9	0	19	A
2	12	0	20	A
2	15	0	21	A
2.6	6	0	22	A
2.6	9	0	23	A
2.6	12	0	24	A
2.6	15	0	25	A
2.6	15	0	26	A
1	6	0	27	A
1	9	0	28	A
1.2	6	0	29	A
1.2	9	0	30	A
1.2	12	0	31	A
1.3	6	0	32	A
1.3	9	0	33	A
1.3	12	0	34	A
1.3	15	0	35	A
1.4	6	0	36	A
1.4	9	0	37	A
1.4	12	0	38	A
1.4	15	0	39	A
1.6	6	0	40	A
1.6	9	0	41	A
1.6	12	0	42	A
1.6	15	0	43	A
2	6	0	44	A

5-WEC Regular Waves

T (s)	H	Theta	Trial	Test
2	9	0	45	A
2	12	0	46	A
2	12	0	47	A
2	12	0	48	A
2	15	0	49	A
2.6	6	0	50	A
2.6	9	0	51	A
2.6	12	0	52	A
2.6	15	0	53	A
0.9	6	0	1	F
1.1	6	0	2	F
1.5	6	0	3	F
1.7	6	0	4	F
1.9	6	0	5	F
2.1	6	0	6	F
2.3	6	0	7	F
2.5	6	0	8	F
2.7	6	0	9	F
0.9	6	0	25	F
1.1	6	0	26	F
1.5	6	0	27	F
1.7	6	0	28	F
1.9	6	0	29	F
2.1	6	0	30	F
2.3	6	0	31	F
2.5	6	0	32	F
2.7	6	0	33	F
0.9	6	22.5	10	F
1.1	6	22.5	11	F
1.3	6	22.5	12	F
1.5	6	22.5	13	F
1.7	6	22.5	14	F
1.9	6	22.5	15	F
2.1	6	22.5	16	F
2.3	6	22.5	17	F
2.5	6	22.5	18	F
2.7	6	22.5	19	F
1.0	6	22.5	51	F
1.2	6	22.5	52	F
1.4	6	22.5	20	F
1.6	6	22.5	21	F
1.8	6	22.5	22	F
2.0	6	22.5	23	F
2.2	6	22.5	24	F

5-WEC Regular Waves

T (s)	H	Theta	Trial	Test
2.4	6	22.5	53	F
2.6	6	22.5	54	F
2.8	6	22.5	55	F
0.9	6	22.5	34	F
1.1	6	22.5	35	F
1.3	6	22.5	36	F
1.5	6	22.5	37	F
1.7	6	22.5	38	F
1.9	6	22.5	39	F
2.1	6	22.5	40	F
2.3	6	22.5	41	F
2.5	6	22.5	42	F
2.7	6	22.5	43	F
1.4	6	22.5	44	F
1.6	6	22.5	45	F
1.8	6	22.5	46	F
2	6	22.5	47	F
2.2	6	22.5	48	F
2.2	6	22.5	50	F

5-WEC Real Seas

Tp (s)	Hs (cm)	SeaState	s	Theta	Trial	Test
1.62	4.54	OR1	4	0.00	50	Real
1.62	4.54	OR1	10	0.00	2	Real
1.62	4.54	OR1	0	0.00	3	Real
1.62	4.54	OR1	0	22.5	4	Real
1.62	4.54	OR1	4	0.00	54	Real
1.62	4.54	OR1	10	0.00	23	Real
1.62	4.54	OR1	10	0.00	24	Real
1.62	4.54	OR1	0	0.00	25	Real
1.62	4.54	OR1	0	22.5	26	Real
1.42	7.58	OR2	4	0.00	47	Real
1.42	7.58	OR2	10	0.00	5	Real
1.42	7.58	OR2	0	0.00	6	Real
1.42	7.58	OR2	0	22.5	7	Real
1.42	7.58	OR2	10	0.00	27	Real
1.42	7.58	OR2	0	0.00	28	Real
1.42	7.58	OR2	0	22.5	29	Real
1.82	7.58	OR3	2	0.00	8	Real
1.82	7.58	OR3	4	0.00	9	Real
1.82	7.58	OR3	10	0.00	1	Real
1.82	7.58	OR3	0	0.00	10	Real
1.82	7.58	OR3	0	22.5	11	Real
1.82	7.58	OR3	2	0.00	30	Real
1.82	7.58	OR3	4	0.00	31	Real
1.82	7.58	OR3	10	0.00	32	Real
1.82	7.58	OR3	0	0.00	33	Real
1.82	7.58	OR3	0	22.5	34	Real
2.22	7.58	OR4	2	0.00	59	Real
2.22	7.58	OR4	4	0.00	48	Real
2.22	7.58	OR4	10	0.00	12	Real
2.22	7.58	OR4	0	0.00	13	Real
2.22	7.58	OR4	0	22.5	14	Real
2.22	7.58	OR4	4	0.00	56	Real
2.22	7.58	OR4	10	0.00	35	Real
2.22	7.58	OR4	0	0.00	36	Real
2.22	7.58	OR4	0	22.5	37	Real
2.22	13.6	OR5	0	0.00	38	Real
2.22	13.6	OR5	0	22.5	39	Real
2.22	13.6	OR5	0	0.00	15	Real
2.22	13.6	OR5	0	22.5	16	Real
1.22	4.54	HI	2	0.00	51	Real
1.22	4.54	HI	4	0.00	49	Real
1.22	4.54	HI	10	0.00	17	Real
1.22	4.54	HI	0	0.00	18	Real
1.22	4.54	HI	0	22.5	19	Real

5-WEC Real Seas

Tp (s)	Hs (cm)	SeaState	s	Theta	Trial	Test
1.22	4.54	HI	2	0.00	57	Real
1.22	4.54	HI	4	0.00	58	Real
1.22	4.54	HI	10	0.00	40	Real
1.22	4.54	HI	10	0.00	41	Real
1.22	4.54	HI	0	0.00	42	Real
1.22	4.54	HI	0	22.5	43	Real
1.62	10.6	IR	2	0.00	52	Real
1.62	10.6	IR	4	0.00	60	Real
1.62	10.6	IR	10	0.00	20	Real
1.62	10.6	IR	0	0.00	21	Real
1.62	10.6	IR	0	22.5	22	Real
1.62	10.6	IR	2	0.00	53	Real
1.62	10.6	IR	10	0.00	44	Real
1.62	10.6	IR	0	0.00	45	Real
1.62	10.6	IR	0	22.5	46	Real

Single-Buoy Characterization Regular Waves

T (s)	H	Theta	Trial	Test	WEC #
1.4	6	0	2	Normal	2
1.6	6	0	3	Normal	2
1.2	9	0	4	Normal	2
1.4	9	0	5	Normal	2
1.6	9	0	6	Normal	2
1.4	6	0	8	Normal	2
1.6	6	0	9	Normal	2
1.2	9	0	10	Normal	2
1.4	9	0	11	Normal	2
1.6	9	0	12	Normal	2
1.2	6	0	13	Normal	3
1.4	6	0	14	Normal	3
1.6	6	0	15	Normal	3
1.2	9	0	16	Normal	3
1.4	9	0	17	Normal	3
1.6	9	0	18	Normal	3
1.2	6	0	19	Normal	3
1.4	6	0	20	Normal	3
1.6	6	0	21	Normal	3
1.2	9	0	22	Normal	3
1.4	9	0	23	Normal	3
1.6	9	0	24	Normal	3
1.2	6	0	25	Normal	4
1.4	6	0	26	Normal	4
1.6	6	0	27	Normal	4
1.2	6	0	28	Normal	4
1.4	6	0	29	Normal	4
1.6	6	0	30	Normal	4
1.3	6	0	31	Normal	4
1.5	6	0	32	Normal	4
1.7	6	0	33	Normal	4
1.8	6	0	34	Normal	4
1.9	6	0	35	Normal	4
2	6	0	36	Normal	4
2.1	6	0	37	Normal	4
2.1	6	0	38	Normal	4
2.2	6	0	39	Normal	4
2.3	6	0	40	Normal	4
1.2	9	0	41	Normal	3
1.3	6	0	42	Normal	4
1.5	6	0	43	Normal	4
1.7	6	0	44	Normal	4

Single-Buoy Characterization Regular Waves

T (s)	H	Theta	Trial	Test	WEC #
1.8	6	0	45	Normal	4
1.9	6	0	46	Normal	4
2	6	0	47	Normal	4
2.1	6	0	48	Normal	4
2.1	6	0	48	Normal	4
2.2	6	0	49	Normal	4
2.3	6	0	50	Normal	4
1.3	6	0	51	Normal	3
1.5	6	0	52	Normal	3
1.7	6	0	53	Normal	3
1.8	6	0	54	Normal	3
1.9	6	0	55	Normal	3
2	6	0	56	Normal	3
2.1	6	0	57	Normal	3
2.2	6	0	58	Normal	3
2.3	6	0	59	Normal	3
1.3	6	0	60	Normal	3
1.5	6	0	61	Normal	3
1.7	6	0	62	Normal	3
1.8	6	0	63	Normal	3
1.9	6	0	64	Normal	3
2	6	0	65	Normal	3
2.1	6	0	66	Normal	3
2.2	6	0	67	Normal	3
2.3	6	0	68	Normal	3
1.2	6	0	69	Normal	5
1.3	6	0	70	Normal	5
1.4	6	0	71	Normal	5
1.5	6	0	72	Normal	5
1.6	6	0	73	Normal	5
1.7	6	0	74	Normal	5
1.8	6	0	75	Normal	5
1.9	6	0	76	Normal	5
2	6	0	77	Normal	5
2.1	6	0	78	Normal	5
2.2	6	0	79	Normal	5
2.3	6	0	80	Normal	5
1.3	6	0	81	Normal	5
1.5	6	0	82	Normal	5
1.7	6	0	83	Normal	5
1.9	6	0	84	Normal	5
2.1	6	0	85	Normal	5

Single-Buoy Characterization Regular Waves

T (s)	H	Theta	Trial	Test	WEC #
2.3	6	0	86	Normal	5
1.3	6	0	87	Normal	5
1.4	6	0	88	Normal	5
1.5	6	0	89	Normal	5
1.3	6	0	91	Normal	2
1.5	6	0	92	Normal	2
1.7	6	0	93	Normal	2
1.8	6	0	94	Normal	2
1.9	6	0	95	Normal	2
2	6	0	96	Normal	2
2.1	6	0	97	Normal	2
2.2	6	0	98	Normal	2
2.3	6	0	99	Normal	2
1.3	6	0	100	Normal	2
1.5	6	0	101	Normal	2
1.7	6	0	102	Normal	2
1.8	6	0	103	Normal	2
1.9	6	0	104	Normal	2
2	6	0	105	Normal	2
2	6	0	106	Normal	2
2.1	6	0	107	Normal	2
2.2	6	0	108	Normal	2
2.3	6	0	109	Normal	2
1.2	6	0	110	Normal	5
1.3	6	0	111	Normal	5
1.4	6	0	112	Normal	5
1.5	6	0	113	Normal	5
1.6	6	0	114	Normal	5
1.7	6	0	115	Normal	5
1.8	6	0	116	Normal	5
1.9	6	0	117	Normal	5
2	6	0	118	Normal	5
2.1	6	0	119	Normal	5
2.2	6	0	120	Normal	5
2.3	6	0	121	Normal	5
1.2	6	0	122	Normal	5
1.3	6	0	123	Normal	5
1.4	6	0	124	Normal	5
1.5	6	0	125	Normal	5
1.6	6	0	126	Normal	5
1.7	6	0	127	Normal	5
1.8	6	0	128	Normal	5

Single-Buoy Characterization Regular Waves

T (s)	H	Theta	Trial	Test	WEC #
1.9	6	0	129	Normal	5
2	6	0	130	Normal	5
2.1	6	0	131	Normal	5
2.2	6	0	132	Normal	5
2.3	6	0	133	Normal	5
0.9	6	0	134	Normal	2
1	6	0	135	Normal	2
1.1	6	0	136	Normal	2
2.4	6	0	137	Normal	2
2.6	6	0	138	Normal	2
0.9	6	0	139	Normal	2
0.9	6	0	140	Normal	2
1	6	0	141	Normal	2
1.1	6	0	142	Normal	2
2.4	6	0	143	Normal	2
2.6	6	0	144	Normal	2
2.6	6	0	145	Normal	2
0.9	6	0	146	Normal	3
1	6	0	147	Normal	3
1.1	6	0	148	Normal	3
2.4	6	0	149	Normal	3
2.6	6	0	150	Normal	3
0.9	6	0	151	Normal	3
1	6	0	152	Normal	3
1.1	6	0	153	Normal	3
2.4	6	0	154	Normal	3
2.6	6	0	155	Normal	3
1.2	6	0	156	Normal	4
1.3	6	0	157	Normal	4
1.4	6	0	158	Normal	4
1.5	6	0	159	Normal	4
1.6	6	0	160	Normal	4
1.7	6	0	161	Normal	4
1.8	6	0	162	Normal	4
2	6	0	163	Normal	4
2.2	6	0	164	Normal	4
0.9	6	0	165	Normal	4
1	6	0	166	Normal	4
1.1	6	0	167	Normal	4
2.1	6	0	168	Normal	4
2.6	6	0	169	Normal	4
1.2	6	0	170	Normal	4

Single-Buoy Characterization Regular Waves

T (s)	H	Theta	Trial	Test	WEC #
1.3	6	0	171	Normal	4
1.4	6	0	172	Normal	4
1.5	6	0	173	Normal	4
1.6	6	0	174	Normal	4
1.7	6	0	175	Normal	4
1.8	6	0	176	Normal	4
2	6	0	177	Normal	4
2.2	6	0	178	Normal	4
0.9	6	0	179	Normal	4
1	6	0	180	Normal	4
1.1	6	0	181	Normal	4
2.1	6	0	182	Normal	4
2.6	6	0	183	Normal	4
0.9	6	0	184	Normal	5
1	6	0	185	Normal	5
1.1	6	0	187	Normal	5
2.4	6	0	188	Normal	5
2.6	6	0	189	Normal	5
0.9	6	0	190	Normal	5
1	6	0	191	Normal	5
1.1	6	0	192	Normal	5
2.4	6	0	193	Normal	5
2.6	6	0	194	Normal	5
1	6	22.5	1	Off-Angle	2
1.1	6	22.5	2	Off-Angle	2
1.2	6	22.5	3	Off-Angle	2
1.3	6	22.5	4	Off-Angle	2
1.4	6	22.5	5	Off-Angle	2
1.5	6	22.5	6	Off-Angle	2
1.6	6	22.5	7	Off-Angle	2
1.7	6	22.5	8	Off-Angle	2
1.8	6	22.5	9	Off-Angle	2
1.9	6	22.5	10	Off-Angle	2
2	6	22.5	11	Off-Angle	2
2.1	6	22.5	12	Off-Angle	2
2.3	6	22.5	13	Off-Angle	2
2.5	6	22.5	14	Off-Angle	2
1	6	22.5	15	Off-Angle	2
1.1	6	22.5	16	Off-Angle	2
1.2	6	22.5	17	Off-Angle	2
1.3	6	22.5	18	Off-Angle	2
1.4	6	22.5	19	Off-Angle	2

Single-Buoy Characterization Regular Waves

T (s)	H	Theta	Trial	Test	WEC #
1.5	6	22.5	20	Off-Angle	2
1.6	6	22.5	21	Off-Angle	2
1.7	6	22.5	22	Off-Angle	2
1.8	6	22.5	23	Off-Angle	2
1.9	6	22.5	26	Off-Angle	2
2	6	22.5	27	Off-Angle	2
2.1	6	22.5	28	Off-Angle	2
2.3	6	22.5	29	Off-Angle	2
2.5	6	22.5	30	Off-Angle	2
1.0	6	22.5	31	Off-Angle	3
1.1	6	22.5	32	Off-Angle	3
1.2	6	22.5	33	Off-Angle	3
1.3	6	22.5	34	Off-Angle	3
1.4	6	22.5	35	Off-Angle	3
1.5	6	22.5	36	Off-Angle	3
1.6	6	22.5	37	Off-Angle	3
1.7	6	22.5	38	Off-Angle	3
1.8	6	22.5	39	Off-Angle	3
1.9	6	22.5	40	Off-Angle	3
2.0	6	22.5	41	Off-Angle	3
2.1	6	22.5	42	Off-Angle	3
2.2	6	22.5	43	Off-Angle	3
2.3	6	22.5	44	Off-Angle	3
1.0	6	22.5	45	Off-Angle	3
1.1	6	22.5	46	Off-Angle	3
1.2	6	22.5	47	Off-Angle	3
1.3	6	22.5	48	Off-Angle	3
1.4	6	22.5	50	Off-Angle	3
1.5	6	22.5	51	Off-Angle	3
1.6	6	22.5	52	Off-Angle	3
1.7	6	22.5	53	Off-Angle	3
1.8	6	22.5	54	Off-Angle	3
1.9	6	22.5	55	Off-Angle	3
2.0	6	22.5	56	Off-Angle	3
2.1	6	22.5	57	Off-Angle	3
2.2	6	22.5	58	Off-Angle	3
2.3	6	22.5	59	Off-Angle	3
1	6	22.5	60	Off-Angle	4
1.1	6	22.5	61	Off-Angle	4
1.2	6	22.5	62	Off-Angle	4
1.3	6	22.5	63	Off-Angle	4
1.4	6	22.5	64	Off-Angle	4

Single-Buoy Characterization Regular Waves

T (s)	H	Theta	Trial	Test	WEC #
1.5	6	22.5	65	Off-Angle	4
1.6	6	22.5	66	Off-Angle	4
1.7	6	22.5	67	Off-Angle	4
1.8	6	22.5	68	Off-Angle	4
1.9	6	22.5	69	Off-Angle	4
2	6	22.5	70	Off-Angle	4
2.1	6	22.5	71	Off-Angle	4
2.3	6	22.5	72	Off-Angle	4
2.5	6	22.5	73	Off-Angle	4
1	6	22.5	74	Off-Angle	4
1.1	6	22.5	75	Off-Angle	4
1.2	6	22.5	76	Off-Angle	4
1.3	6	22.5	77	Off-Angle	4
1.4	6	22.5	78	Off-Angle	4
1.5	6	22.5	79	Off-Angle	4
1.6	6	22.5	80	Off-Angle	4
1.7	6	22.5	81	Off-Angle	4
1.8	6	22.5	82	Off-Angle	4
1.9	6	22.5	83	Off-Angle	4
2	6	22.5	84	Off-Angle	4
2.1	6	22.5	85	Off-Angle	4
2.3	6	22.5	86	Off-Angle	4
2.5	6	22.5	87	Off-Angle	4
1.0	6	22.5	88	Off-Angle	5
1.1	6	22.5	89	Off-Angle	5
1.2	6	22.5	90	Off-Angle	5
1.3	6	22.5	91	Off-Angle	5
1.4	6	22.5	92	Off-Angle	5
1.5	6	22.5	93	Off-Angle	5
1.6	6	22.5	94	Off-Angle	5
1.7	6	22.5	95	Off-Angle	5
1.8	6	22.5	96	Off-Angle	5
1.9	6	22.5	97	Off-Angle	5
2.0	6	22.5	98	Off-Angle	5
2.1	6	22.5	99	Off-Angle	5
2.2	6	22.5	100	Off-Angle	5
2.3	6	22.5	101	Off-Angle	5
1.0	6	22.5	102	Off-Angle	5
1.1	6	22.5	103	Off-Angle	5
1.2	6	22.5	104	Off-Angle	5
1.3	6	22.5	105	Off-Angle	5
1.4	6	22.5	106	Off-Angle	5

Single-Buoy Characterization Regular Waves

T (s)	H	Theta	Trial	Test	WEC #
1.5	6	22.5	107	Off-Angle	5
1.6	6	22.5	108	Off-Angle	5
1.7	6	22.5	109	Off-Angle	5
1.8	6	22.5	110	Off-Angle	5
1.9	6	22.5	111	Off-Angle	5
2.0	6	22.5	112	Off-Angle	5
2.1	6	22.5	113	Off-Angle	5
2.2	6	22.5	114	Off-Angle	5
2.3	6	22.5	115	Off-Angle	5

Single-Buoy Characterization Real Seas

Tp (s)	Hs (cm)	SeaState	s	Theta	Trial	Test	WEC #
1.82	7.58	OR3	UD	0.00	1	Real	5
1.62	10.6	IR	UD	0.00	2	Real	5
1.62	4.54	OR1	UD	0.00	3	Real	5
1.82	7.58	OR3	UD	0.00	4	Real	5
1.62	10.6	IR	UD	0.00	5	Real	5
1.62	4.54	OR1	UD	0.0	6	Real	5
1.62	4.54	OR1	10	0.00	7	Real	3
1.62	4.54	OR1	10	0.00	8	Real	3
1.62	4.54	OR1	UD	0.00	9	Real	3
1.62	4.54	OR1	UD	22.5	10	Real	3
1.82	7.58	OR3	10	0.00	11	Real	3
1.82	7.58	OR3	UD	0.00	12	Real	3
1.82	7.58	OR3	UD	22.5	13	Real	3
1.62	10.6	IR	10	0.00	14	Real	3
1.62	10.6	IR	UD	0.00	15	Real	3
1.62	10.6	IR	UD	22.5	16	Real	3
1.62	4.54	OR1	10	0.00	17	Real	3
1.62	4.54	OR1	UD	0.00	18	Real	3
1.62	4.54	OR1	UD	22.5	19	Real	3
1.82	7.58	OR3	10	0.00	20	Real	3
1.82	7.58	OR3	UD	0.00	22	Real	3
1.82	7.58	OR3	UD	22.5	23	Real	3
1.62	10.6	IR	10	0.00	24	Real	3
1.62	10.6	IR	UD	0.00	25	Real	3
1.62	10.6	IR	UD	22.5	26	Real	3
1.62	4.54	OR1	10	0.0	27	Real	5
1.62	4.54	OR1	UD	22.5	28	Real	5
1.82	7.58	OR3	10	0.00	29	Real	5
1.82	7.58	OR3	UD	22.5	30	Real	5
1.62	10.6	IR	10	0.00	31	Real	5
1.62	10.6	IR	10	0.00	32	Real	5
1.62	10.6	IR	UD	22.5	33	Real	5
1.62	4.54	OR1	10	0.00	34	Real	5
1.62	4.54	OR1	UD	22.5	35	Real	5
1.82	7.58	OR3	10	0.00	36	Real	5
1.82	7.58	OR3	UD	22.5	37	Real	5
1.62	10.6	IR	10	0.00	38	Real	5
1.62	10.6	IR	UD	22.5	39	Real	5